CNWRA *A center of excellence in earth sciences and engineering*

A Division of Southwest Research Institute™
6220 Culebra Road • San Antonio, Texas, U.S.A. 78228-5166
(210) 522-5160 • Fax (210) 522-5155

September 26, 2002
Contract No. NRC–02–97–009
Account No. 20.01402.671

U.S. Nuclear Regulatory Commission
ATTN: Dr. Mysore S. Nataraja
Division of Waste Management
Two White Flint North (Mail Stop 7–C6)
Washington, DC 20555

SUBJECT: Repository Design and Thermal-Mechanical Effects Key Technical Issue Intermediate Milestone No. 20.01402.671.220, DECOVALEX Thermal-Mechanical-Hydrological Coupled Analysis—Progress Report

Dear Dr. Nataraja:

Attached is the Center for Nuclear Regulatory Analyses (CNWRA) document entitled "DECOVALEX III Task 2C: Thermal-Mechanical Modeling of the Drift-Scale Heater Test at Yucca Mountain." To better reflect the content of the document, the title has been changed from that originally identified in the Operations Plan. This technical document fulfills the requirements for the subject milestone, which is due September 27, 2002.

DECOVALEX (acronym for the **DE**velopment of **CO**upled models and their **VAL**idation against **EX**periments in nuclear waste isolation) is an international cooperative project to support the development of mathematical models for coupled processes in the geosphere, and their applications and validation against experiments in the field of nuclear waste isolation. The drift-scale heater test at the Exploratory Studies Facility at Yucca Mountain has been designated for study under Task 2 of the DECOVALEX III project. The NRC/CNWRA research team is involved in the Subtasks 2A and 2C modeling activities. The two-dimensional thermal-hydrological analysis of the drift-scale heater test for Subtask 2A was completed, and the report was submitted to the NRC and the DECOVALEX Secretariat.

This report presents the thermal-mechanical analyses results for Subtask 2C modeling using the finite difference computer code Fast Lagrangian Analysis of Continua (FLAC). Specific topics addressed in this report are (i) technical approach, (ii) thermal-mechanical models used in the analysis, and (iii) modeling results. The modeling studies presented in this report provide valuable insight for evaluating DOE models used to demonstrate a safety case for the design and analysis of the geologic repository at Yucca Mountain.

Washington Office • Twinbrook Metro Plaza #210
12300 Twinbrook Parkway • Rockville, Maryland 20852-1606

If you have any questions regarding this report, please contact me at (210) 522-5151 or Dr. Simon Hsiung at (210) 522-5209.

Sincerely yours,

Asadul H. Chowdhury, Manager
Mining, Geotechnical, and
Facility Engineering

AC/cap

Attachment

cc: J. Greeves
J. Schlueter
W. Reamer
D. DeMarco
B. Meehan
N. Stablein
J. Linehan (w/o Attachment)
D. Riffle
C. Trottier
D. Brooks
B. Jagannath
L. Campbell
T. Ahn
J. Andersen
R. Johnson
T. McCartin
P. Justus
J. Pohle
W. Patrick
B. Sagar
G. Wittmeyer
P. Maldonado
S. Hsiung
A. Ghosh
D. Gute
G. Ofoegbu
B. Dasgupta
T. Maxwell
R. Fedors
R. Green
CNWRA Element Managers and Directors (letter only)
T. Nagy (SwRI Contracts)

D:\MGFE\Simon\Letters\decovalex-lttr.wpd

DECOVALEX III TASK 2C: THERMAL-MECHANICAL MODELING OF THE DRIFT-SCALE HEATER TEST AT YUCCA MOUNTAIN

Prepared for

U.S. Nuclear Regulatory Commission
Contract NRC–02–97–009

Prepared by

Sui-Min Hsiung
Asadul H. Chowdhury

Center for Nuclear Waste Regulatory Analyses
San Antonio, Texas

September 2002

ABSTRACT

The drift-scale heater test at the Exploratory Studies Facility at Yucca Mountain is designated for study in Task 2 of the DECOVALEX III project. A U.S. Nuclear Regulatory Commission (NRC) and Center for Nuclear Waste Regulatory Analyses research team is involved in Subtasks 2A and 2C modeling activities. The two-dimensional thermal-hydrological analysis of the drift-scale heater test in Subtask 2A was completed, and the report was submitted to the NRC and the DECOVALEX Secretariat. This report documents the analysis conducted for Subtask 2C modeling activities to predict the (i) temperature-induced mechanical deformation surrounding the heated drift, and (ii) thermal-mechanical effects on rock mass permeability.

The thermal-mechanical modeling was conducted using a continuum approach. The finite difference computer program, Fast Lagrangian Analysis Continua Version 4.0 (Itasca Consulting Group, Inc, 2000), was used for this analysis. Thermal-mechanical modeling was carried out for the entire modeling domain using (i) intact-rock properties (Basecase 1) and (ii) rock-mass properties (Basecase 2). Three litho-stratigraphic units were modeled in the simulations: Upper Lithophysal, Middle Nonlithophysal, and Lower Lithophysal litho-stratigraphic units. A circular drift, 5 m in diameter, was simulated in the middle of the Middle Nonlithophysal litho-stratigraphic unit. Sensitivity analyses were also conducted to examine the potential effects of (i) variations of measured intact rock Young's modulus and strength properties, approximately one standard deviations from the corresponding values, for the models using intact-rock properties and (ii) variations of rock-mass quality for the models using rock-mass properties on the rock responses, including deformation and permeability.

Two temperature options were used in this study. For Temperature Option 1, temperature data provided by the Task 2 technical monitor research team were used directly. The temperature data for Temperature Option 2 were exactly the same as those for Temperature Option 1 except the location of each temperature value in space was adjusted vertically 2 m [6.56 ft] upward. This adjustment was intended to match better the locations of high-temperature zones with the locations of the outer wing heaters.

It was found that the thermal-mechanical modeling with rock-mass properties (Basecase 2) resulted in much larger yield zones in all three litho-stratigraphic units simulated than the simulation with intact-rock properties (Basecase 1) irrespective of temperature options used. In the latter case, no yield zones were developed in the Upper and Lower Lithophysal units while a yield zone with a dimension of greater than 5-drift diameter in width and greater than 8-drift diameter in height was observed in the Upper Lithophysal unit and a yield zone with a dimension of greater than 5-drift diameter in width and greater than 6-drift diameter in height in the Lower Lithophysal unit also were observed for the former case. Similar yielding zones could be induced for the intact-rock basecase by increasing the Young's modulus or reducing cohesion and tensile strength of the intact rock. The yielding or failure modes for these intact-rock cases, however, appeared to be different from those observed for the rock-mass cases. The yield zones associated with the intact-rock cases are mostly caused by tensile failure and shear failure for the rock-mass cases.

The predicted rock displacements for Temperature Option 2 were much larger in the roof of the heated drift compared to Temperature Option 1; the predicted displacements in the floor were, however, considerably smaller. The cases using rock-mass properties, in general, resulted in

larger displacements surrounding the heated drift than the cases with intact-rock properties for both temperature options. The predicted displacements were found insensitive to the variations of rock properties or rock-mass qualities for either of the temperature options except for the variation of rock-mass quality under Temperature Option 2.

A continuum model representing a deformation-permeability relationship was developed to predict thermal-mechanically induced permeability variations. The excavation-induced changes in permeability were found to be small and reversed at the early stage of heating. The increase in permeability because of heating was found to occur at a large spatial scale with the largest increase coinciding with the highest temperature zones. The highest increase observed was more than 4 times the initial permeability. Temperature options were found to have more influence on permeability prediction than the variations in rock-mass quality and intact rock properties. The largest increase in permeability observed in the specified prediction locations was around 61 percent for Temperature Option 2. This magnitude of change in permeability is considered to be inconsequential for overall performance assessment, considering relatively large (several orders of magnitude) uncertainty associated with *in-situ* permeability measurements.

REFERENCE

Itasca Consulting Group, Inc. "FLAC—Fast Lagrangian Analysis of Continua, Version 4.0." Minneapolis, Minnesota: Itasca Consulting Group, Inc. 2000.

CONTENTS

FIGURES

FIGURES, Continued

FIGURES, Continued

TABLES

ACKNOWLEDGMENTS

This report was prepared to document work performed by the Center for Nuclear Waste Regulatory Analyses (CNWRA) for the U.S. Nuclear Regulatory Commission (NRC) under Contract No. NRC–02–97–009. The activities reported here were performed on behalf of the NRC Office of Nuclear Material Safety and Safeguards, Division of Waste Management. The report is an independent product of the CNWRA and does not necessarily reflect the views or regulatory position of the NRC.

The authors thank A. Ghosh and B. Sagar for their reviews of this report. The authors are thankful to C. Patton for assisting with the word processing and preparation of the report and to C. Cudd, A. Woods, and B. Long for editorial reviews.

QUALITY OF DATA, ANALYSES, AND CODE DEVELOPMENT

DATA: No CNWRA-generated original data are contained in this report. Sources for other data should be consulted for determining the level of quality for those data.

ANALYSES AND CODES: Numerical models presented in this report were developed using the finite difference computer code Fast Lagrangian Analysis of Continua (FLAC) Version 4.0 (Itasca Consulting Group, Inc, 2000). This computer code is controlled by the CNWRA software quality assurance procedure (Technical Operating Procedure–018, Development and Control of Scientific and Engineering Software).

REFERENCE

Itasca Consulting Group, Inc. "FLAC—Fast Lagrangian Analysis of Continua, Version 4.0." Minneapolis, Minnesota: Itasca Consulting Group, Inc. 2000.

1 INTRODUCTION

1.1 Background

DECOVALEX (acronym for the **DE**velopment of **CO**upled models and their **VAL**idation against **EX**periments in nuclear waste isolation) is an international cooperative project to support the development of mathematical models for coupled processes in the geosphere and their applications and validation against experiments in the field of nuclear waste isolation. The DECOVALEX project has been designed to increase understanding of coupled thermal-hydrological-mechanical processes as they affect rock-mass responses and radionuclide release and transport from a repository to the biosphere and also to assess how these processes can be described by mathematical models. The DECOVALEX project also attempts to identify contributions of these coupled processes to the overall performance assessment in both the near and far fields. DECOVALEX includes three phases. DECOVALEX I began in 1991 and was completed in 1995. In this phase, the activities focused on modeling laboratory experiments and benchmark problems. The U.S. Nuclear Regulatory Commission (NRC) was an active participant of DECOVALEX I. The Center for Nuclear Waste Regulatory Analyses (CNWRA) assisted NRC in performing the analyses. DECOVALEX II started in 1995 and concluded in 1999. This phase focused on using the modeling experience gained during the first phase to simulate experiments conducted in the field. Attention was also given to relating the effects of the thermal-hydrological-mechanical processes to the performance of nuclear waste isolation. NRC and CNWRA did not participate in this phase of the project. DECOVALEX III, the current phase, began in 1999 and includes four tasks:

- Task 1 involves modeling the *in situ*, full-scale engineered barriers experiment.
- Task 2 involves modeling the thermal-hydrological-mechanical-chemical behavior of the drift-scale heater test at Yucca Mountain.
- Task 3 includes three benchmark problems. The first problem presents the implication of thermal-hydrological-mechanical coupling on the near-field performance of a nuclear waste repository. The second problem investigates the effects of upscaling thermal-hydrological-mechanical processes on performance assessment results. The third problem studies the effects of glaciation on rock-mass behavior surrounding a nuclear waste repository.
- Task 4 attempts to address the issue of incorporating the effects of thermal-hydrological-mechanical-chemical processes to performance assessment.

NRC, with the assistance of CNWRA, is actively participating in the DECOVALEX III project. Task 2 is the focus of NRC involvement because this task is most relevant to the high-level waste program in the United States.

1.2 Objective and Scope

As discussed previously, Task 2 of the DECOVALEX III project models the thermal-hydrological-mechanical-chemical behavior of the drift-scale heater test performed by

the U.S. Department of Energy (DOE) in the Exploratory Studies Facility at Yucca Mountain, Nevada. This task includes four subtasks. Subtask 2A focuses on performing thermal-hydrological modeling analyses of the drift-scale heater test to predict the temperature and saturation distribution in the rock during the heating phase of the test. The outcome of this predictive analysis forms the basis for comparison with the measured temperatures and saturations to validate the models used to represent thermal-hydrological processes. Subtask 2B is related to modeling thermally induced rock-mass deformation and the thermal-mechanical effect on rock-mass permeability at various times of the heating phases of the test. The predicted and measured displacements and permeability changes/variations are compared to validate the thermal-hydrological-mechanical models. The specific locations required by Task 2 for displacement and permeability predictions are discussed in detailed in Section 3. In this subtask, the predicted temperatures from Subtask 2A will be used as temperature input for analyses. Subtask 2C involves the same thermal-mechanical modeling activities as those in Subtask 2B. Subtask 2C, however, uses measured temperatures for analyses instead of the predicted ones from Subtask 2A. Subtask 2D includes modeling of thermal-hydrological-chemical processes associated with the drift-scale heater test.

The NRC and CNWRA modeling effort for Task 2 focuses on Subtasks 2A and 2C. The two-dimensional thermal-hydrological analyses of the drift-scale heater test for Subtask 2A used the computer code MULTIFLO (Lichtner et al., 2000). Analyses have been completed. A report documenting the two-dimensional final analyses results for Subtask 2A was submitted to NRC and the Secretariat of the DECOVALEX project in May 2001 (Green et al., 2001), thereby fulfilling the original objective of the thermal-hydrological analyses for Subtask 2A. Since then, through discussions between the NRC and CNWRA research team and DECOVALEX Secretariat, the scope of the thermal-hydrological analyses at CNWRA for Subtask 2A has been extended to three-dimensional analysis using MULTIFLO. These thermal-hydrological analyses are in progress at CNWRA.

This report presents the thermal-mechanical analyses results for Subtask 2C modeling using the finite difference computer code Fast Lagrangian Analysis of Continua (FLAC). Specific topics addressed in this report are (i) technical approach, (ii) thermal-mechanical models used in the analysis, and (iii) modeling results. No comparison with the measured displacements and permeability changes were made in this report because the measured data have not been provided by the Task 2 technical monitor research team. This comparison will be made documented in a later report. The modeling studies reported herein will provide valuable insight for evaluating and developing confidence in DOE models used to demonstrate a safety case for the design and analysis of the geologic repository at Yucca Mountain.

2 TECHNICAL APPROACH AND THEORETICAL BACKGROUND

Two fundamentally different approaches are available for numerically modeling behavior of rock mass. The first modeling approach assumes that a rock mass behaves as a continuous material, often called the continuum approach. In this modeling approach, the presence of discontinuities may be accounted for by making various assumptions. It is a common understanding that discontinuities in rock media make the rock softer and weaker. A softer rock tends to deform more than a stiffer one with the same loading condition. A weaker rock can be modeled by reducing the rock strength parameters. The finite element and finite difference techniques are well suited for modeling this type of material. The second approach for modeling rock mass is to include discontinuities explicitly into the model. This approach is referred to as the discontinuum approach. Discrete element and discontinuous deformation analysis methods are among the techniques currently available and used for direct modeling of discontinuities in the numerical analysis.

In the modeling effort for Subtask 2C to analyze the thermal-mechanical behavior of the rock mass surrounding the drift-scale heater test, the continuum approach was used. The finite difference code FLAC (Version 4.0) was used to conduct the continuum analysis. FLAC is a two-dimensional explicit finite difference program (Itasca Consulting Group, Inc, 2000) used to solve a wide range of complex problems in mechanics. This program simulates the behavior of structures of soil, rock, or other materials that may undergo plastic flow when their yield limits are reached.

FLAC is controlled by the CNWRA software quality assurance procedure (Technical Operating Procedure–018, Development and Control of Scientific and Engineering Software). The theoretical background of the FLAC computer code and the conceptual model used to describe fracture-aperture changes as a result of deformations using a continuum approach are discussed in the following sections. The former was taken from the FLAC user's manual.

2.1 Field Equations

FLAC uses a time-marching method to solve a set of algebraic equations of motion and constitutive relations. In a continuous solid body, the equation of motion can be generalized from Newton's law of motion for a mass and spring system in a tensor form as follows

$$\rho \frac{\partial \dot{u}_i}{\partial t} = \frac{\partial \sigma_{ij}}{\partial x_j} + \rho g_i \qquad (2\text{-}1)$$

where ρ is the mass density, t is time, $\dot{u}_i$ are components of velocity vector, x_j are components of coordinate vector, σ_{ij} are components of stress tensor, g_i are components of body force, and indices i and j are components in a Cartesian coordinate system.

Subjected to the equation of motion in Eq. (2-1), the associated strain rate may be derived from velocity gradient using the following equation

$$\dot{e}_{ij} = \frac{1}{2}\left[\frac{\partial \dot{u}_i}{\partial x_j} + \frac{\partial \dot{u}_j}{\partial x_i}\right] \tag{2-2}$$

where $\dot{e}_{ij}$ are strain-rate components. With the strain-rate known, the constitutive relation that describes the stress-strain relationship of a deformable body for an isotropic elastic material can be represented by

$$\Delta\sigma_{ij} = \{\delta_{ij}(K - \frac{2}{3}G)\dot{e}_{kk} + 2G\dot{e}_{ij}\}\Delta t \tag{2-3}$$

where δ_{ij} is the Kronecker delta, Δt is the timestep, and K and G are bulk and shear modulus, respectively.

In FLAC, the large-strain condition can be accounted for, if the option is selected, by adding the rotation-induced stress component expressed in the following term to the stress components in Eq. (2-3)

$$\omega_{ik}\sigma_{kj} - \sigma_{ik}\omega_{kj} \tag{2-4}$$

where

$$\omega_{ij} = \frac{1}{2}\left[\frac{\partial \dot{u}_i}{\partial x_j} - \frac{\partial \dot{u}_j}{\partial x_i}\right]\Delta t \tag{2-5}$$

2.2 Formulation of Thermally Induced Stresses

The FLAC computer code has a thermal option that allows simulation of transient heat conduction and calculation of thermally induced displacements and stresses in materials. This thermal option requires a prescribed heat-generating source function as input. The heat source input along with the thermal conductivity and specific heat of the material are used to compute temperature changes. The calculated temperature changes are then used for determining stresses and displacements.

Since the thermal-mechanical modeling activities involved in Subtask 2C require the use of measured temperatures directly, the thermal option in the FLAC computer code was not needed for this purpose. Consequently, subroutines were prepared to read in temperature change data input in both temporal and spatial domains and to calculate the thermally induced stress changes using the FLAC built-in programming language FISH (short for FLACish). The change in state of stresses, as a result of temperature change, generates an out-of-balance force for the

system modeled. A mechanical cycling procedure in FLAC was invoked until a steady-state solution (i.e., the unbalanced force was smaller than a predetermined limit) was reached.

The stress and temperature relationship used in the user defined subroutine (FISH function) followed

$$\Delta\sigma_{ij} = -\delta_{ij}\ 3\ K\alpha\Delta T \tag{2-6}$$

where α is thermal expansion coefficient, and ΔT is temperature change. Equation (2-6) is for a plane strain condition.

2.3 Continuum Model of Deformation-Permeability Relationship

2.3.1 Matrix Permeability of Fractured Rocks

As indicated in Section 1, one of the objectives of this study is to predict the thermal-mechanical effects on rock-mass permeability. Permeability is a measure of the ability of a material to transmit fluid under a hydraulic gradient. Permeability is the most important rock parameter pertinent to fluid flow; it is an intrinsic property of rock and relates to the presence of interconnected voids (pores) and fractures. In general, permeability of a rock mass can be divided into two parts, matrix and fracture permeabilities.

For a porous medium, the matrix permeability, k_m, may be determined using the Carman-Kozeny equation (Panda and Lake, 1994)

$$k_m = \frac{D_p^2 \varphi_m^3}{72\tau_m\left(1-\varphi_m\right)^2} \tag{2-7}$$

where D_p is the particle diameter, φ_m is the porosity of the medium, and τ_m is tortuosity of the medium. Assuming that D_p and τ_m are constant when they are subjected to stress changes, the matrix permeability at a state of stresses can be expressed as

$$k_m = k_{mo}\frac{\varphi_m^3}{\left(1-\varphi_m\right)^2}\frac{\left(1-\varphi_{mo}\right)^2}{\varphi_{mo}^3} \tag{2-8}$$

where φ_{mo} is reference matrix porosity, and k_{mo} is the intrinsic permeability for matrix porosity, φ_{mo}.

2.3.2 Fracture Permeability of Fractured Rocks

Permeability in fractures depends on size, density, connectivity, orientation, and smoothness of fractures. The permeability, k_f, for individual fractures can be represented by (Mohanty et al., 1994)

$$k_f = \frac{b^2}{12} \tag{2-9}$$

where b is fracture aperture. This expression may be modified to account for fracture roughness. The fracture-set permeability for a set of fractures characterized by fracture density, f_d, on the other hand, can be expressed by (Ofoegbu, 2000; Elsworth and Mase, 1993; Elsworth, 1989)

$$k_f = f_d \frac{b^3}{12} \tag{2-10}$$

The fracture permeability in the fracture-parallel direction for a two-orthogonal-fracture-set system is given by (Ofoegbu, 2000; Elsworth and Mase, 1993; Elsworth, 1989)

$$k_f = f_d \frac{b^3}{6} \tag{2-11}$$

Although the assumption of orthogonal fracture sets is somewhat restrictive, it greatly reduces the effort of relating fracture permeability and fracture aperture and density. Relaxing this assumption may be possible, but it most likely will make the relationship complicated, and much more effort may be required to develop such a relationship.

2.3.3 Continuum Representation for Mechanical Effect on Fractured Rock Permeability

In a continuum approach, direct representation of fracture permeability is not possible. A mathematical derivation of fractured-rock-mass permeability for this study, based on several assumptions, is presented in this section.

When a fractured-rock medium is subjected to stress changes, resulting from either excavation or temperature variation, deformation of the rock mass affected will be induced. As a result, the volume of the fractured-rock medium changes accordingly. The extent of volume change depends on the magnitude of stress changes.

This volume change may be related to changes in matrix and fracture porosities of the fractured-rock medium through volumetric strain. For a deformed rock block, its volumetric strain, e_v, can be determined using

$$e_v = \frac{\Delta V}{V} \tag{2-12}$$

where ΔV is the volume change, and V is the rock volume before deformation took place. As discussed earlier, e_v may be directly related to the changes in both matrix and fracture porosities, $\Delta\varphi_m$ and $\Delta\varphi_f$.

$$e_v = \Delta\varphi_m + \Delta\varphi_f \tag{2-13}$$

In deformable fractured rocks, changes in matrix porosity are small. Furthermore, for the fractured rocks of interest in this study, their matrix permeabilities are more than four orders of magnitude smaller than the fracture permeabilities (CRWMS M&O, 2001). Consequently, the influence of volume change induced matrix-permeability change to the overall permeability of a fractured-rock mass is likely very small. With this understanding, Eq. (2-13) can be approximated by

$$e_v = \Delta\varphi_f \tag{2-14}$$

With the assumptions that a fractured-rock mass consists of three mutually perpendicular fracture sets, each with fracture density f_d and aperture b, Ofoegbu (2000) suggested that the linear fracture density normal to a given fracture set is f_d, and the volumetric fracture density is $3f_d$. The fracture aperture of the rock mass can then be related to fracture porosity by

$$b = \frac{\varphi_f}{3f_d} \tag{2-15}$$

The fractured-rock mass permeability is related to fracture porosity by combining Eqs. (2-11) and (2-15)

$$k_f = \frac{\varphi_f^3}{27f_d^2} \tag{2-16}$$

Eq. (2-16) can be further expressed using the fracture porosity before change, φ_{fo}, and fracture porosity change, $\Delta\varphi_f$

$$k_f = \frac{\left(\varphi_{fo} + \Delta\varphi_f\right)^3}{27f_d^2} \tag{2-17}$$

The fractured-rock mass permeability after stress change can be directly related to the permeability before stress change, k_{fo}

$$k_f = k_{fo}\left(1+\frac{\Delta\varphi_f}{\varphi_{fo}}\right)^3 = k_{fo}\left(1+\frac{e_v}{\varphi_{fo}}\right)^3 \tag{2-18}$$

Note that e_v in Eq. (2-18) includes both elastic, e_{ve}, and inelastic volumetric strain, e_{vi}. The elastic volumetric strain, e_{ve}, is caused by normal compression or extension of fractures and the shear deformation of fracture before dilation while the inelastic volumetric strain, e_{vi}, could result from fracture shear dilation or inelastic extension. A plasticity-based yielding or failure criterion can be used to accumulate inelastic volumetric strain. While the inelastic volumetric strain is irreversible, elastic volumetric strain is recoverable. Equation (2-18) offers a means of analyzing permeability change caused by elastic deformation of rock mass and an opportunity of assessing the effect of cooling planned for the drift-scale heater test on rock-mass permeability even though the assumption of orthogonal joint sets is not representative to the area. This equation suggests that permeability is fully recoverable if the rock mass is in the elastic range throughout the loading path. Otherwise, after complete unloading, inelastic-deformation-induced permeability change remains.

Laboratory experiments have suggested that the compressibility of fracture decreases as applied normal stress increases. A fracture can no longer be compressed when a limiting aperture is reached (Witherspoon et al., 1980; Bandis et al., 1983; Barton et al., 1985; Schrauf and Evans, 1986; Hsiung et al., 1994). This limiting aperture is believed to be fracture roughness and fracture wall-strength dependent. To account for this behavior, a limiting value for fracture porosity can be established for Eq. (2-18). For example, the limiting value, φ_L, can be set as

$$\varphi_L = e_{veL} = R_L\varphi_{fo} \tag{2-19}$$

where R_L is a fraction value, and e_{veL} is the limiting elastic strain. The resulting fracture porosity because of deformation should not be smaller than φ_L. A complete description of continuum representation of the deformation-permeability model is obtained by combining Eqs. (2-18) and (2-19).

$$\begin{aligned} k_f &= k_{fo}\left(1+\frac{e_{ve}+e_{vi}}{\varphi_{fo}}\right)^3, \qquad e_{ve} \geq -R_L\varphi_{fo} \\ k_f &= k_{fo}\left(1+\frac{-R_L\varphi_{fo}+e_{vi}}{\varphi_{fo}}\right)^3, \quad e_{ve} < -R_L\varphi_{fo} \end{aligned} \tag{2-20}$$

3 MODEL DESCRIPTION AND DATA INPUT

3.1 Drift-Scale Heater Test

3.1.1 General Description

The drift-scale heater test facility is located in the Topopah Spring middle nonlithophysal zone (CRWMS M&O, 1997a). The Topopah Spring middle nonlithophysal zone is approximately 30–40 m [98.4–131.2 ft] thick at the location of the drift-scale test area. This zone is overlain by the Topopah Spring upper lithophysal and underlain by the Topopah Spring lower lithophysal zones. Figure 3-1 shows a generalized stratigraphic column including expanded lithologic information from ground surface to below Calico Hills formation for the proposed repository.[1] Note that, for the convenience of organizing the report, all figures presented in Sections 3 and 4 are placed at the end of the respective sections.

The drift-scale heater test block was characterized prior to the onset of heating. The characterization included geologic mapping, local geology, rock-mass classification, and some geotechnical data. Figure 3-2 shows a plane-view schematic of the drift-scale heater test region and associated access. The heater drift was approximately 5 m [16.4 ft] in diameter and 47.5 m [155.8 ft] long and was closed at the east end by a thermal bulkhead (east is the right of the figure).

Approximately 12.5 m [41.01 ft] of the heated drift, from the west end, was lined with a cast-in-place concrete liner with a drift-diameter of 5.6 m [18.4 ft]. The drift diameter gradually increased from 5 m [16.4 ft] to 5.6 m [18.4 ft] starting at a location 36 m [118.1 ft] from the thermal bulkhead over a 2-m [6.6-ft] length. A concrete invert was poured along the entire floor of the heated drift. Eight 20-mm [0.79-in] thermal expansion joints were cast into the invert at a nominal spacing of 6 m [19.7 ft].

Thermal sources for the heated drift consisted of 9 canister heaters, placed end to end on the concrete inverts of the heated drift, and 50 wing heaters (25 on either side) placed in horizontal boreholes drilled into the sidewalls of the heated drift about 0.25 m [0.8 ft] below the springline. These two types of electric heaters had an initial, combined power output of approximately 200 kW [189.6 Btu/s]. Locations of the wing heaters around the heated drift can be found in CRWMS M&O (1997b). The wing heaters were spaced 1.83 m [6 ft] apart. Each wing heater had two segments {5 m [16.4 ft] long} with a larger power output from the outer segment {85.8 kW [81.3 Btu/s] versus 57.2 kW [54.2 Btu/s]}. The inner wing heater segment was separated from the heater drift by 1.5 m [4.9 ft].

Temperatures were measured at approximately 2,662 locations for the drift-scale heater test. Instruments aiming at investigating various aspects of thermal-mechanical-hydrological-chemical coupling phenomena were installed in more than 140 boreholes around the heated drift.

[1]This information is provided by the technical monitor research team for Task 2 of the DECOVALEX III project.

3.1.2 Specific Requirements on Numerical Predictions

In the study reported herein, numerical predictions are made on (i) rock-mass displacements at locations that coincide with the anchors of four multiple-position extensometers located at the cross section approximately 21 m [68.9 ft] from the thermal bulkhead and (ii) permeability variations at locations that coincide with the locations of the pressure sensors for hydrologic boreholes, two at the cross section approximately 10 m [32.1 ft] and the other at the cross section approximately 30 m [98.4 ft] from the thermal bulkhead.

Figures 3-3 and 3-4 illustrate the relative locations of hydrologic boreholes and multiple-position extensometers of interest to the heated drift. Also shown in the figures are locations of pressure sensors and anchors in each of the boreholes. The data for anchor and pressure sensor locations were obtained from CRWMS M&O (1998). The anchors for all the multiple-position extensometers were numbered from 1 to 4, with the anchors with smaller numbers closer to the drift wall than those with larger numbers. A similar numbering system was used also for the pressure sensors in the hydrologic boreholes except the pressure sensors with larger numbers were located closer to the drift than the sensors with smaller numbers. Notice that there might be an error in the location of Anchor 4 in hydrologic borehole 59; no attempt was made to correct this potential error.

Note that hydrologic boreholes 57 and 59 shown in Figure 3-3 were located 10 m [32.1 ft] and hydrologic boreholes 74 and 76 were located 30 m [98.4 ft] from the thermal bulkhead. For the four extensometers shown in Figure 3-4, two were vertically oriented (one in the crown and one in the invert), and the remaining two were inclined at approximately 30° to the vertical extensometer on either side of the vertical extensometer.

3.2 Drift-Scale Heater Test Model Domain

A vertically oriented two-dimensional cross section was configured for numerical analysis using FLAC computer code. This cross section intersected the axis of the heated drift at middistance between the thermal bulkhead and the terminus of the heated drift. The two-dimensional numerical models developed, based on this cross section, simulated a plane strain condition. The FLAC models developed had a dimension of 400 m [1,312.3 ft] in width and height with the origin located at the lower-left corner of the models. A 5-m [16.4-ft] diameter circular drift was constructed with its center located 200 m [65.6 ft] from the left boundary and 300 m [984.2 ft] from the bottom of the model domain.

The FLAC models developed consisted of 400 × 400 grids. The distance between two neighboring grids in both horizontal and vertical directions was 1 m [3.28 ft] except for grids near the heated drift. The grid distance around the heated drift was adjusted to better describe the shape of the drift. Figure 3-5 shows a closeup of the FLAC model with grids in the vicinity of the heated drift.

Fixed horizontal displacement boundaries were applied to the sides and a fixed vertical displacement boundary to the bottom of the model. At the top of the model, a constant stress was applied to represent the remaining overburden. Initial stresses consistent with overburden depth were applied as initial conditions.

The FLAC models developed included three generalized thermal-mechanical lithologic units: Topopah Spring upper lithophysal unit on the top, Topopah Spring middle nonlithophysal unit in the middle, and Topopah Spring lower lithophysal unit on the bottom. The Topopah Spring middle nonlithophysal zone simulated was 37 m [121.4 ft] thick, and its bottom is located 282 m [925.2 ft] from the bottom of the model domain.

3.3 Material Properties Input

Material properties needed for conducting the continuum analyses in this study included (i) rock deformation modulus, (ii) Poisson's ratio, (iii) strength properties, and (iv) thermal expansion coefficient. All data were provided by the Task 2 technical monitor research team through several CRWMS M&O reports. These properties are discussed briefly in the following sections, and relevant references of the reports are provided as appropriate.

3.3.1 *In-Situ* Deformation Modulus

The *in-situ* deformation modulus of a rock mass is an important parameter in any form of numerical analysis and in the interpretation of monitored deformation around the heated drift. The intact rock Young's moduli, Poisson's ratios, and bulk densities for the three lithologic zones are listed in Table 3-1 (CRWMS M&O, 1997c, 1999). Also included in Table 3-1 are standard deviation values for the corresponding parameters.

Table 3-1. Intact Rock Material Properties (CRWMS M&O, 1997c, 1999)

	Upper Lithophysal Zone	Middle Nonlithophysal Zone	Lower Lithophysal Zone
Bulk Density, kg/m^3 [lb/ft^3]	2,160 ± 80 [134.8 ± 5.0]	2,250 ± 70 [140.5 ± 4.4]	2,250 ± 60 [140.5 ± 3.7]
Young's Modulus, GPa [10^6 psi]	20.36 ± 6.75 [2.95 ± 0.98]	33.03 ± 5.94 [4.79 ± 0.86]	33.03 ± 5.94 [4.79 ± 0.86]
Poisson's Ratio	0.23 ± 0.07	0.21 ± 0.04	0.21 ± 0.04

Discontinuities in a rock media tend to soften and weaken the media. Therefore, the deformation modulus of a rock mass could be substantially different from that of the intact rocks than from the rock-mass. The extent of difference in the deformation modulus depends on the intensity and the surface properties of joints present in the host rock. A reasonable approach to determine the rock-mass deformation modulus is to conduct tests in the field. This approach, however, is often difficult to perform and is expensive. Attempts have been made to develop methods for estimating its value, based on rock-mass classifications. The two most widely used rock-mass classifications are RMR (Bieniawski, 1976, 1989) and Q (Barton et al., 1974) methods. Both methods rely heavily on joint information.

It should be noted, however, large variations are associated with the characterization of joint intensity and joint properties. Consequently, determination of rock-mass deformation modulus by taking into consideration the presence of joints will similarly involve large variations. To account for these variations, CRWMS M&O (1999) attempted to quantify these variations by representing the rock-mass for each thermal-mechanical unit with a method called rock-mass quality categories. For each rock unit, five rock-mass categories were defined based on cumulative frequency of occurrence, and the corresponding rock-mass properties were estimated using full peripheral-fracture mapping data. Table 3-2 lists the rock-mass Young's modulus of each rock-mass quality category for Topopah Spring Welded Tuff Thermal-Mechanical Units 1 and 2. It can be shown that the rock-mass Young's modulus varied more than a factor of 2 from Rock-Mass Quality Category 1 to 5. It should be noted that the Upper Lithophysal litho-stratigraphic unit is part of the Topopah Spring Welded Tuff Thermal-Mechanical Unit 1 and the Middle Nonlithophysal and Lower Lithophysal litho-stratigraphic units are part of the Topopah Spring Welded Tuff Thermal-Mechanical Unit 2. In this study, the corresponding rock-mass Young's moduli were used for modeling accordingly.

Table 3-2. Rock-Mass Young's Modulus (CRWMS M&O, 1999)

Thermal-Mechanical Unit	Rock-Mass Quality Category	Cumulative Frequency of Occurrence	Rock-Mass Young's Modulus, GPa [10^6 psi]
Topopah Spring Welded Tuff Unit 1	1 (Sensitivity Case 5)	5%	9.03 [1.31]
	2 (Basecase 2)	20%	14.28 [2.07]
	3	40%	19.40 [2.81]
	4	70%	20.36 [2.95]
	5 (Sensitivity Case 6)	90%	20.36 [2.95]
Topopah Spring Welded Tuff Unit 2	1 (Sensitivity Case 5)	5%	8.98 [1.30]
	2 (Basecase 2)	20%	12.02 [1.74]
	3	40%	14.77 [2.14]
	4	70%	18.92 [2.74]
	5 (Sensitivity Case 6)	90%	24.71 [5.58]

The FLAC computer code accepts bulk and shear moduli (K and G) as material properties input. A FISH function was prepared to calculate K and G using the following equations:

$$K = \frac{E}{2(1+\nu)} \tag{3-1}$$

and

$$G = \frac{E}{3(1-2\nu)} \tag{3-2}$$

where E and ν are Young's modulus and Poisson's ratio, respectively.

3.3.2 Strength Properties

Another important group of parameters that support numerical analysis of the behavior of geologic media are strength properties. The intact rock strength properties are provided in Table 3-3. The FLAC modeling used cohesion as input for failure/yielding assessment. The uniaxial compressive strength listed in Table 3-3 was not directly used. However, it was used to determine cohesion for sensitivity analysis which will be discussed in detail later.

Determination of rock-mass strength properties is equally if not more difficult than the rock-mass deformation modulus. Rock-mass quality category approach was used to quantify rock-mass strength properties and associated uncertainties and variability. Table 3-4 lists the rock-mass strength properties for the two thermal-mechanical units mentioned previously. Note that in this qualification system, the rock-mass with higher rock-mass quality category number is relatively stronger than those with smaller rock-mass quality designations.

Table 3-3. Intact Rock Strength Properties (CRWMS M&O, 1999; Mean Values were Used)

Thermal-Mechanical Unit	Cohesion, MPa [psi]	Uniaxial Compressive Strength, MPa [psi]	Tensile Strength, MPa [psi]	Friction Angle, degree	Dilation Angle, degree
Topopah Spring Welded Tuff Unit 1	12.65 [1,834.3]	58.22 ± 30.69 [8,441.9 ± 4,450.1]	5.48 ± 2.32 [794.6 ± 336.4]	47.45	23.73
Topopah Spring Welded Tuff Unit 2	38.69 [5,610.1]	167.90 ± 65.53 [24,345.5 ± 9,501.9]	8.91 ± 3.39 [1.292 ± 491.6]	48.15	24.08

Table 3-4. Rock-Mass Strength Properties (CRWMS M&O, 1999)						
Thermal-Mechanical Unit	**Rock-Mass Quality Category**	**Cumulative Frequency of Occurrence**	**Cohesion, MPa [psi]**	**Tensile Strength, MPa [psi]**	**Friction Angle, degree**	**Dilation Angle, degree**
Topopah Spring Welded Tuff Unit 1	1 (Sensitivity Case 5)	5%	1.1 [159.5]	0.90 [130.5]	44	22
	2 (Basecase 2)	20%	1.4 [203.0]	1.13 [163.9]	46	23
	3	40%	1.7 [246.5]	1.35 [195.8]	46	23
	4	70%	2.1 [304.5]	1.69 [245.1]	47	24
	5 (Sensitivity Case 6)	90%	2.9 [420.5]	2.26 [327.7]	47	24
Topopah Spring Welded Tuff Unit 2	1 (Sensitivity Case 5)	5%	1.9 [275.5]	1.16 [168.2]	56	28
	2 (Basecase 2)	20%	2.3 [333.5]	1.36 [197.2]	57	29
	3	40%	2.6 [377.0]	1.54 [223.3]	57	29
	4	70%	3.2 [464.0]	1.82 [263.9]	58	29
	5 (Sensitivity Case 6)	90%	3.9 [565.5]	2.22 [321.9]	58	29

Similar to the selection of Young's modulus values for FLAC modeling, the strength properties for the Upper Lithophysal litho-stratigraphic unit was assumed to be the same as the Topopah Spring Welded Tuff Thermal-Mechanical Unit 1 and the Middle Nonlithophysal litho-stratigraphic unit was the same as the Topopah Spring Welded Tuff Thermal-Mechanical Unit 2. However, the Lower Lithophysal litho-stratigraphic unit might not be as strong as the Middle Nonlithophysal litho-stratigraphic unit even though these two units were grouped in the same thermal-mechanical unit (Topopah Spring Welded Tuff Thermal-Mechanical Unit 2). The Lower Lithophysal litho-stratigraphic unit contains voids of various sizes as opposed to the Middle Nonlithophysal litho-stratigraphic unit, which does not contain large voids. It is, therefore, reasonable to assume that the former is relatively weaker than the latter. Consequently, using the same strength properties as the Middle Nonlithophysal unit for the Lower Lithophysal unit may not be appropriate. No strength data for the Lower Lithophysal litho-stratigraphic unit are readily available; therefore, the strength properties for the Topopah Spring Welded Tuff Thermal-Mechanical Unit 1 were used for the purpose of this study.

Comparison of Tables 3-3 and 3-4 indicates that the rock-mass friction angles for the Topopah Spring Welded Tuff Thermal-Mechanical Unit 2 appear to be larger than the intact-rock friction angle. It is difficult to imagine that the rock-mass friction angle can be larger than the intact one. Investigation in this area is not abundantly available. In this study, if the rock-mass friction angle to be used for analysis was larger than the intact-rock friction angle, the intact-rock friction angle was used to represent the rock-mass friction angle. In a similar fashion, the rock-mass dilation angle was also adjusted to represent the intact-rock dilation angle to be consistent.

3.3.3 Thermal Expansion Coefficient

The thermal expansion coefficients for the three litho-stratigraphic units modeled in this study are provided in Table 3-5 (CRWMS M&O, 1997c). These data were determined based on laboratory experiments. It can be observed that the thermal expansion coefficient for each of the litho-stratigraphic units are temperature dependent. The thermal expansion coefficient varies more than a factor of 5 when the temperature is increased from 25 to 300 °C [77 to 572 °F].

The temperature-dependent nature of the thermal expansion coefficients listed in Table 3-5 was used in the FLAC modeling. Since the thermal expansion coefficient was expressed as a step function, a 1°C [1.8 °F] gap between steps was provided as FLAC input. Within this gap, the thermal expansion coefficient was linear interpolated using the step values at the two ends. Also, in this study, the thermal expansion coefficient for both intact rock and rock mass were assumed the same. The thermal expansion coefficient corresponding to temperatures higher than 300 °C [572 °F] is not available; the value associated with 275–300 °C [527–572 °F] was used in the analysis.

3.4 Temperature Input

As discussed previously, temperatures were measured at approximately 2,662 locations within the drift-scale heater test block by CRWMS M&O. Temperature measurements in the rock and from wing heaters were used by CRWMS M&O in developing the temperature distributions in the rock at 2-day intervals. These generated temperature distribution data were provided to the research teams involved in the modeling effort of Task 2C of the DECOVALEX III project. The dimensions of the block used for the development of temperature distributions were 70 m [229.7 ft] wide in the *x*-direction, 60 m [196.8 ft] long in the *y*-direction (axis along the heated drift), and 70 m [229.7 ft] high in the *z*-direction. The center of the block is located at the center of the heated drift approximately 25 m [82 ft] from the thermal bulkhead. Ambient temperatures {approximately 24 °C [75 °F]} were applied to the boundaries of the block to develop temperature distribution. The temperature data were generated at intervals of 1 m [3.28 ft] along all three directions using the three-dimensional gridding capabilities of Earth Vision software by Dynamic Graphics Inc.

Table 3-5. Thermal Expansion Coefficient Data {10^{-5}/°C [10^{-5}/°F]} (CRWMS M&O, 1999)						
Litho-Stratigraphic Unit	**25–50 °C [77–154 °F]**	**50–75 °C [154–231 °F]**	**75–100 °C [231–308 °F]**	**100–125 °C [308–385 °F]**	**125–150 °C [308–462 °F]**	**150–175 °C [462–539 °F]**
Upper Lithophysal	7.41 [4.12]	8.43 [4.68]	8.89 [4.94]	9.52 [5.29]	10.86 [6.03]	13.51 [7.51]
Middle Nonlithophysal	6.89 [3.83]	8.45 [4.69]	8.95 [4.97]	9.50 [5.28]	10.12 [5.62]	10.95 [6.08]
Lower Lithophysal	6.41 [3.56]	8.15 [4.53]	8.77 [4.87]	9.12 [5.07]	9.87 [5.48]	10.75 [5.97]
Litho-Stratigraphic Unit	**175–200 °C [539–616 °F]**	**200–225 °C [616–693 °F]**	**225–250 °C [693–770 °F]**	**250–275 °C [770–847 °F]**	**275–300 °C [847–924 °F]**	
Upper Lithophysal	19.38 [10.77]	29.34 [16.30]	32.35 [17.97]	40.16 [22.31]	48.83 [27.13]	
Middle Nonlithophysal	12.09 [6.72]	14.57 [8.09]	19.45 [10.81]	27.24 [15.13]	41.56 [23.09]	
Lower Lithophysal	12.55 [6.97]	15.14 [8.41]	25.19 [13.99]	26.15 [14.53]	33.40 [18.56]	

In this study, thermal load was calculated based on the temperature distribution at the cross section 23 m [75.5 ft] from the thermal bulkhead coinciding with the location of numerical models.

Figure 3-6 shows the contours of the temperature distribution on a vertical cross section at 23 m [75.5 ft] from the thermal bulkhead of the heated drift after 4 years of heating. The two high-temperature concentration zones {with temperatures higher than 250 °C [482 °F] in Figure 3-6} appeared to be at locations below the outer wing heaters, which were 0.25 m [0.82 ft] below the springline, on both sides of the heater drift. The zones with the highest temperatures were approximately 2 m [6.56 ft] below the springline. Intuitively, these zones should be at or close to the wing heaters. It is not clear why the temperature shift took place. Figure 3-7 shows the same contours as in Figure 3-6 except with a shift of 2 m [6.56 ft] upward. Notice that the zones of highest temperature {> 300 °C [572 °F]} were located approximately at the springline. The temperature distribution pattern shown in Figure 3-7 appears to be consistent with those predicted temperature distribution results presented in Task 2A.[2] In the interest of this study, temperature distributions shown in both figures were used for the

[2] DECOVALEX III Project Task 2A Interim Report (Revised) Thermal-Hydrological Predictive Simulation of the Yucca Mountain Project Drift Scale Test. Compiled by R.N. Datta, URS Corporation. 2002.

study and the possible effects these two distributions analyzed. To facilitate discussions on modeling results in the latter section, the use of temperature distribution without shifting (Figure 3-6) was named Temperature Option 1, and the use of temperature distribution with location shifting (Figure 3-7) was called Temperature Option 2.

3.5 Base and Sensitivity Analysis Cases

Two basecases were established for Task 2C modeling activities. For Basecase 1, the three litho-stratigraphic units were treated as intact rocks in the analysis. The material and strength properties used for these three units were the mean values presented in Tables 3-1 and 3-3. For Basecase 2, the three litho-stratigraphic units were treated as rock masses. The material and strength properties for Rock-Mass Quality Category 2 rock listed in Tables 3-2 and 3-4 were used for Basecase 2. Rock-Mass Quality Category 2 was selected as a basecase because CRWMS M&O (1999) reported that limited rock-mass modulus obtained from field tests for the Topopah Spring Welded Tuff Thermal-Mechanical Unit 2 was smaller than the rock-mass Young's modulus designated for the Topopah Spring Welded Tuff Thermal-Mechanical Unit 2 (CRWMS M&O, 1999). Toward this end, Rock-Mass Quality Category 2 might be reasonable to represent rock-mass quality for at least the Middle Nonlithophysal litho-stratigraphic unit.

Besides the two basecases, several sensitivity analyses were also performed. The sensitivity analyses for Basecase 1 focused on investigating the effects of intact-rock Young's modulus and strength properties (mainly cohesion and tensile strength) on displacements and permeability changes at predetermined locations.

Table 3-6 shows the sensitivity analyses cases studied along with the parameters varied from Basecase 1. Sensitivity analysis on friction angle was performed because the associated standard deviation data were not available. The relevant values for Basecase 1 were also provided in the table for clarity. The parameter values shown in the table for the sensitivity cases were varied from the mean values used in Basecase 1 either one standard deviation greater or smaller to examine the potential effects of variability associated with the determination of these parameters. As can be observed in Table 3-3, standard deviation is not available for intact-rock cohesion, C_o. In this case, uniaxial compressive strength, σ_c, provided in Table 3-4, was used to estimate cohesion, C_o, for the three litho-stratigraphic units modeled using the following equation

$$C_o = \frac{\sigma_c(1-\sin\phi)}{2\cos\phi} \tag{3-3}$$

where ϕ is intact-rock friction angle.

Table 3-6. Cases of Sensitivity Analyses with Respect to Basecase 1				
Case	**Rock Unit**	**Young's Modulus, GPa [10^{-6} psi]**	**Cohesion, MPa [psi]**	**Tensile Strength, MPa [psi]**
Basecase 1	Upper Lithophysal	20.36 [2.95]	12.65 [1,834.3]	5.48 [794.6]
	Middle Nonlithophysal	33.03 [4.97]	38.69 [5,610.1]	8.91 [1,292]
	Lower Lithophysal	33.03 [4.97]	12.65 [1,834.3]	5.48 [794.6]
Sensitivity Case 1	Upper Lithophysal	13.61 [1.97]	Same As Basecase 1	Same As Basecase 1
	Middle Nonlithophysal	27.09 [3.93]	Same As Basecase 1	Same As Basecase 1
	Lower Lithophysal	27.09 [3.93]	Same As Basecase 1	Same As Basecase 1
Sensitivity Case 2	Upper Lithophysal	27.11 [3.93]	Same As Basecase 1	Same As Basecase 1
	Middle Nonlithophysal	38.97 [5.65]	Same As Basecase 1	Same As Basecase 1
	Lower Lithophysal	38.97 [5.65]	Same As Basecase 1	Same As Basecase 1
Sensitivity Case 3	Lower Lithophysal	13.61 [1.97]	5.36 [777.20]	3.16 [458.20]
	Middle Nonlithophysal	27.09 [3.93]	19.57 [2,837.65]	5.52 [800.40]
	Lower Lithophysal	27.09 [3.93]	5.36 [777.2]	3.16 [458.2]
Sensitivity Case 4	Lower Lithophysal	27.11 [3.93]	17.33 [2,512.85]	5.48 [794.60]
	Middle Nonlithophysal	38.97 [5.65]	44.63 [6,471.35]	12.30 [1,783.50]
	Lower Lithophysal	38.97 [5.65]	17.33 [2,512.85]	5.48 [794.60]

For Basecase 2, sensitivity of rock-mass quality to the displacement and permeability under heated conditions were analyzed by considering Rock-Mass Quality Categories 1 and 5 (Sensitivity Cases 5 and 6). The material and strength properties for these two rock-mass quality categories were listed in Tables 3-2 and 3-4. All basecases and sensitivity cases were analyzed under both temperature options as defined in Section 3.4.

3.6 Modeling Procedures

FLAC simulation started by obtaining an initial model static-state equilibrium considering the *in-situ* and applied stresses for representing the remaining overburden on top of the FLAC models. After the initial equilibrium was reached, the drift was excavated by assigning the bulk and shear moduli of the zones within the drift boundary to 0. After a new static-state condition in the presence of excavation was established, the thermal-mechanical analyses began. To perform thermal-mechanical analyses, temperatures were applied to the FLAC models in the form of temperature changes after 3 months, 6 months, 9 months, 1 year, 2 years, 3 years, and 4 years of heating. After the application of temperature changes at each predetermined thermal time, the stresses and displacements of a FLAC model were updated through a mechanical cycling process until a new equilibrium was reached. After the completion of each thermal-mechanical run, the displacements and permeability variations at predetermined locations, as discussed in Section 3.1 and presented in Figures 3-3 and 3-4, were calculated using separate FISH functions.

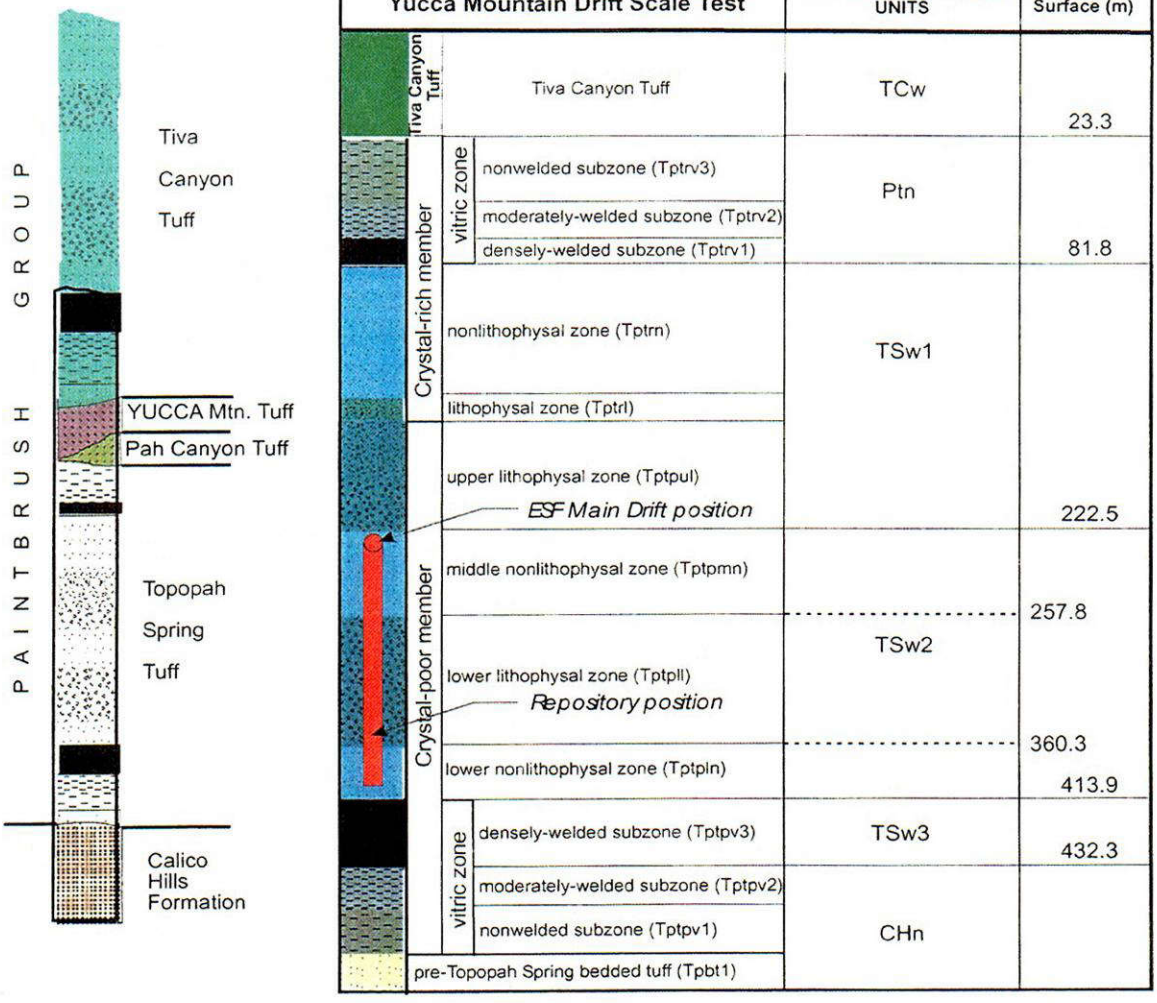

Figure 3-1. Stratigraphic data for drift-scale heater test (provided by Task 2 technical monitor research team)

C01

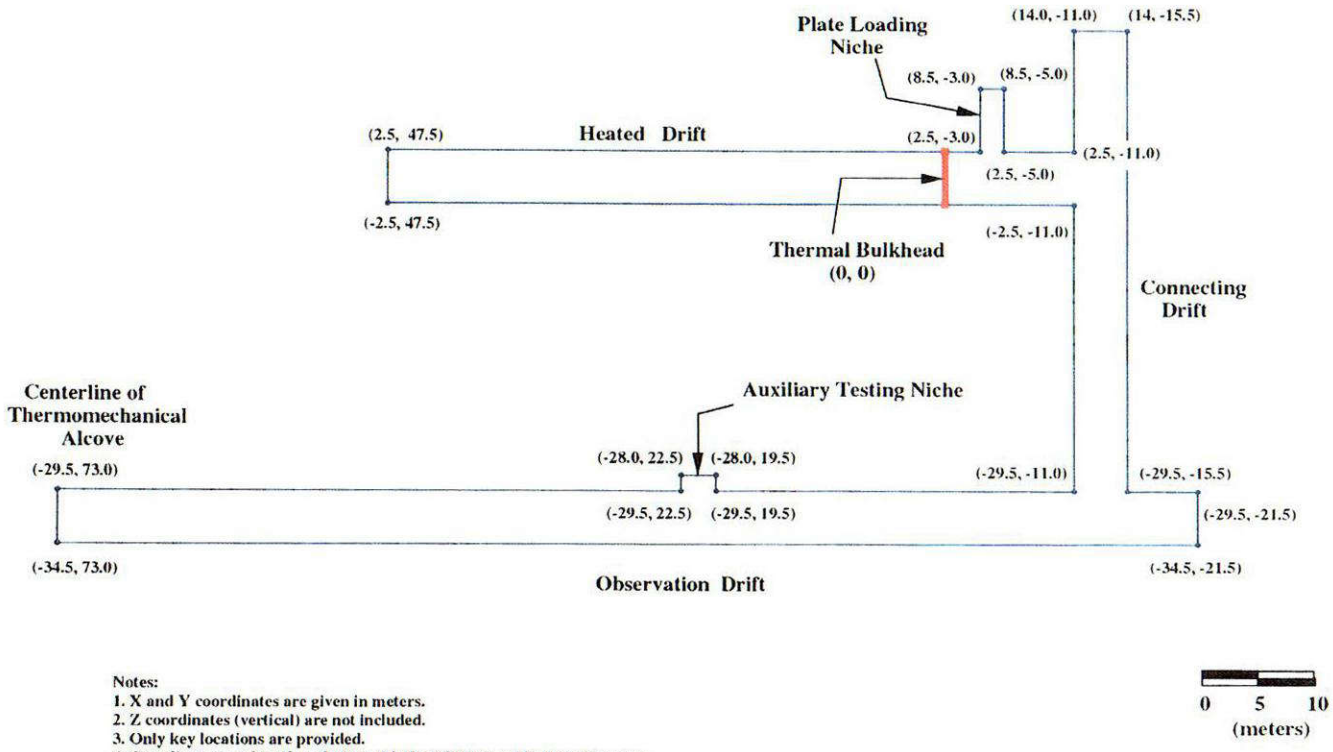

Notes:
1. X and Y coordinates are given in meters.
2. Z coordinates (vertical) are not included.
3. Only key locations are provided.
4. Coordinates are based on design with the following as-builts tolerances:
   Horizontal alignment = - 0 to + 0.5m
   All other = - 0 to + 0.3m

0 5 10
(meters)

Figure 3-2. Plan view schematic of the primary components of the drift-scale heater test region

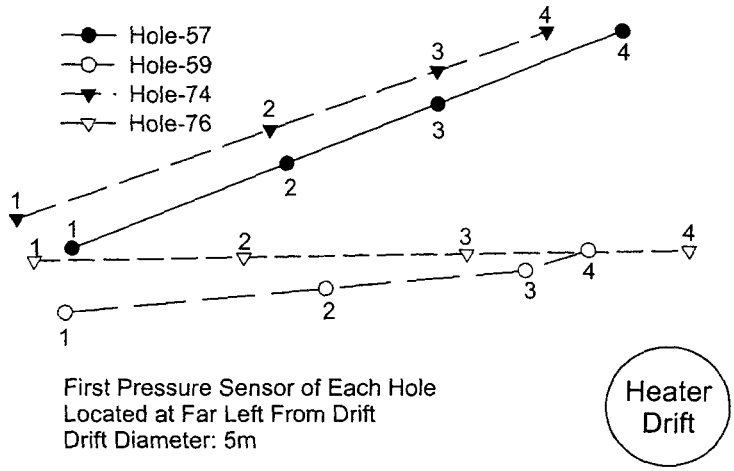

Figure 3-3. Relative Location of Hydrological Measurement Holes with respect to drift

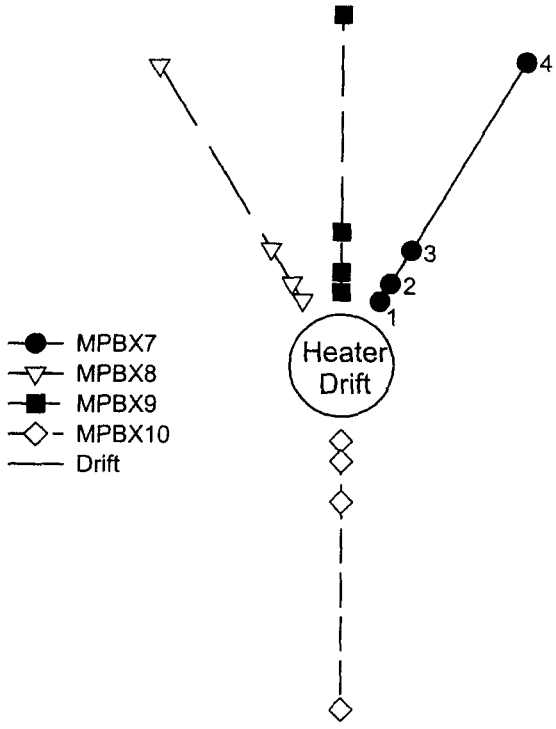

Figure 3-4 Relative positions of multiple-position extensometer anchors with respect to drift

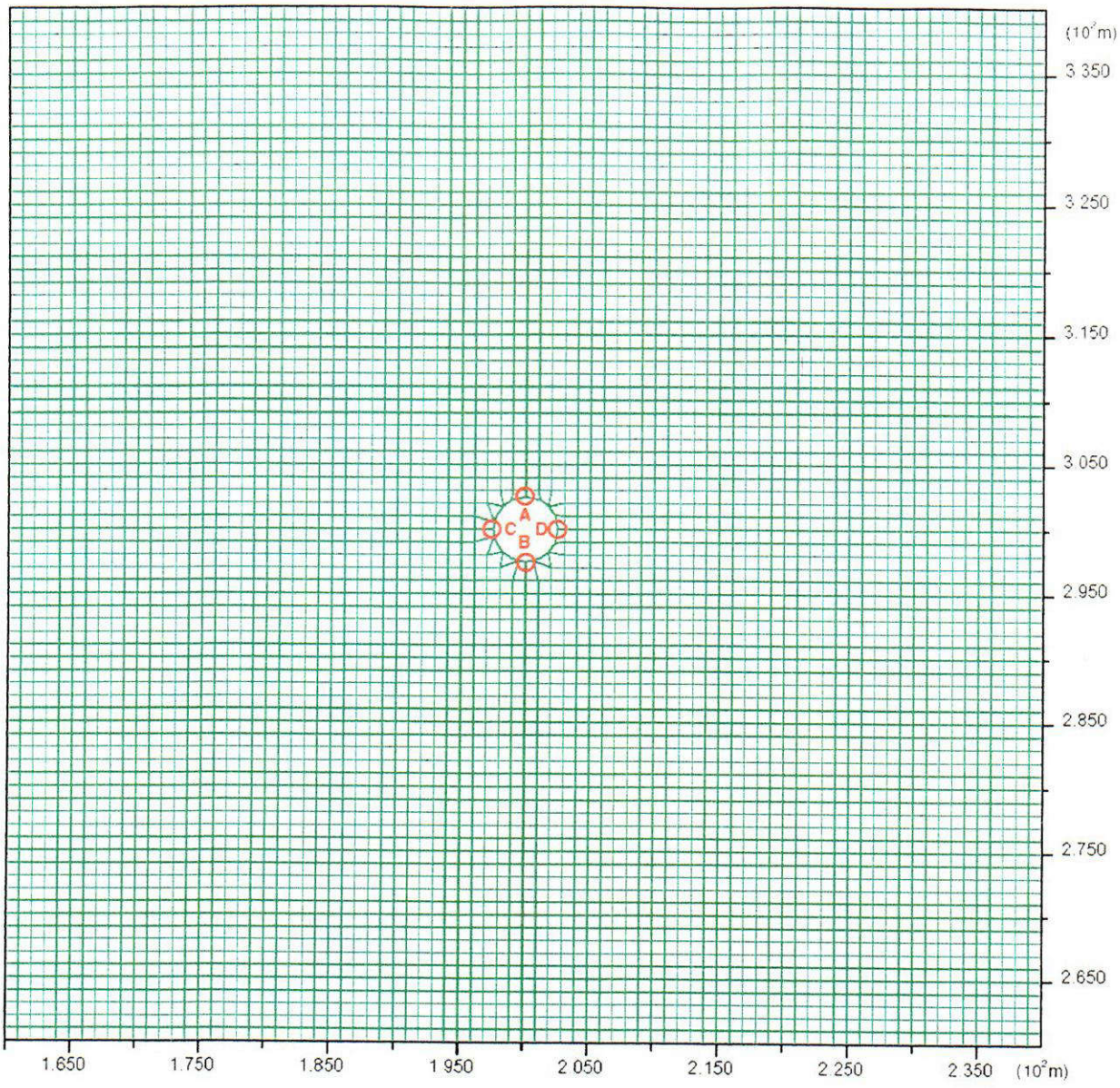

Figure 3-5. Close-up of a two-dimensional grid discretization of the heated drift

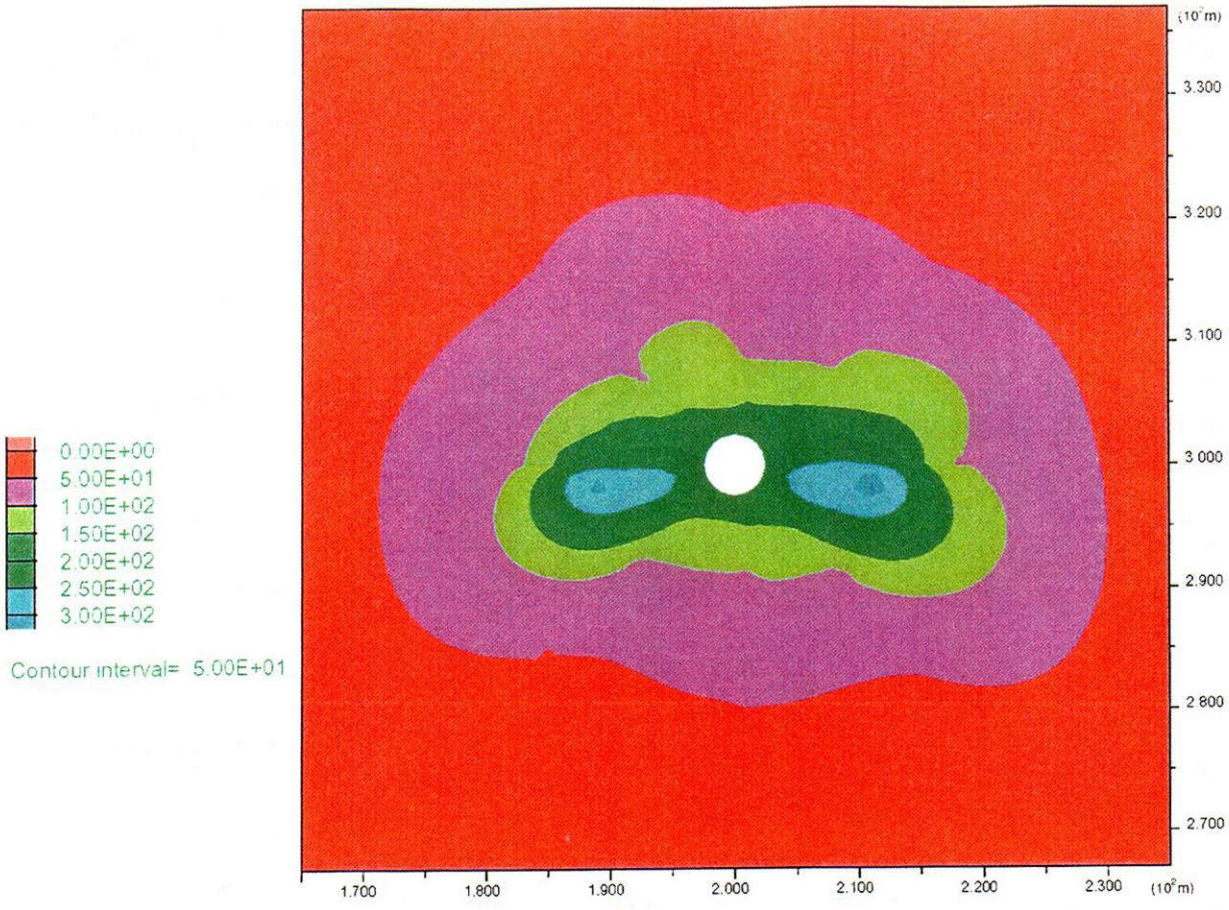

Figure 3-6. Temperature contour, 23 m [75.5 ft] from the thermal bulkhead after 4 years of heating

C02

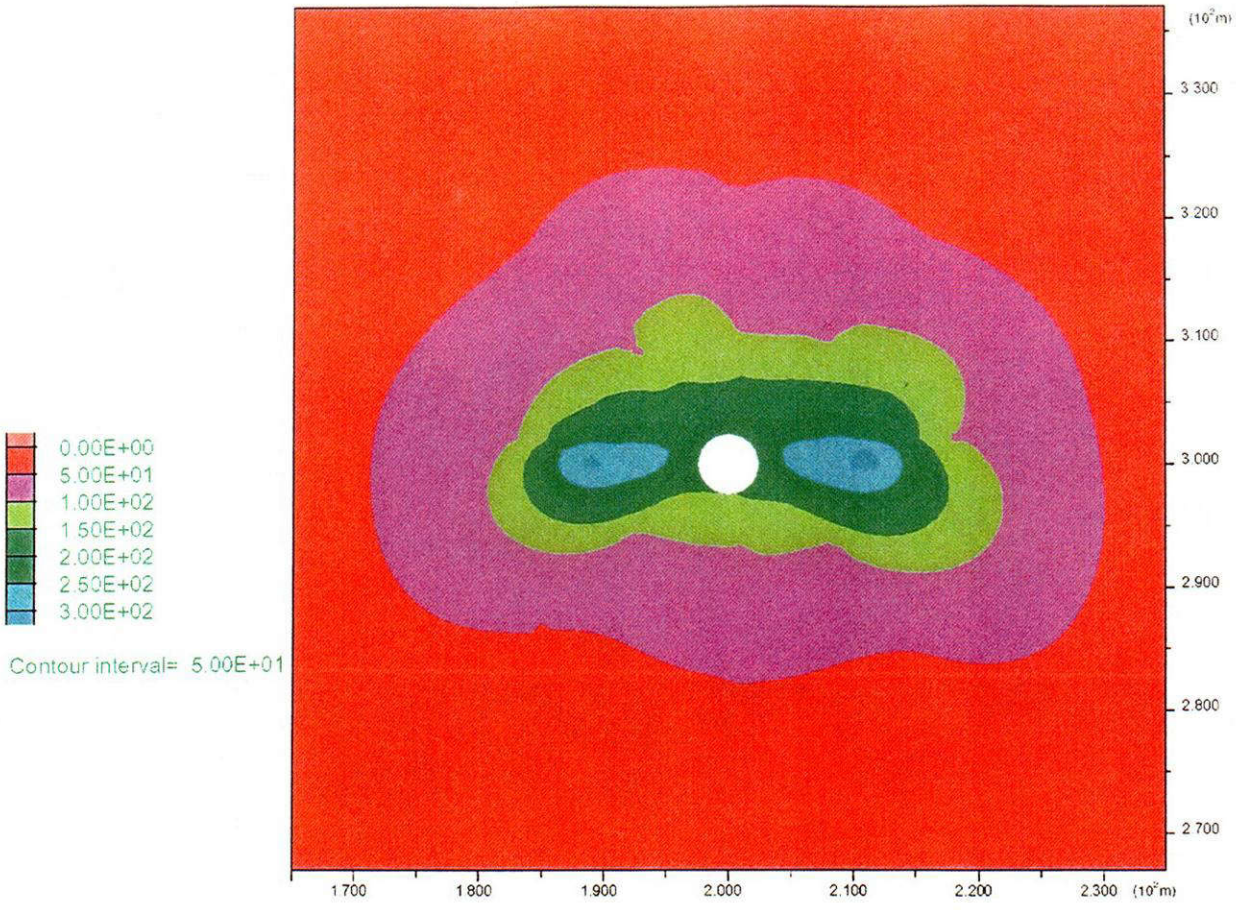

Figure 3-7. Temperature contour, 23 m [75.5 ft] from the thermal bulkhead after 4 years of heating {Temperature distribution was shifted upward by 2 m [6.56 ft]}

C03

4 MODELING RESULTS

A number of cases were analyzed, as discussed in Section 3.5. The objectives of the analyses were to examine thermally induced mechanical responses and thermal-mechanical effects on rock-mass permeability of the drift-scale heater test. The modeling results of thermally induced mechanical responses are discussed in Section 4.1, and the results of thermal-mechanical effects on permeability are discussed in Section 4.2.

The discussions in this section are focused on the thermal times at 3 months, 1 year, and 4 years. These thermal times were specified by the Task 2 technical monitor research team to facilitate comparison of results with the measured data and among the research teams.

4.1 Modeling Results of Thermally Induced Mechanical Responses

The effects of temperature were examined in terms of principal stresses, extent of yielding, rock deformation, and roof and wall convergences. These effects are discussed in the following sections.

4.1.1 Principal Stresses

Figures 4-1 and 4-2 show the contours of maximum and minimum principal stresses for Basecase 1 using Temperature Option 1 at the thermal times of 3 months, 1 year, and 4 years. The figures indicate that both maximum and minimum principal stresses increased with time because of increase in temperature. As expected, the high-stress zones for both maximum and minimum principal stresses coincided, in general, with the high-temperature zones. The maximum principal stress experienced at the end of 4 years of heating was more than 125 MPa [1.81×10^4 psi], which was 20–25 times the *in-situ* maximum principal stress before excavation. Similarly, the minimum principal stress at the end of 4 years of heating was more than 70 MPa [1.02×10^4 psi], which was 47–50 times the *in-situ* minimum principal stress before excavation. An extensive tensile stress (positive stress) zone can be observed in Figure 4-2. This tensile zone expanded outward from the heated drift with time. Similar observations apply to the case using Temperature Option 2. Furthermore, the patterns of the principal stress distributions generated for Basecase 1 using both temperature options do not differ much [Figure 4-1(c) versus Figure 4-3(a) and Figure 4-2(c) versus Figure 4-3(b)].

The maximum and minimum principal stress distributions for Basecase 2 (Figures 4-4 and 4-5) were considerably different from those for Basecase 1 (Figures 4-1 and 4-2). Although the high-stress zones coincided with the high temperature zones—same as observed for Basecase 1, but for Basecase 2—the magnitudes were much smaller {more than 50 MPa [0.73×10^4 psi] for the maximum principal stress and 30 MPa [0.44×10^4 psi] for the minimum principal stress after 4 years of heating [Figure 4-4(c)]}. This difference in principal stresses was understandable because the Young's modulus for the rock mass (Middle Nonlithophysal zone) in Basecase 1 was approximately one-third of that for the intact rock. The thermally induced stresses are directly proportional to the Young's modulus of a material as indicated in Eq. (2-6). Also, the tensile stress zones experienced in Basecase 2 were much smaller than those observed for Basecase 1. Similar to the observation for Basecase 1, temperature options did not significantly alter the pattern of the principal stress distributions for Basecase 2.

4.1.2 Yielding of Rocks

To assess yielding/failure and accumulated plastic strains in rock mass, a Mohr-Coulomb failure criterion was used. In the criterion, a nonassociated flow rule was used to describe the shear potential function, and an associated rule was used for tensile potential function. The strength properties used in the criterion included cohesion, tensile strength, friction angle, and dilation angle. All the relevant strength properties for each case studied are provided in Tables 3-2, 3-4, and 3-6.

4.1.2.1 Results for Basecase 1 and Related Sensitivity Cases

After drift excavation, no rock yield was observed for Basecase 1. Yield zones in the rock started to develop and grow gradually as temperature increased with duration of heating (Figures 4-6 and 4-7). The results shown in Figure 4-6 are with Temperature Option 1 and Figure 4-7 are with Temperature Option 2. As can be observed, most yielding was concentrated around the sidewalls and four corners of the heated drift and an area above the outer wing heater located at left side of the heated drift (viewing from the thermal bulkhead into the heated drift). The yield zones observed in this case were all located in the Middle Nonlithophysal litho-stratigraphic unit. Some differences in yielding caused by the two temperature options can be observed. The differences were not large.

Effect of Variation in Young's Modulus

Two sensitivity analyses (Sensitivity Cases 1 and 2) were conducted with respect to Basecase 1 to evaluate the effects of variation in intact-rock Young's modulus. The Young's moduli used in these two cases are provided in Table 3-6 as Sensitivity Cases 1 and 2. No yield zones were found for these two sensitivity cases after the completion of excavation. As with Basecase 1, when temperature in the rock surrounding the drift heated up, yield zones in the rock began to develop and grow. However, the yield zones developed for the three cases were quite different (Figures 4-6 and 4-7 for Basecase 1, Figures 4-8 and 4-9 for Sensitivity Case 1, and Figures 4-10 and 4-11 for Sensitivity Case 2).

For the case with smaller Young's modulus (Sensitivity Case 1), the yield zones developed were limited to surrounding the heated drift. Some amount of yielding was observed in the drift roof as compared to Basecase 1 where no roof yielding was found. Furthermore, there was no yield zone in the area above the outer wing heater as was observed in Basecase 1. For the case with larger Young's modulus (Sensitivity Case 2), the yield zones in the Middle Nonlithophysal litho-stratigraphic unit were located in the same areas as Basecase 1 except that the zones were bigger and the drift roof yielded also.

Extensive tensile zones started to develop in the Upper and Lower Lithophysal litho-stratigraphic units between 1 and 2 years of heating [Figure 4-10(c)] and became much larger after 4 years of heating [Figure 4-10(d)]. Note that the bedding plane between the Lower Lithophysal and Middle Nonlithophysal units was at 282 m [925.2 ft] for the FLAC model and 319 m [1,046.6 ft] between the Middle Nonlithophysal and Upper Lithophysal units. Development of these large tensile zones was directly the result of relatively smaller tensile strengths for the Upper and Lower Lithophysal litho-stratigraphic units as compared to the Middle Nonlithophysal litho-stratigraphic unit in which such large tensile yield zones were not present.

In general, the extent that yield zones for the case with smaller Young's modulus was smaller than that for the case with relatively larger Young's modulus is reasonable. Recall that the thermally induced stresses are directly proportional to Young's modulus as indicated in Eq. (2-6). Other things being equal, thermally induced stresses are higher for large Young's modulus than for small Young's modulus; consequently, the rock with large Young's modulus is more likely to yield than the one with small Young's modulus.

Effect of Variation in Strength Properties

Two other sensitivity analyses (Sensitivity Cases 3 and 4) were conducted to evaluate the effects of variation in intact rock cohesion and tensile strength. Figures 4-12 and 4-13 show the extent of yield zones with smaller strength properties (cohesion and tensile strength) (Sensitivity Case 3) than Sensitivity Case 1 with both temperature options, while Figures 4-14 and 4-15 show the yield zones with larger strength properties (Sensitivity Case 4) than Sensitivity Case 1.

Comparing the results for Sensitivity Cases 1, 3, and 4, it is clear that, in the temperature range of interest, the extent of yield zones is sensitive to the variation of strength properties. This observation is intuitive. Extensive yield zones developed in the Upper and Lower Lithophysal litho-stratigraphic units when the cohesion and tensile strength of these units were reduced. As can be observed in Sensitivity Case 3 with both temperature options (Figures 4-12 and 4-13), yield zone in the Upper Lithophysal zone occurred first between 9 months and 1 year of heating, and the yield zone in the Lower Lithophysal zone began to develop between 1 and 2 years of heating. The yield zone developed in the Upper Lithophysal unit also extended into the Middle Nonlithophysal unit [Figures 4-12(c) and 4-13(c)]. Other things being equal, for higher strength properties, the yield zones were limited to areas surrounding the heated drift [Figures 4-14(c) and 4-15(c)].

4.1.2.2 Results for Basecase 2 and Related Sensitivity Cases

Analyses on Basecase 2 and Sensitivity Cases 5 and 6 were conducted to evaluate the effects of rock-mass quality variations. As discussed in Section 3.5, the rock-mass properties used for Basecase 2 were corresponding to Rock-Mass Quality Category 2 and Sensitivity Cases 5 and 6 modeled Rock-Mass Quality Categories 1 and 5.

Immediately after excavation, yielding in the roof and on the sidewall of the drift was reported for Basecase 2 and Sensitivity Case 5, while very limited yielding was observed for Sensitivity Case 6. As the drift was heated up, extensive yield zones developed in all three cases (Figures 4-17, 4-18, and 4-19). The extent of yield zones in the three litho-stratigraphic units modeled, however, was larger for cases with higher rock-mass quality designations. With the best quality rock mass (designated as Rock-Mass Quality Category 5, Sensitivity Case 6), the yield zones developed after 4 years of heating in the Middle Nonlithophysal zone where the heated drift was located were much more significant [Figure 4-19(c)] than the ones observed for Basecase 2 [Rock-Mass Quality Category 2, Figure 4-18(c)] and Sensitivity Case 5 [Rock-Mass Quality Category 1, Figure 4-17(c)]. This observation is consistent with the findings reported by other researchers (e.g., Ofoegbu, 1999).

Comparing the mechanical and strength properties for the three Rock-Mass Quality Categories analyzed in this study (Tables 3-2 and 3-4), it can be concluded that there is a large difference in Young's modulus between Rock-Mass Quality Category 5 and Rock-Mass Quality Categories 1 and 2, while the difference in strength properties among them is relatively small. As discussed earlier, large thermally induced stresses are associated with high Young's modulus. Consequently, a rock mass with higher rock-mass quality designation is more prone to yield than the one with smaller rock-mass quality designation.

4.1.3 Displacement Prediction

Prediction of rock displacements at the anchor locations of four multiple-position extensometers (MPBX7 through MPBX10 shown in Figure 3-4) is one of the objectives of Task 2C. This section (Section 4.1.3) discusses the predicted displacement results and sensitivity analyses results.

4.1.3.1 Results for Basecase 1

Figure 4-20 shows the predicted displacements for Basecase 1 with Temperature Option 1 as a function of time in which rocks were modeled as intact rocks. As discussed in Section 3.1, each multiple-position extensometer contained four anchors. Anchor 1 was located closest to the heated drift, while Anchor 4 was the farthest. The anchor displacements presented in the figures discussed in this section are thermally induced displacements. Excavation-induced anchor displacements are not included. The positive displacement values in the figure indicated that, after deformation, the distance between anchors and the extensometer assembly heads located near the collar of the heated drift became larger than the original distance before heating started; the negative values indicated that the distance between the anchors and the assembly heads became smaller.

In general, the predicted displacements associated with the anchors of the two inclined multiple-position extensometers (MPBX7 and MPBX8) were the highest, while the displacements predicted for the anchors of the two vertical extensometers (MPBX9 and MPBX10) were relatively smaller with the smallest for the vertical extensometer located in the floor rock of the heated drift. The largest anchor displacement predicted was approximately 5.73 mm [0.23 in] for Anchor 4 of MPBX7 after 4 years of heating. The maximum displacement for MPBX8 was slightly smaller than that for MPBX7.

During the early stage of heating, Anchor 4 for both vertical extensometers (MPBX9 and MPBX10) moved closer to the heated drift before a positive displacement of the anchor took place after 1 to 2 years of heating. This phenomenon was likely because the temperature increase did not reach the regions where Anchor 4 was located until at the later stage of heating. As a result, any displacement associated with Anchor 4 was a direct response of thermal expansions of rock in the heated zone.

The displacements predicted for anchors of the extensometers using Temperature Option 2 (Figure 4-21) were quite different for those observed for Temperature Option 1 although the general trend was the same. The predicted displacements for the three extensometers located in the roof of the heated drift for Temperature Option 2 were larger than those for Temperature Option 1. The largest displacement predicted was approximately 8.8 mm [0.35 in] for Anchor 4 of MPBX7 after 4 years of heating. The displacements for the anchors of the vertical

extensometer (MPBX10) located in the floor rock of the heated drift was, on the other hand, even smaller compared with the predictions for Temperature Option 1. All four anchors for MPBX10 moved closer to the heated drift before positive displacements began some time after heating. Anchor 4 did not have a positive displacement until at a later stage of heating. It is not clear at this time the cause of this behavior.

4.1.3.2 Results for Basecase 2

Figures 4-22 and 4-23 illustrate the predicted displacements of the multiple-position extensometer anchors for Basecase 2 with Temperature Option 1 and Temperature Option 2. Consistent with the observations for Basecase 1, Temperature Option 2 tended to generate larger deformations than Temperature Option 1 in the rock mass surrounding the roof area of the heated drift, while the predicted anchor displacements in the rock mass at the bottom of the heated drift was relatively smaller. The maximum displacement predicted for Basecase 2 with Temperature Option 2 was approximately 12.54 mm [0.49 in] for Anchor 4 of MPBX7 after 4 years of heating. In general, the predicted displacements for Basecase 2 (rock units were modeled using rock-mass properties) were larger than the corresponding anchor displacements for Basecase 1 with the same temperature options (rock units were modeled using intact-rock properties). The displacements predicted for Anchor 4 of MPBX7 and MPBX8 using Temperature Option 1 were slightly smaller for Basecase 2 than those for Basecase 1. This observation might be related to the large yield zones developed in Upper and Lower Lithophysal units above and below the heated drift for Basecase 2, while there was none for Basecase 1. Dilations generated by yielding could have restricted somewhat the relative displacement between Anchor 4 and the assembly head of the relevant multiple-position extensometer.

4.1.3.3 Sensitivity Analyses with Respect to Basecase 1 and Sensitivity Case 1

Figures 4-24 and 4-25 show the effects of cohesion and tensile strength variations on rock deformation relative to Sensitivity Case 1 for both temperature options. Anchor displacements for MPBX7 and MPBX8 after 4 years of heating were displayed in the figures. In analyzing the effects of rock strength, both cohesion and tensile strength for all three rock units modeled were varied simultaneously by one standard deviation lower or higher from the mean corresponding value, which was used in Basecase 1. Using cohesion as the horizontal axis for both figures was a matter of choice. It should be noted also that the standard deviation data for intact-rock cohesion are not available. The variation in intact-rock cohesion was calculated from uniaxial compressive strength listed in Table 3-1. As can be observed from the figures, the effects of cohesion and tensile strength within the range of consideration on deformation of rock surrounding the heated drift were insignificant.

The effects of variations of Young's modulus relative to Basecase 1 appeared to be small as well within the range of variation (Figures 4-26 and 4-27). The middle point for each curve in the figures represents the result for Basecase 1. The only noticeable effect was related to displacement for Anchor 4 for both temperature options. The anchor displacement decreased with an increase in Young's modulus; the effect was relatively larger for Temperature Option 2 than for Temperature Option 1.

For the cases of modeling rock units using rock-mass properties, varying rock-mass quality designations produced substantially noticeable effects on rock-mass deformation in the heated

drift roof area for Temperature Option 2. Figures 4-28 and 4-29 show displacements of anchors for MPBX7 and MPBX8 for Temperature Options 1 and 2, respectively. In general, displacements of all anchors for MPBX7 and MPBX8 increased as the rock-mass quality designation number increased. Note that larger rock-mass quality designation numbers indicate higher rock-mass Young's modulus and strength (refer to Table 3-4 in Section 3.3.2). The displacement increase was relatively small for Temperature Option 1. For Temperature Option 2, however, the difference in displacement predicted could be as large as 4.78 mm [0.19 in] for Anchor 4 of MPBX7 when the rock-mass properties were changed from Rock-Mass Quality Category 1 to 5 (i.e., from the smallest to the largest rock-mass properties).

4.1.4 Drift Convergence

Another piece of information often used to assess stability of underground excavations and to determine ground support for underground excavations is convergence. Although this information is not required by Task 2C, it is presented here for completeness.

Figures 4-30 and 4-31 show roof-to-floor and wall-to-wall drift convergences as functions of time for Basecases 1 and 2, respectively. The roof-to-floor convergence was calculated between the two vertical points A and B shown in Figure 3-5, and the wall-to-wall convergence was calculated between two horizontal points C and D shown in the same figure. Points A and B were the intersections of drift vertical diameter to the drift, and points C and D were intersections of drift horizontal diameter (springline) to the drift. The positive values in the figures are indications of divergence (two points moved away from each other), while negative values are representations of convergence of two points.

As can be observed from these figures, the heated drift became slightly narrower and elongated as the heating process progressed for both temperature options. The high-temperature zones located at both sides of the drift were the contributor to the narrowing of the heated drift in the horizontal direction. The side boundaries of the models tended to restrict the heated rock mass to expand toward those two directions, while expansion into the heated drift was relatively easier. In the vertical direction, expansion was easier in the upward direction because no displacement restriction was imposed on the top boundary of the models; a stress boundary condition was applied to the top of the FLAC models. This boundary condition could explain why divergence occurred in the vertical direction. The roof-to-floor divergence and wall-to-wall convergence peaked after 3 years of heating and began to decrease gradually afterward. More roof-to-floor divergence and less wall-to-wall convergence were observed for Basecase 1 than Basecase 2.

For either basecase, Temperature Option 2 produced less roof-to-floor divergence but more wall-to-wall convergence. It can also be observed that temperature options had relatively more effect on roof-to-floor divergence than wall-to-wall convergence for Basecase 2, and the opposite was true for Basecase 1.

Figure 4-32 shows the potential effect of rock-mass quality on drift convergence. The effect of rock-mass quality on roof-to-floor divergence was small for both temperature options, however, it was relatively large on wall-to-wall convergence.

4.2 Modeling Results of Thermal-Mechanical Effects on Rock Permeability

4.2.1 Initial Fracture Porosity and Permeability Properties

One of the primary objectives of Task 2 was to predict the thermal-mechanical effects on rock-mass permeability. To achieve this objective, a continuum representation of the deformation-permeability model was developed. The mathematical form of the model is provided as Eq. (2-20) in Section 2.3.3. For convenience of discussion, Eq. (2-20) is repeated here.

$$k_f = k_{fo}\left(1+\frac{e_{ve}+e_{vi}}{\varphi_{fo}}\right)^3, \qquad e_{ve} \geq -R_L\varphi_{fo}$$
$$k_f = k_{fo}\left(1+\frac{-R_L\varphi_{fo}+e_{vi}}{\varphi_{fo}}\right)^3, \quad e_{ve} < -R_L\varphi_{fo} \tag{4-1}$$

where k_f is the permeability after deformation, k_{fo} is the reference fracture permeability for the reference fracture porosity φ_{fo}, e_{ve} is an elastic volumetric strain, e_{vi} is a plastic volumetric strain, and R_L is a fraction value that controls the magnitude of residual fracture porosity.

For this study, k_{fo} and φ_{fo} were assumed to be the initial values before a rock mass was disturbed by excavation or heating and R_L was assumed to be 0.05. Notice that the proposed continuum-deformation-permeability model is highly sensitive to the initial fracture porosity. The smaller the fracture porosity is, the bigger will be the increase in permeability. The initial fracture porosities and permeabilities for the three litho-stratigraphic units used in this study are listed in Table 4-1.

Table 4-1. Initial Fracture Porosities and Fracture Permeabilities (CRWMS M&O, 2001)

Litho-Stratigraphic Unit	Porosity	Permeability, m^2 [ft^2]
Upper Lithophysal	0.0066	5.50×10^{-13} [5.92×10^{-12}]
Middle Nonlithophysal	0.01	2.76×10^{-13} [2.97×10^{-12}]
Lower Lithophysal	0.011	1.29×10^{-12} [1.39×10^{-11}]

4.2.2 Modeling Results

4.2.2.1 Permeability Variation Caused by Excavation

Figures 4-33 through 4-36 show contours of ratio of permeability after drift excavation to the initial permeability for Basecase 1, Sensitivity Case 2, Basecase 2, and Sensitivity Case 6 with

Temperature Option 1, respectively. Permeabilities in all four figures were observed to increase in regions where the permeability ratio was greater than one with a decrease in regions where the ratio was smaller than one. Although the effects of excavation on permeability were different for various cases, they were, in general, very small. The change involved a reduction in permeability smaller than 20 percent as can be observed in Figures 4-33 through 4-36. Two regions also were reported to have experienced an increase in permeability. These regions were located in the roof and floor of the drift for all cases studied. These regions had a diameter approximately equal to the diameter of the drift. The maximum increase in permeability for Basecase 1 was slightly over 3 percent and slightly over 10 percent for Basecase 2. These regions were not shown in the figures.

It should be noted, for all cases, that there existed a small area located at the lower-left corner of the drift where a reduction of more than 80 percent was observed. The presence of this small area appeared to be the model artifact caused by, perhaps, the irregular grid patterns near the drift, and, because the area involved is small, it is not expected this artifact will affect the evaluation of regional permeability changes because of thermally induced rock deformation.

4.2.2.2 Variations of Permeability as a Function of Temperature

Figures 4-37 and 4-38 show the thermally induced deformation effects on rock permeability after 3 months, 1 year, and 4 years of heating for Basecases 1 and 2 with Temperature Option 1. As can be observed in the figures, permeability over a large region surrounding the heated drift was influenced by the thermally induced deformation. The two areas experiencing the large increases coincided with the locations of wing heaters on both sides of the heated drift for both cases. This observation is true for all other cases studied here.

These two higher permeability areas grew gradually as the heating progressed. After 4 years of heating, the areas with permeability 1.5 times the initial permeability were approximately 3 drift-diameters wide and 2 drift-diameters high, and the areas with permeability of twice the initial permeability were approximately 2 drift-diameters wide and 1 drift-diameter high. Areas with permeability three and four times the initial permeability also can be observed although these areas were much smaller. Temperature options did not make much difference in permeability distributions. The observations described for Temperature Option 1 were equally applied to Temperature Option 2.

There were differences in permeability distributions between Basecases 1 and 2; for example, the permeability reduction regions were much larger for Basecase 2 than for Basecase 1. The differences were relatively small, however.

4.2.2.3 Permeability Prediction at Specified Locations

Figures 4-39 through 4-42 show the permeability variations predicted at sensor locations in Hydrologic Holes 57, 59, 74, and 76 at various stages of heating for Basecase 1 with Temperature Option 1, and Figures 4-43 through 4-46 are permeability variations for the same hydrologic boreholes for Basecase 2. The results in these figures are presented in terms of distance of a sensor to the first sensor of the respective hydrologic boreholes. The relative locations of the hydrologic boreholes and sensors in each borehole were discussed in Section 3.1 and shown in Figure 3-3. Among the hydrologic boreholes, Holes 59 and 76 were

closer to the horizon of the wing heaters located on the left-hand side of the heated drift than Holes 57 and 74, with Hole 59 being the closest. It is, therefore, logical to expect the permeability increases predicted in Hydrologic Hole 59 to be the largest. The predicted results for both basecases studied confirmed this expectation. In general, permeability changes associated with Basecase 2 were slightly smaller than those for Basecase 1. The maximum increase in permeability predicted was approximately 43 percent for Basecase 1 after 4 years of heating as opposed to 38 percent for Basecase 2.

Predicted permeability changes for both basecases using Temperature Option 2 as input (the results for Basecase 1 are shown in Figures 4-47 through 4-50) were larger than those for Temperature Option 1 shown in Figures 4-39 through 4-42 for the four hydrologic boreholes. This finding was expected. As discussed in Section 3.4, Temperature Option 2 used the same temperature data provided by the Task 2 technical monitor research team except that the locations of the temperatures were shifted 2 m [6.56 ft] upward. This shift made the high-temperature zone for Temperature Option 2 closer to hydrologic boreholes of interest than Temperature Option 1. The maximum increase in permeability predicted with Temperature Option 2 was approximately 61 percent for Basecase 1 and 57 percent for Basecase 2 after 4 years of heating, approximately 20 percent more than the increase predicted with Temperature Option 1.

4.2.2.4 Sensitivity Analyses Results for Both Basecases 1 and 2

Figure 4-51 shows the effect of rock-mass quality on permeability for the cases of modeling rock units using rock-mass properties. Figures 4-52 and 4-53 show the sensitivity of rock permeability to the variations of Young's modulus and rock strength (cohesion and tensile strength) relative to Basecase 1. The results presented in the three figures suggested that thermally induced perturbation to the rock permeability is not sensitive to either rock-mass qualities for cases using rock-mass properties and variation of rock properties within the reasonable range for cases using intact-rock properties.

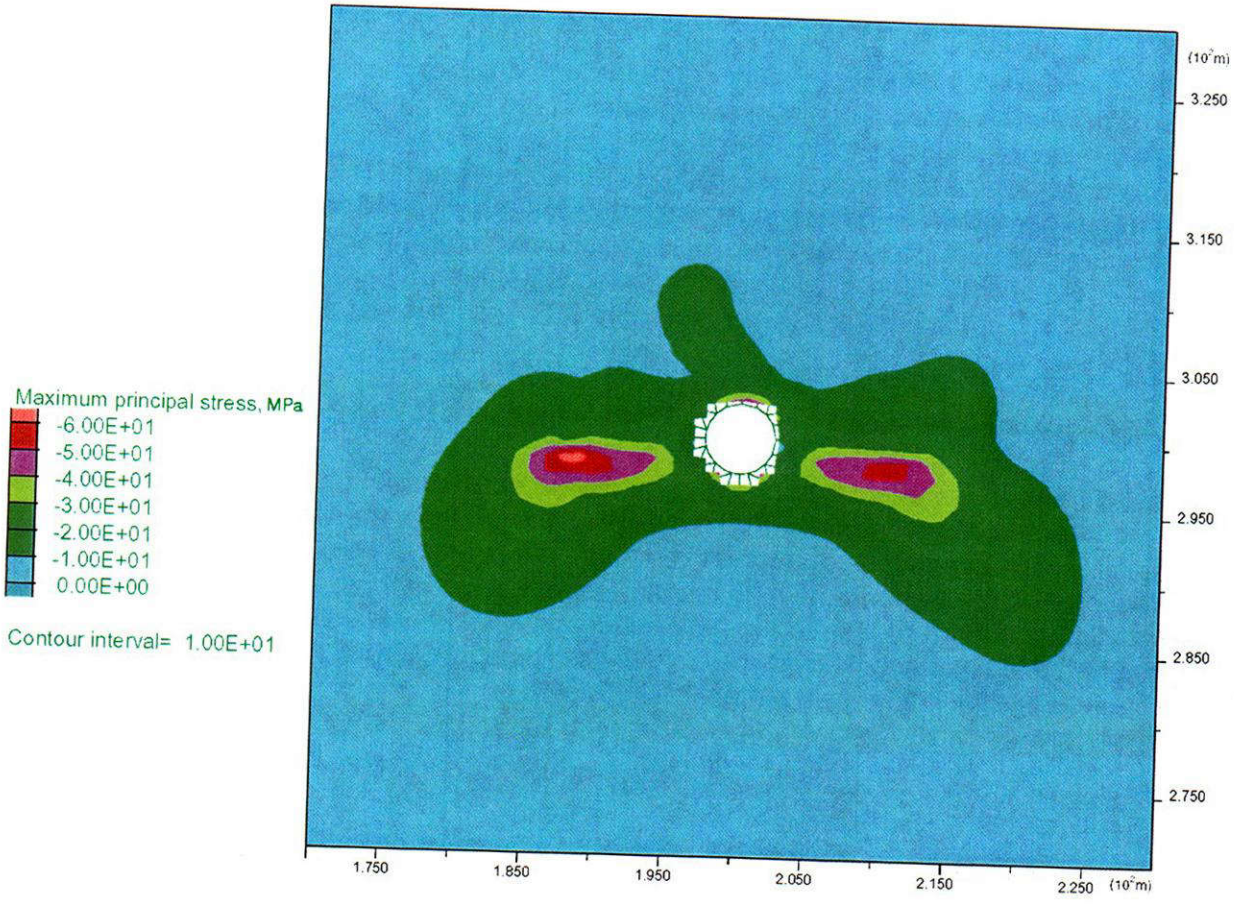

(a) After 3 Months of Heating

Figure 4-1. Maximum principal stress contour for Basecase 1 with Temperature Option 1

C04

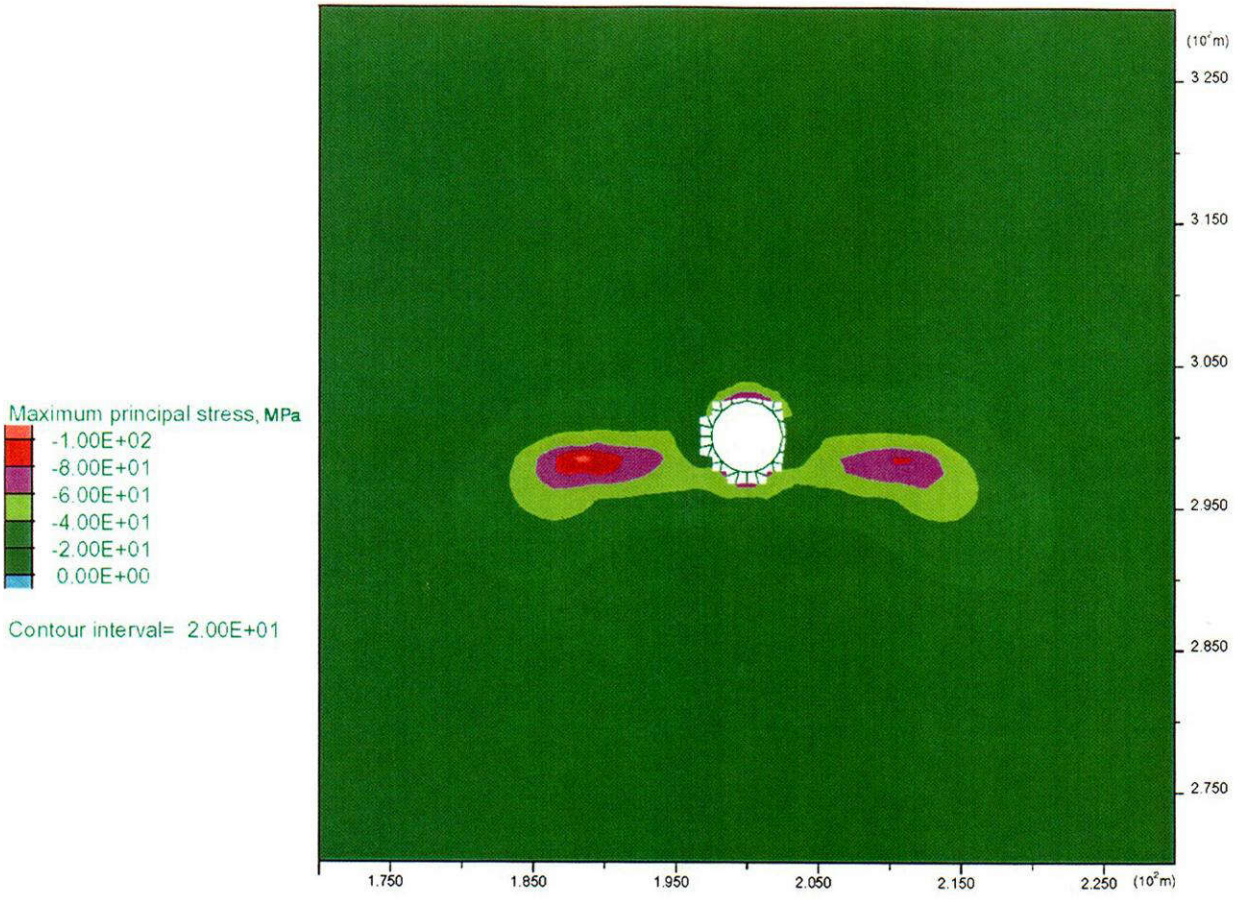

(b) After 1 Year of Heating

Figure 4-1. Maximum principal stress contour for Basecase 1 with Temperature Option 1 (cont'd)

C05

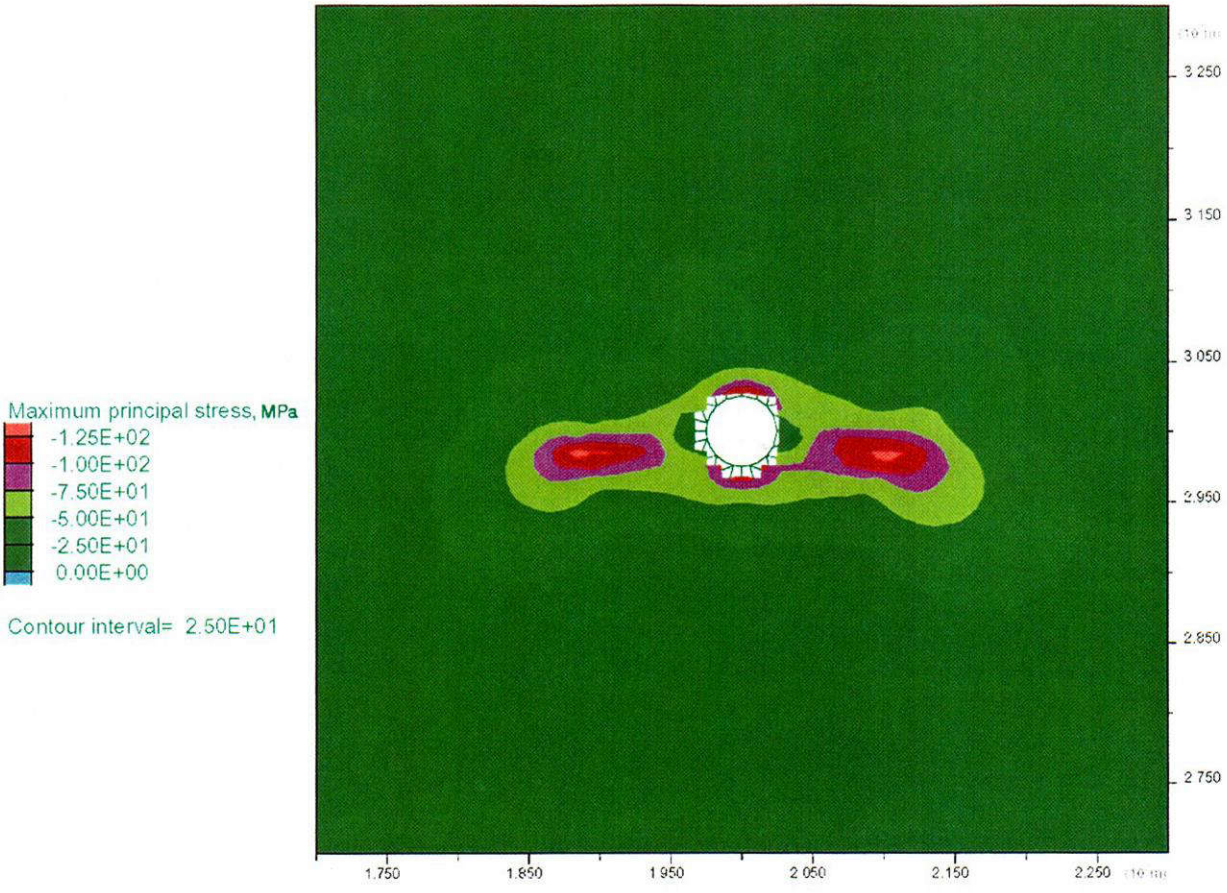

(c) After 4 Years of Heating

Figure 4-1. Maximum principal stress contour for Basecase 1 with Temperature Option 1 (cont'd)

C06

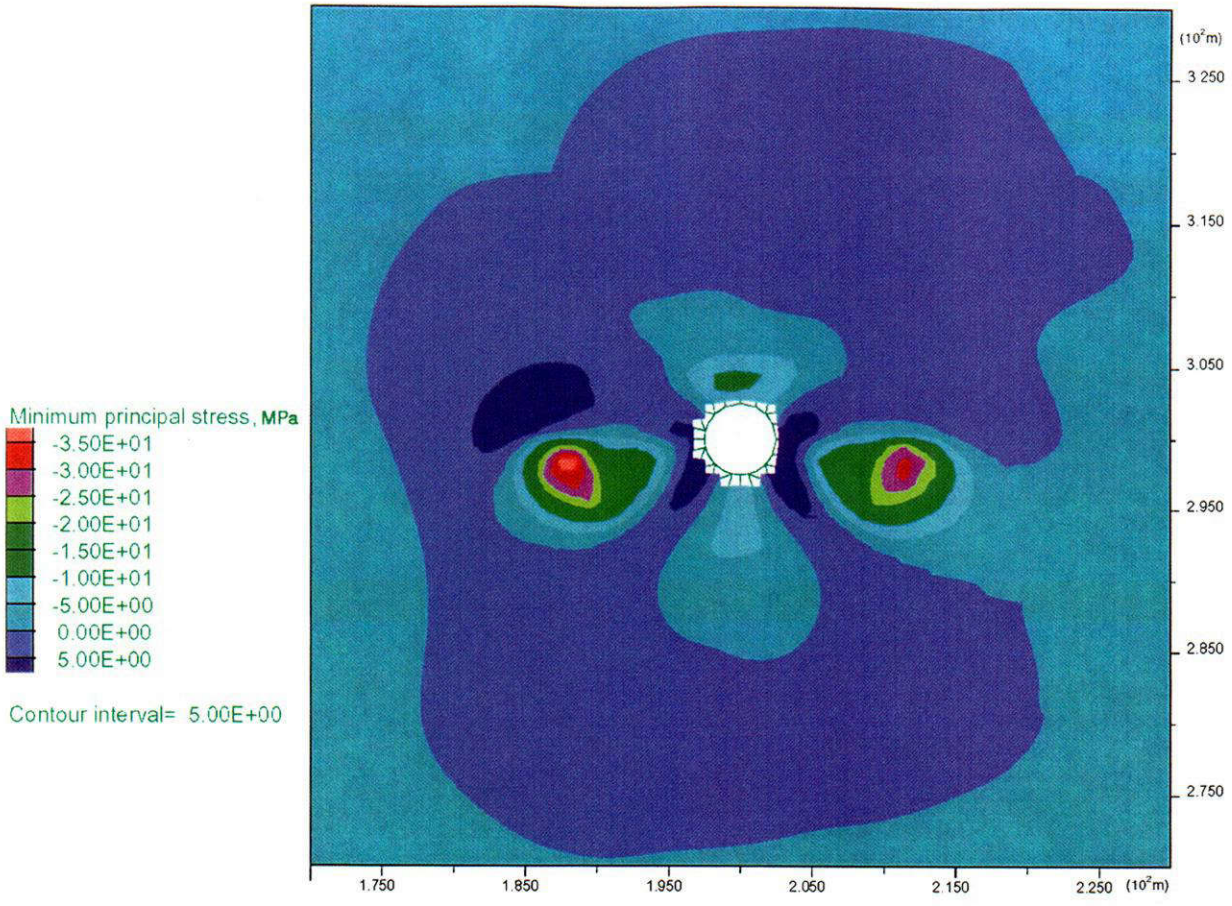

(a) After 3 Months of Heating

Figure 4-2. Minimum principal stress contour for Basecase 1 with Temperature Option 1

C07

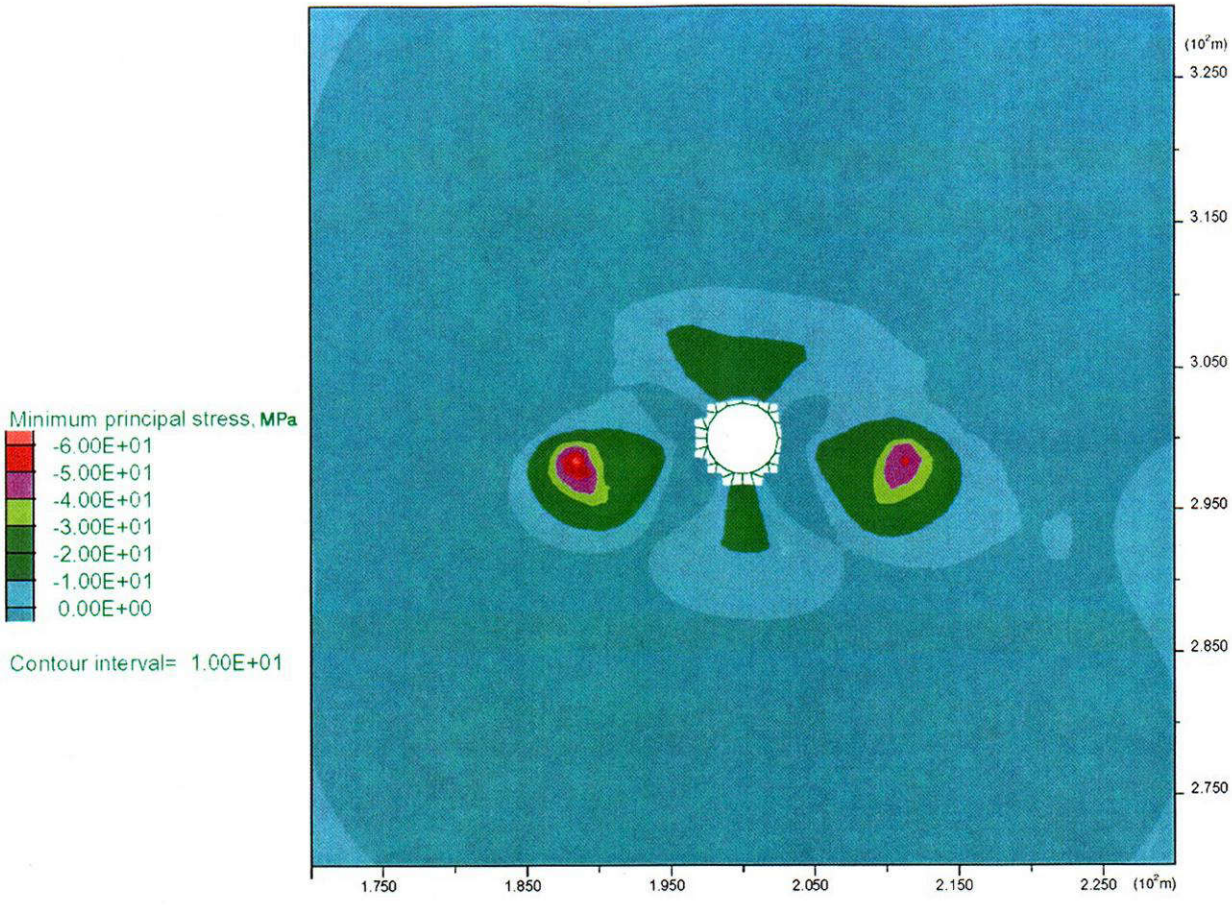

(b) After 1 Year of Heating

Figure 4-2. Minimum principal stress contour for Basecase 1 with Temperature Option 1 (cont'd)

C08

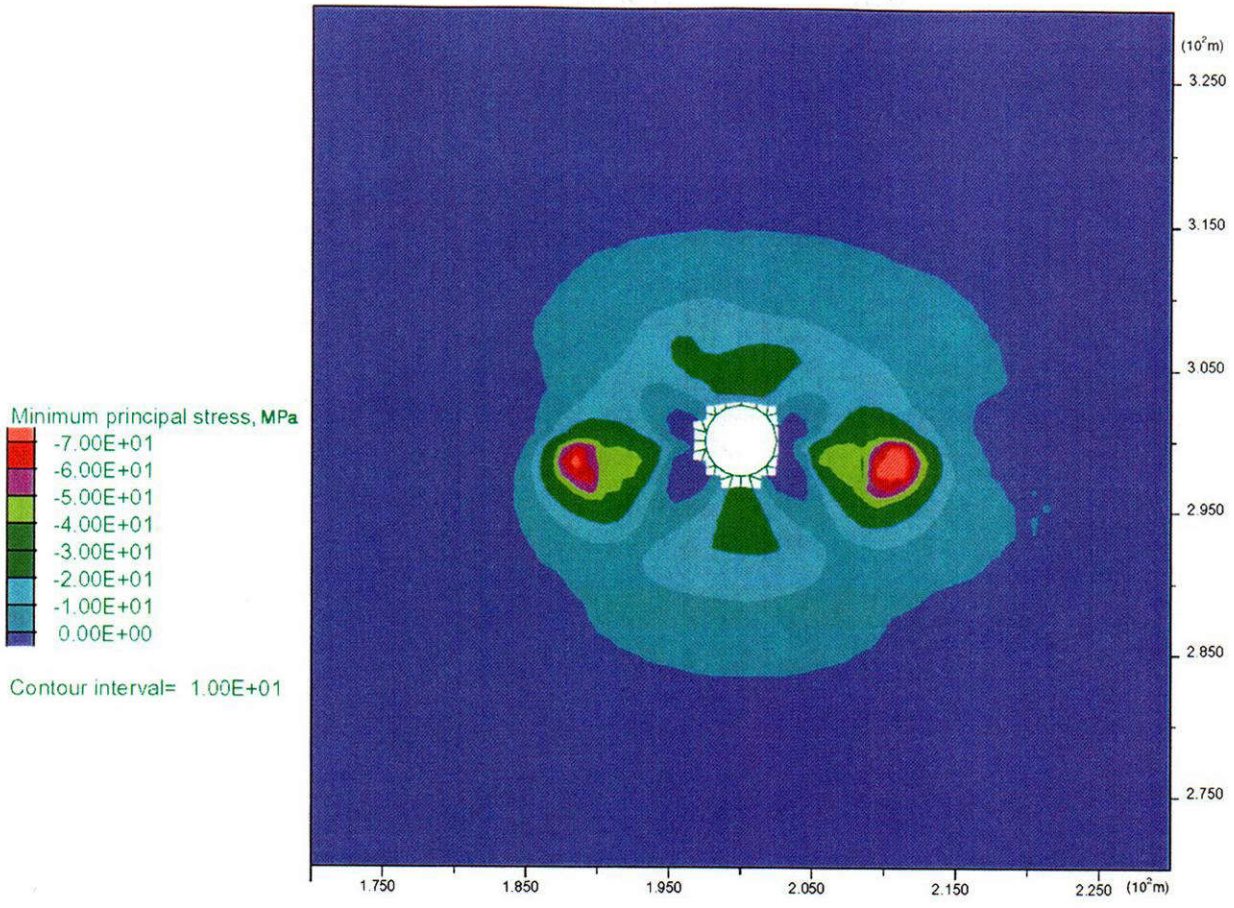

(c) After 4 Years of Heating

Figure 4-2. Minimum principal stress contour for Basecase 1 with Temperature Option 1 (cont'd)

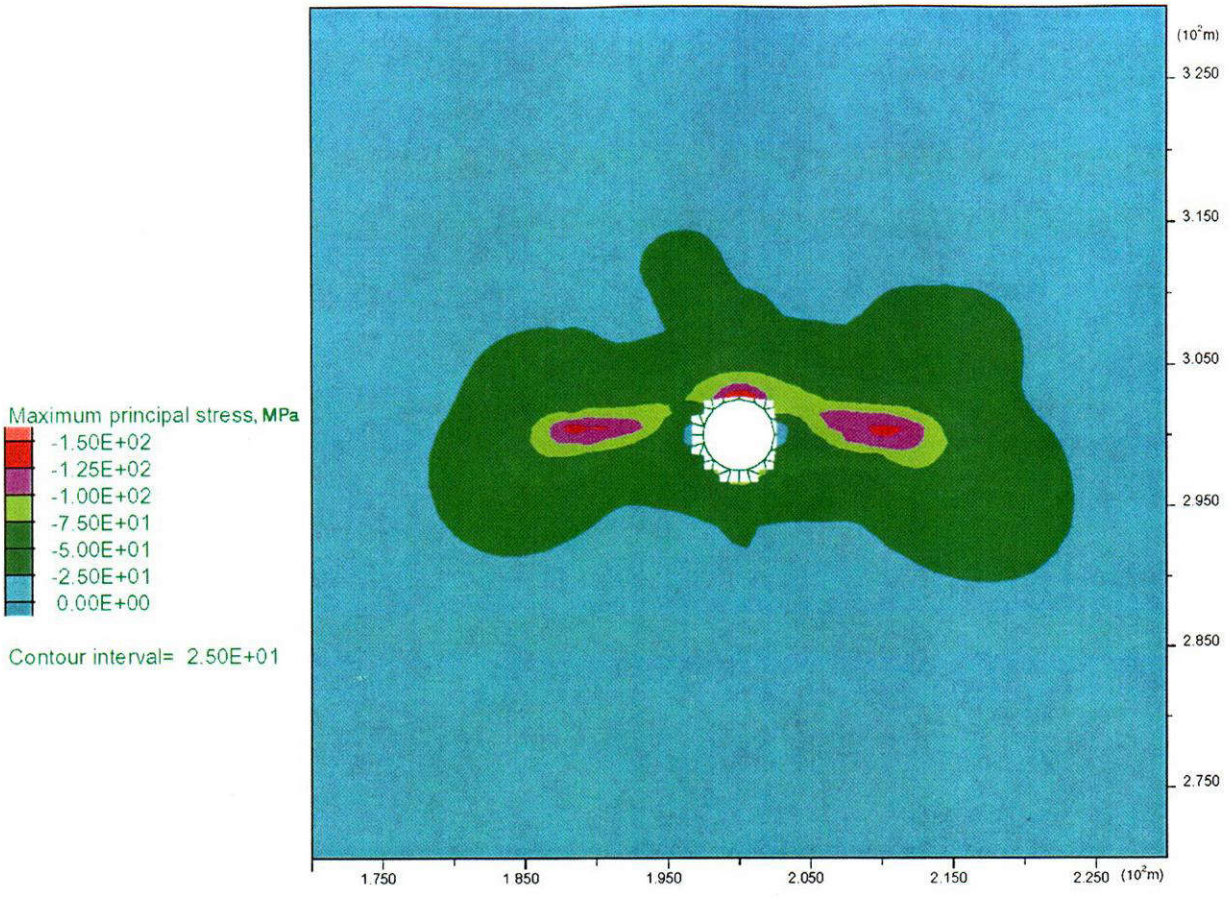

(a) Maximum Principal Stress

Figure 4-3. Contours of principal stresses contour for Basecase 1 with Temperature Option 2 after 4 years of heating

C10

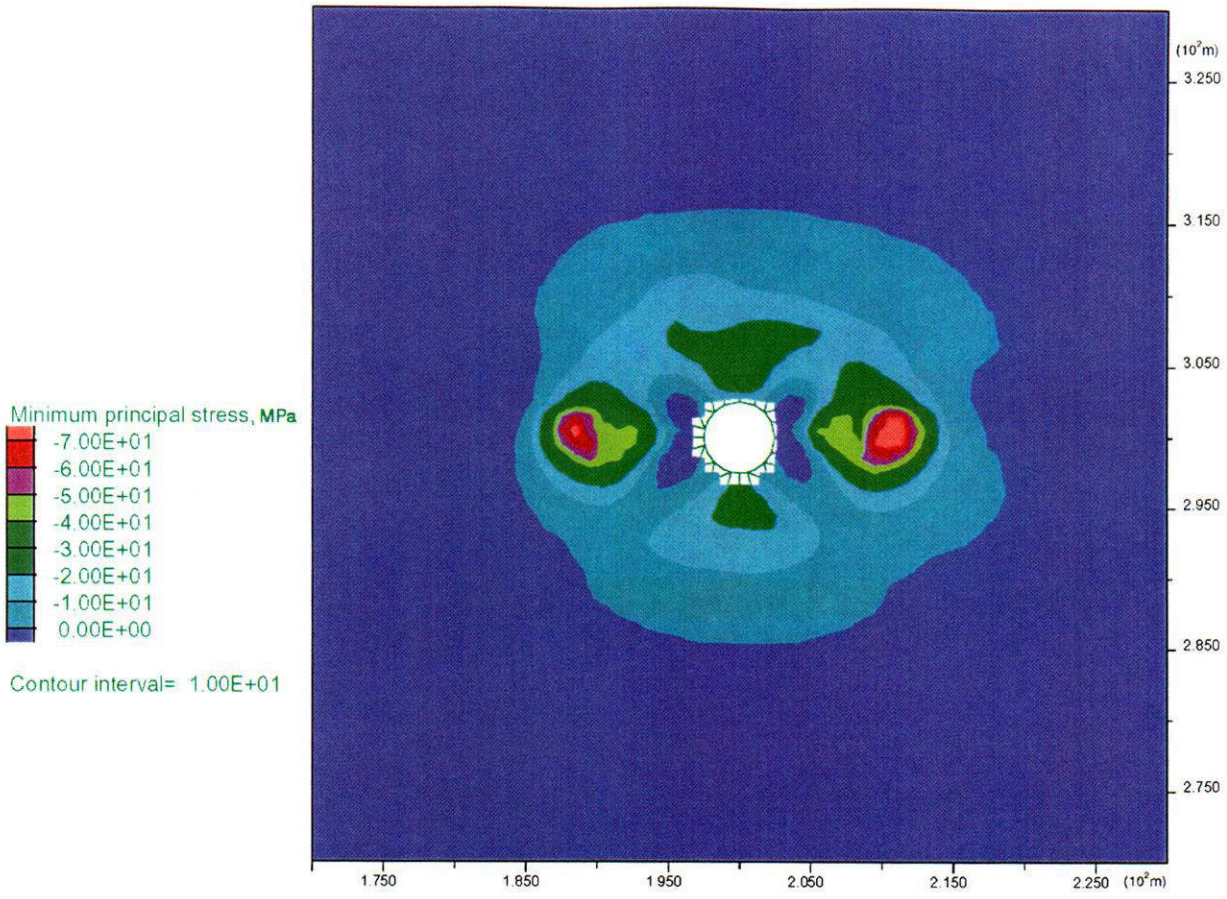

(b) Minimum Principal Stress

Figure 4-3. Contours of principal stresses contour for Basecase 1 with Temperature Option 2 after 4 years of heating (cont'd)

C11

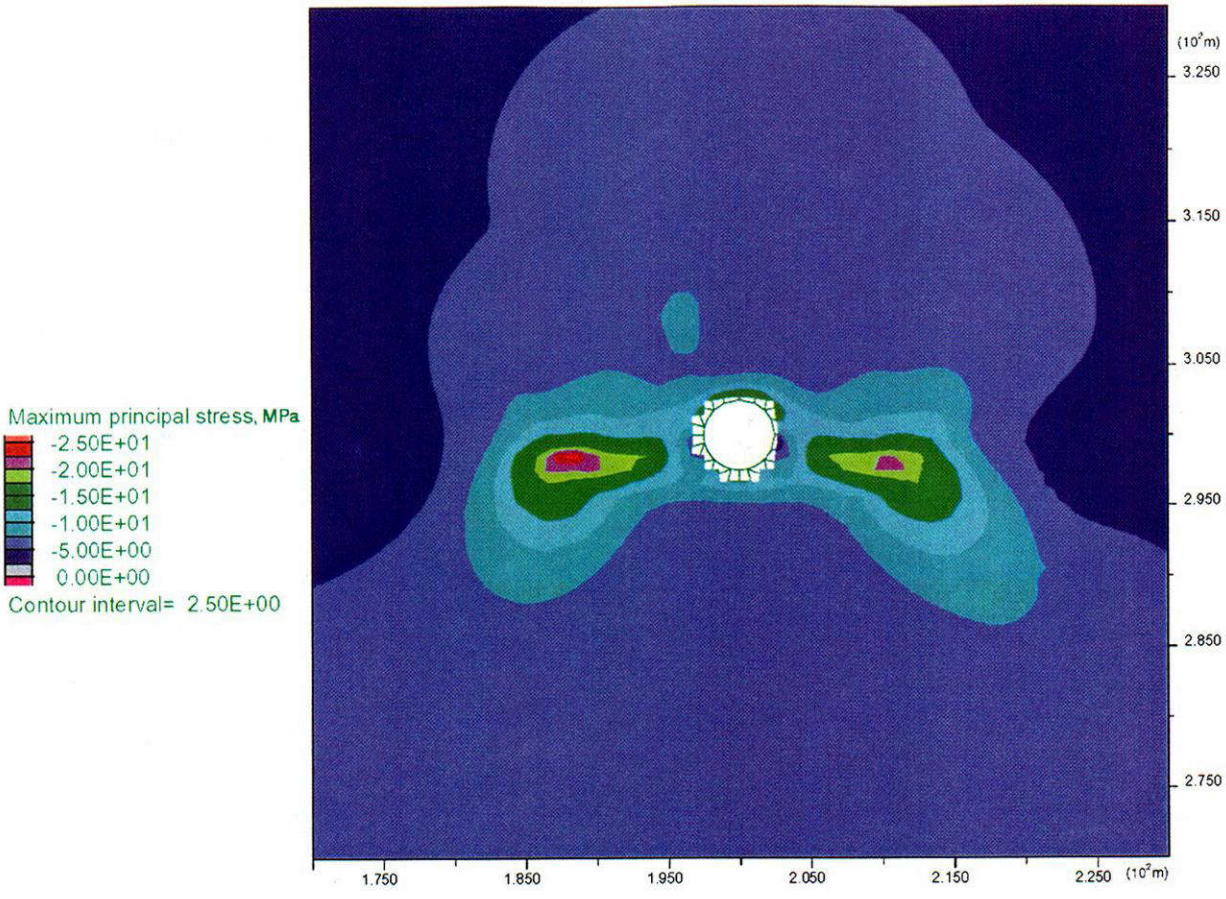

(a) After 3 Months of Heating

Figure 4-4. Maximum principal stress contour for Basecase 2 with Temperature Option 1

C12

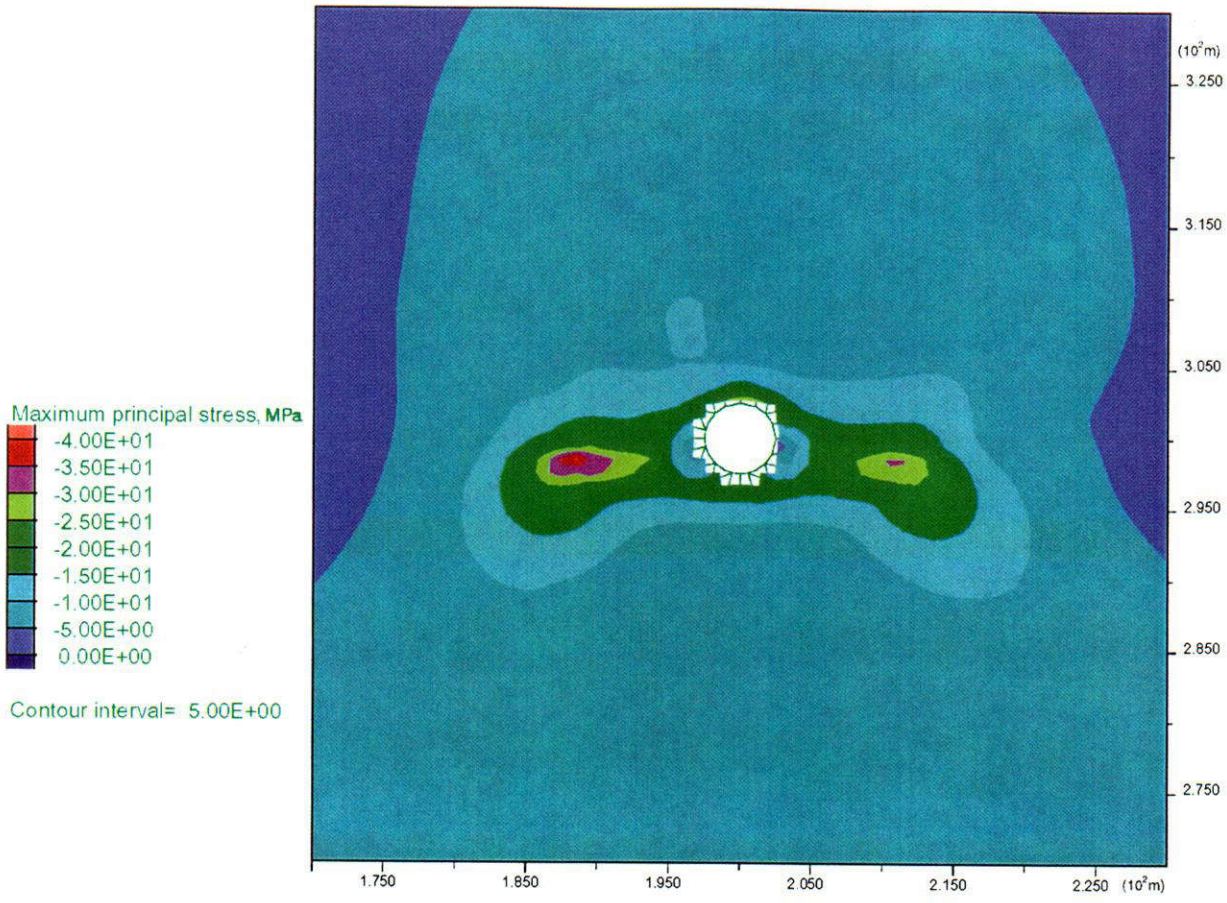

(b) After 1 Year of Heating

Figure 4-4. Maximum principal stress contour for Basecase 2 with Temperature Option 1 (cont'd)

C13

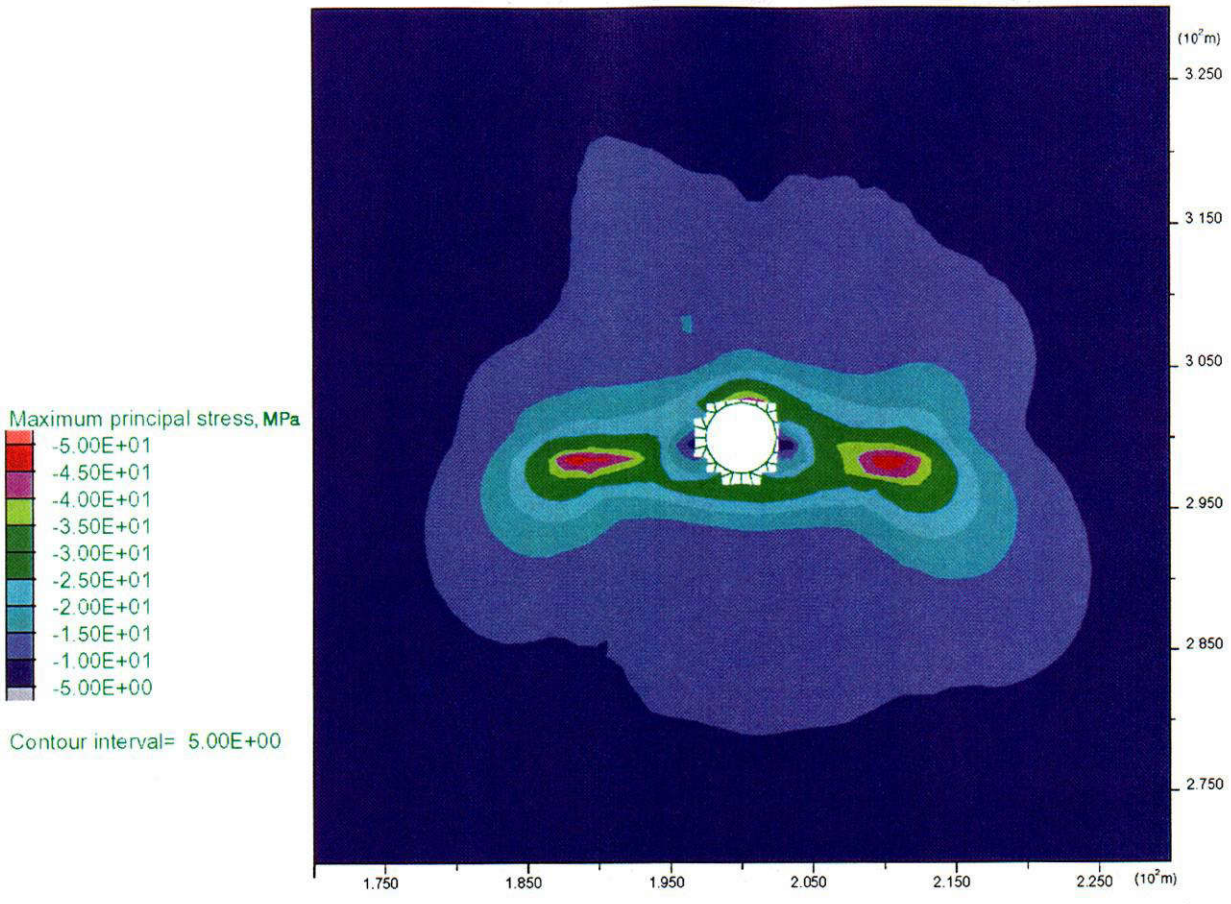

(c) After 4 Years of Heating

Figure 4-4. Maximum principal stress contour for Basecase 2 with Temperature Option 1 (cont'd)

C14

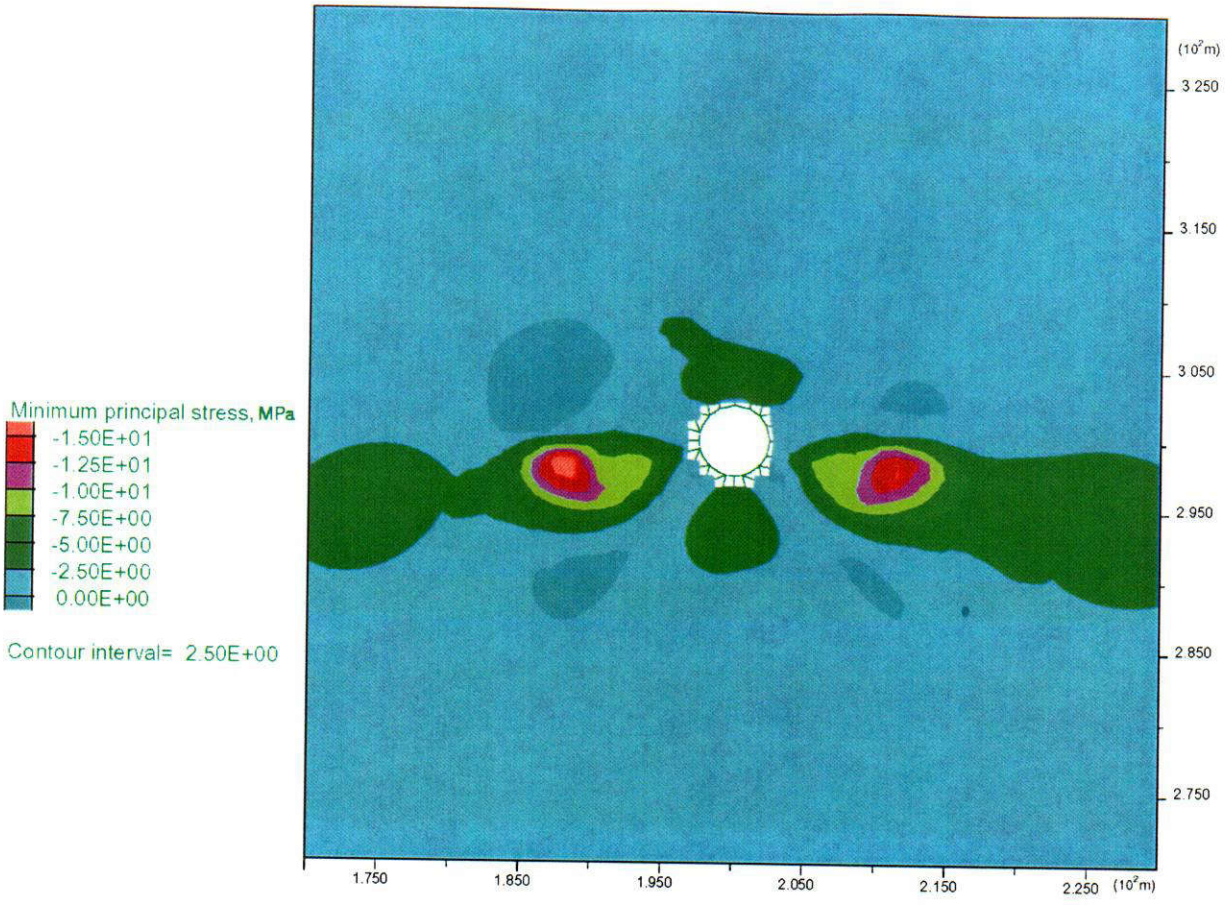

(a) After 3 Months of Heating

Figure 4-5. Minimum principal stress contour for Basecase 2 with Temperature Option 1

C15

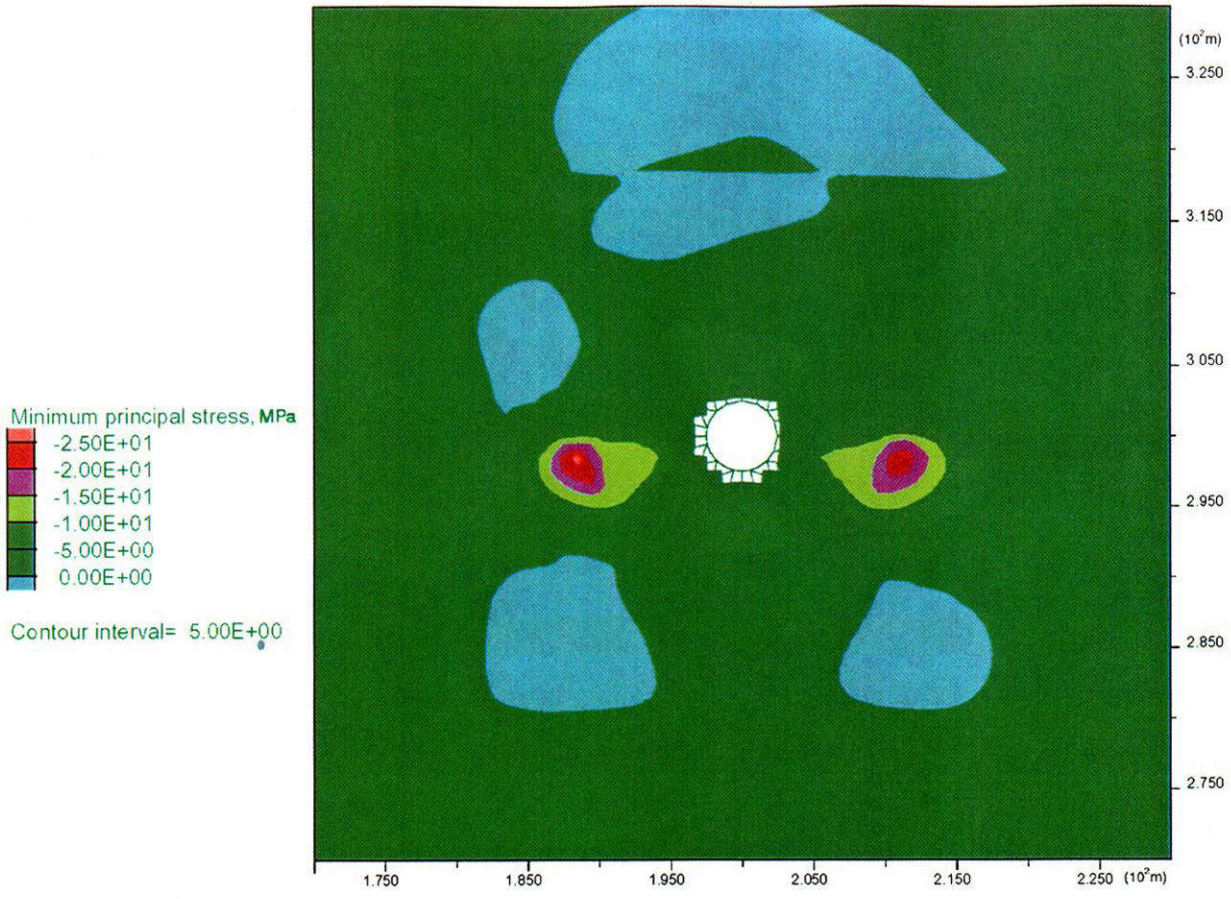

(b) After 1 Year of Heating

Figure 4-5. Minimum principal stress contour for Basecase 2 with Temperature Option 1 (cont'd)

C16

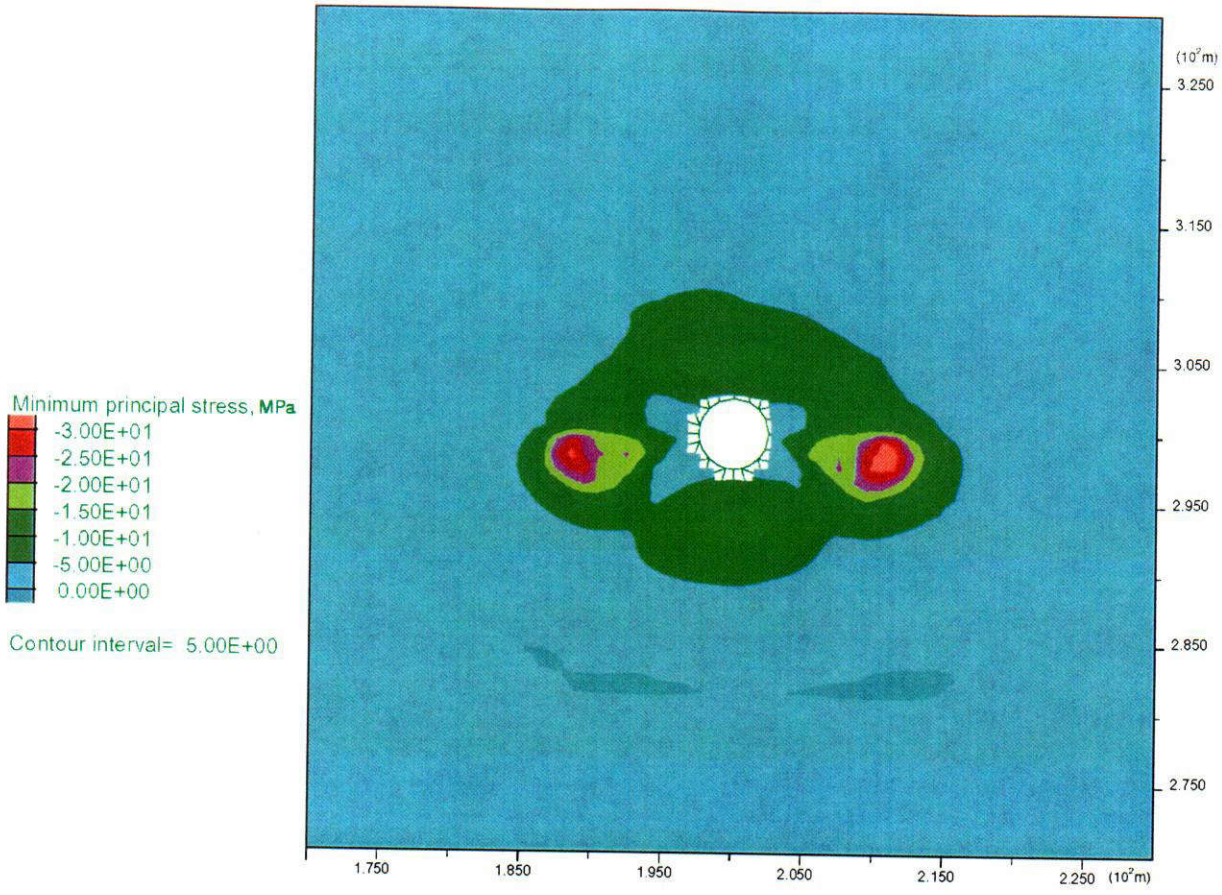

(c) After 4 Years of Heating

Figure 4-5. Minimum principal stress contour for Basecase 2 with Temperature Option 1 (cont'd)

C17

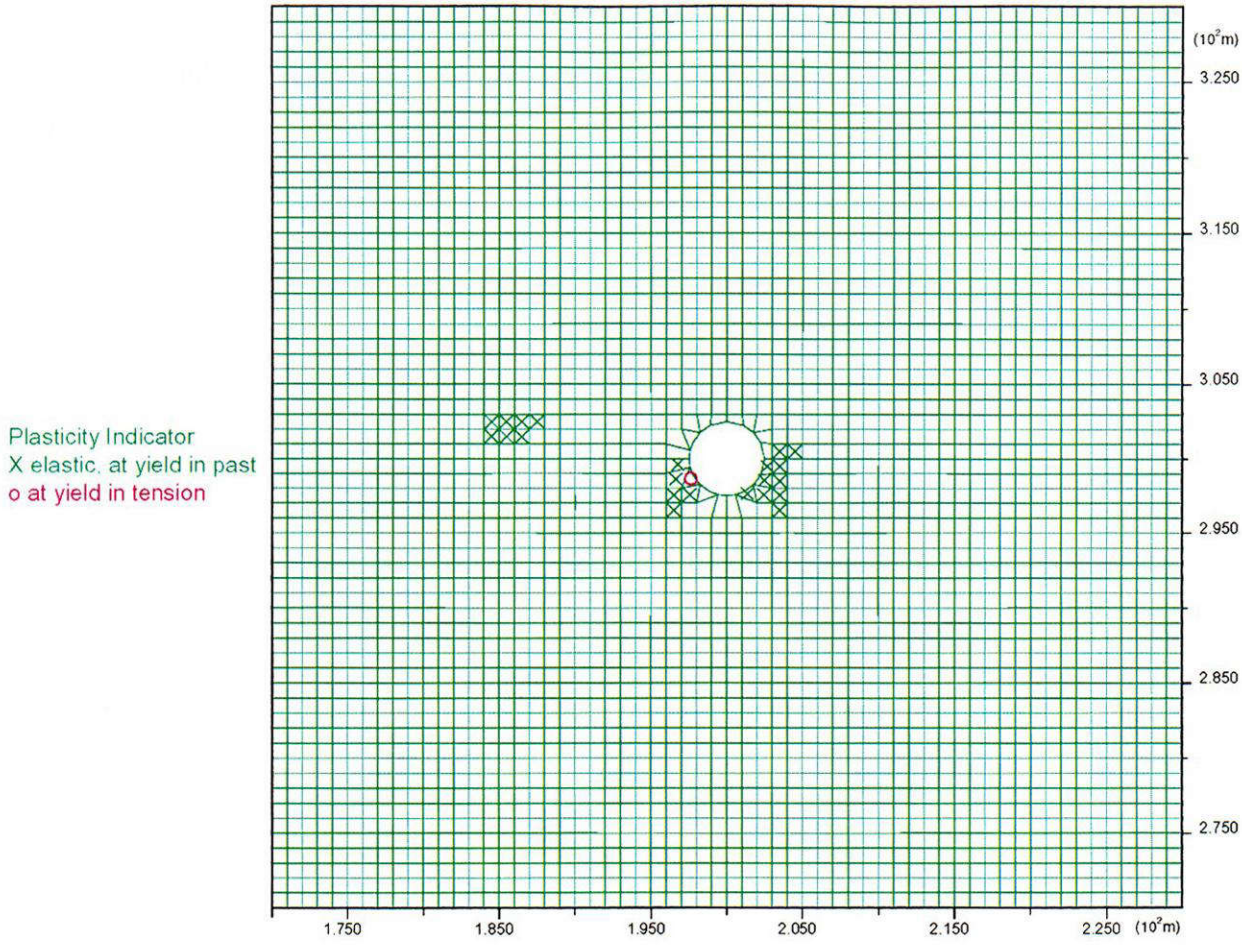

(a) After 3 Months of Heating

Figure 4-6. Extent of yielding in rock as a function of time for Basecase 1 with Temperature Option 1

C18

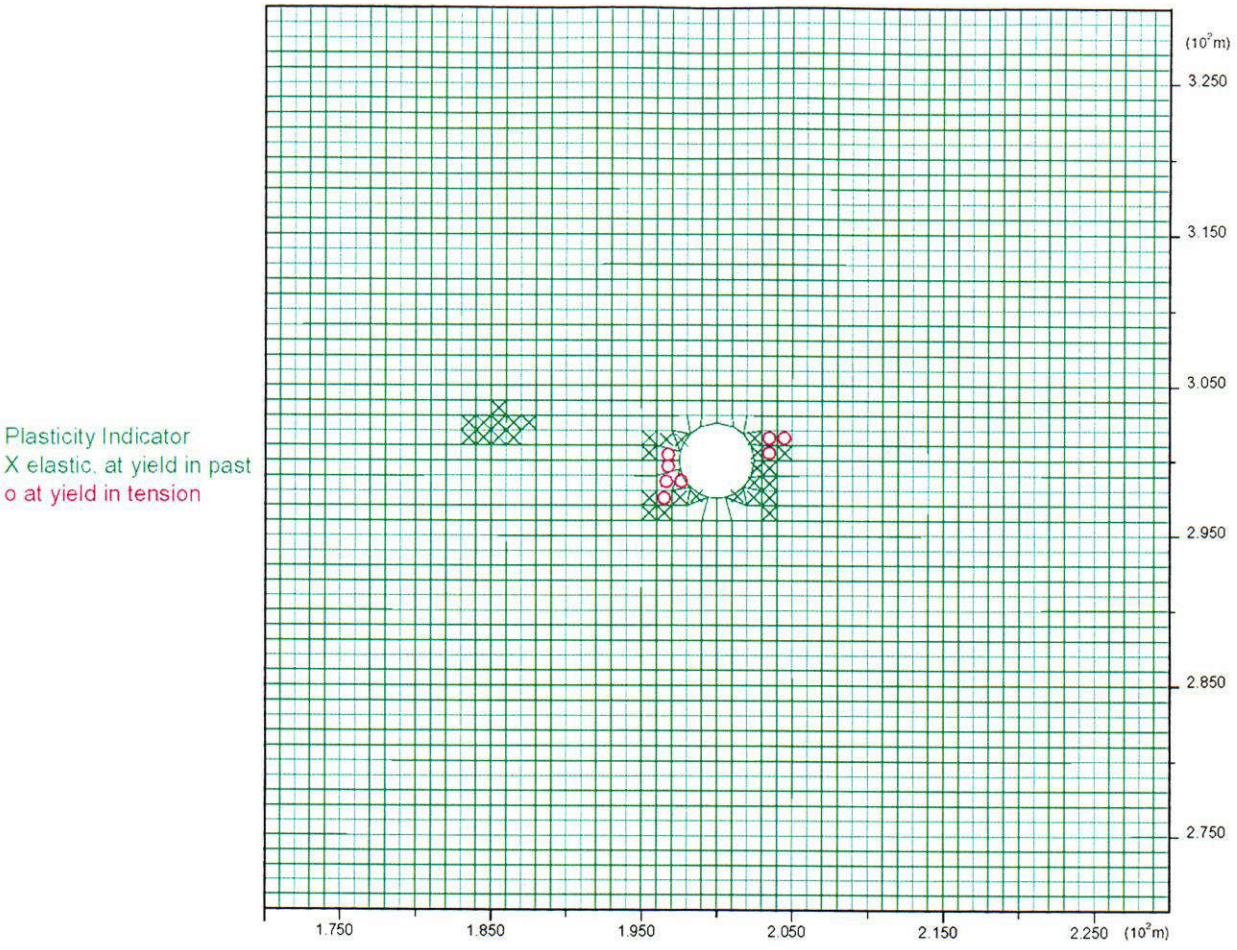

(b) After 1 Year of Heating

Figure 4-6. Extent of yielding in rock as a function of time for Basecase 1 with Temperature Option 1 (cont'd)

C19

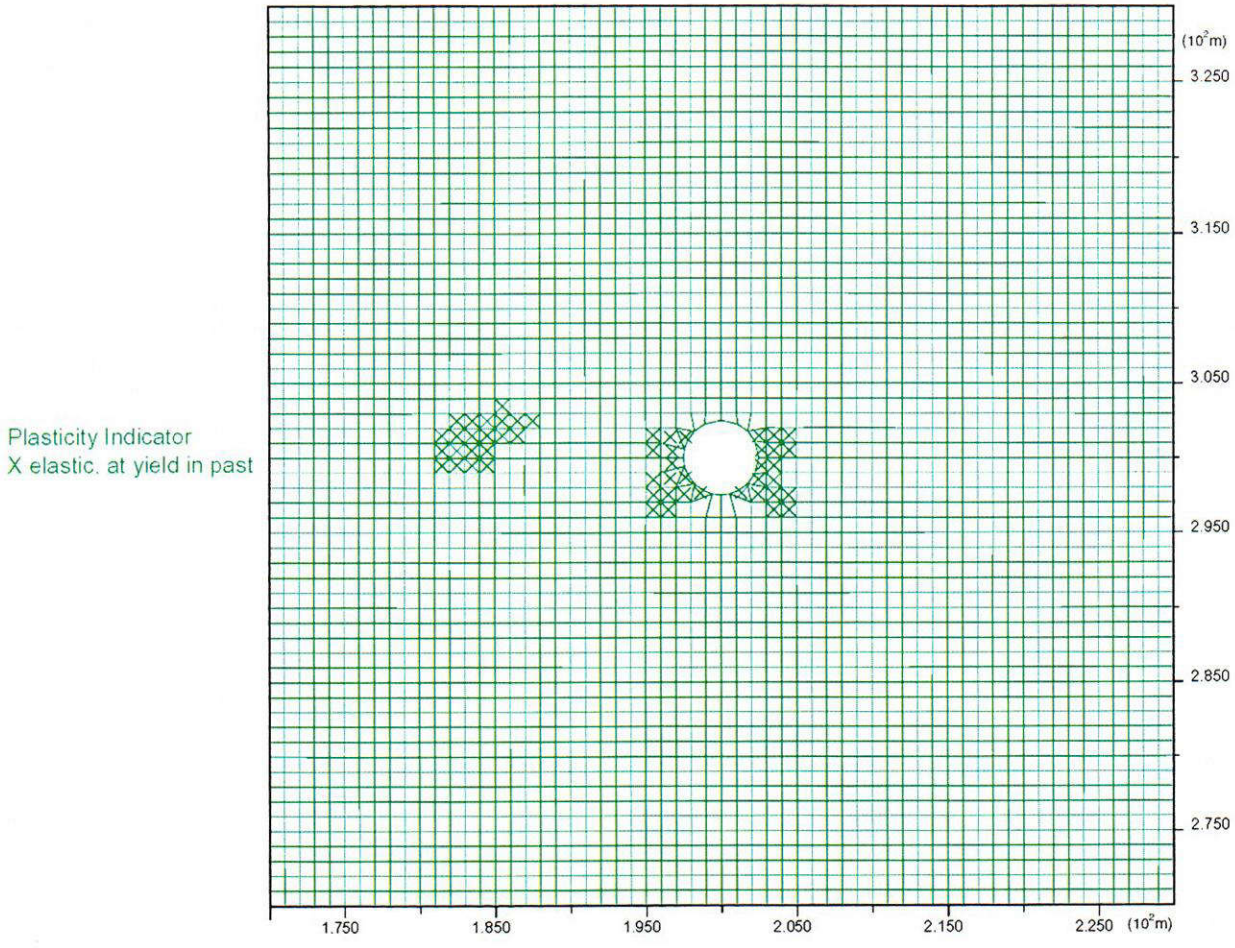

(c) After 4 Years of Heating

Figure 4-6. Extent of yielding in rock as a function of time for Basecase 1 with Temperature Option 1 (cont'd)

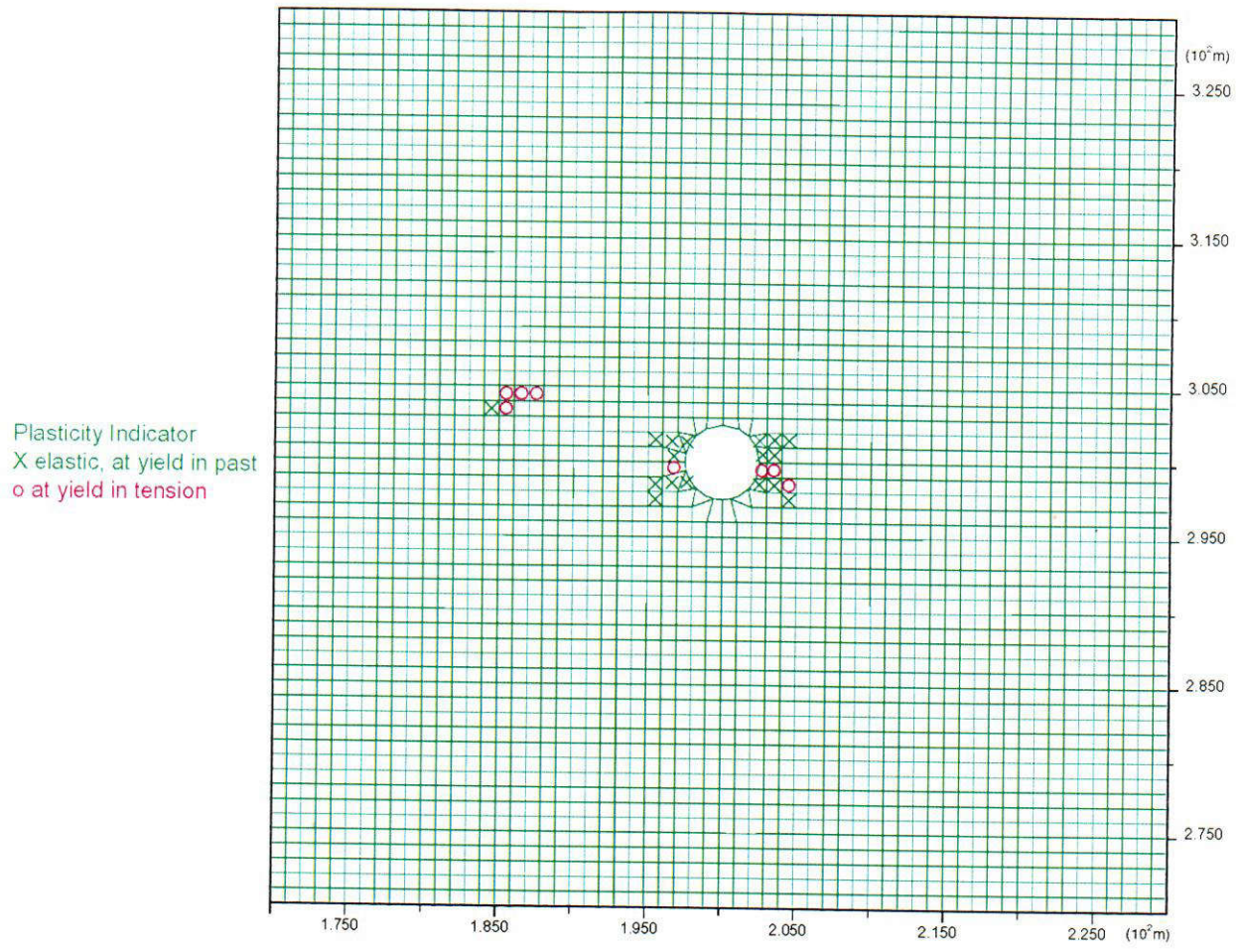

(a) After 3 Months of Heating

Figure 4-7. Extent of yielding in rock as a function of time for Basecase 1 with Temperature Option 2

C20

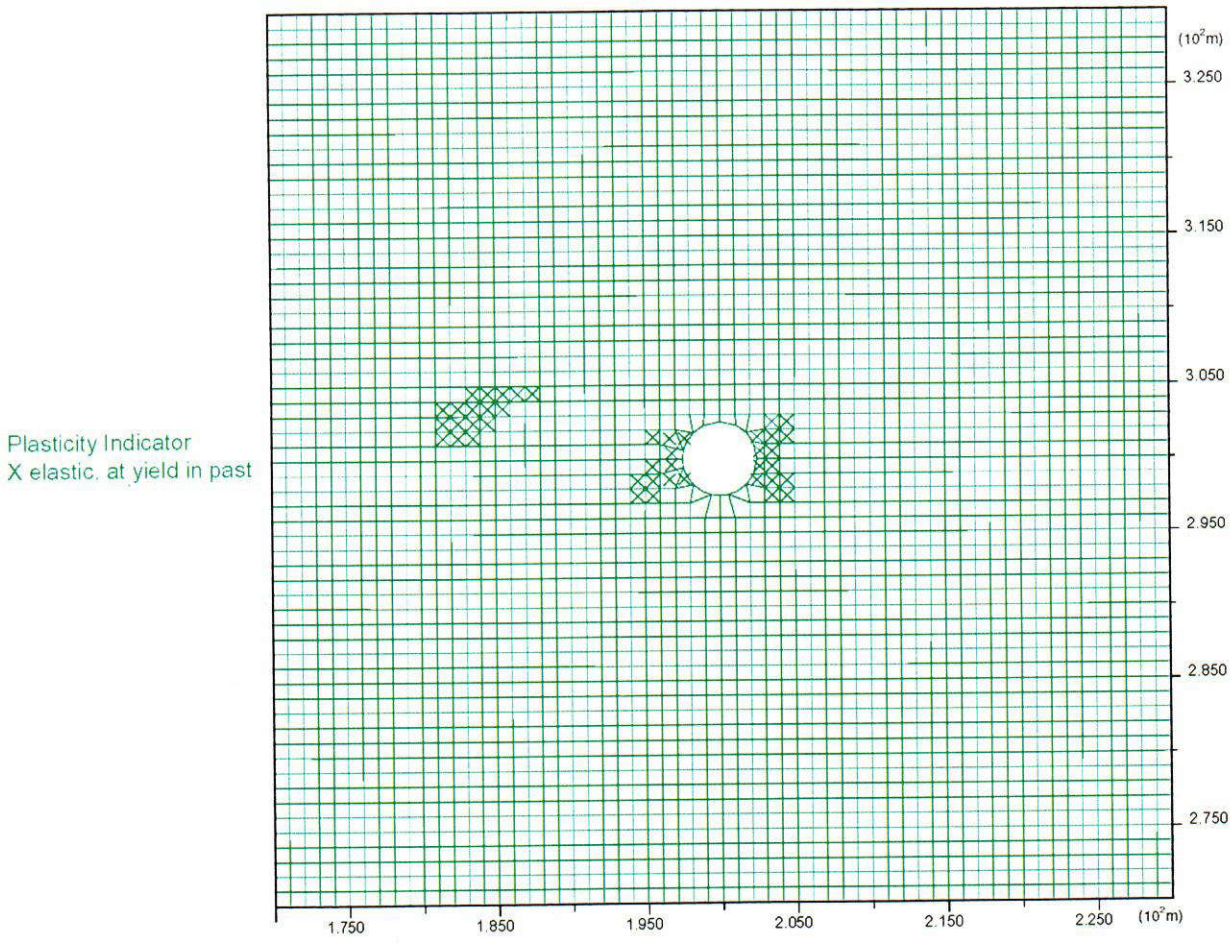

(b) After 4 Years of Heating

Figure 4-7. Extent of yielding in rock as a function of time for Basecase 1 with Temperature Option 2 (cont'd)

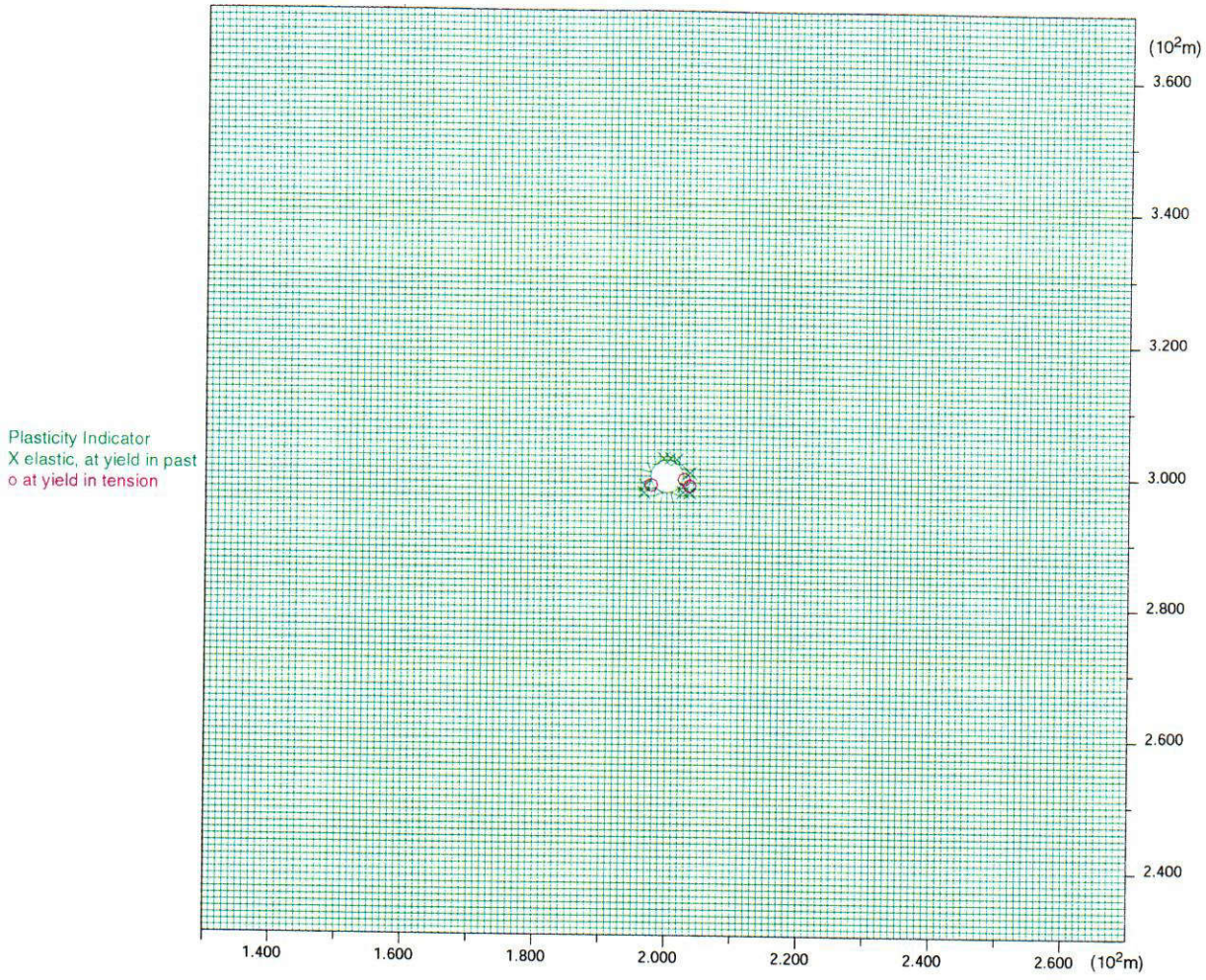

(a) After 3 Months of Heating

Figure 4-8. Extent of yielding in rock as a function of time for Sensitivity Case 1 with Temperature Option 1

C21

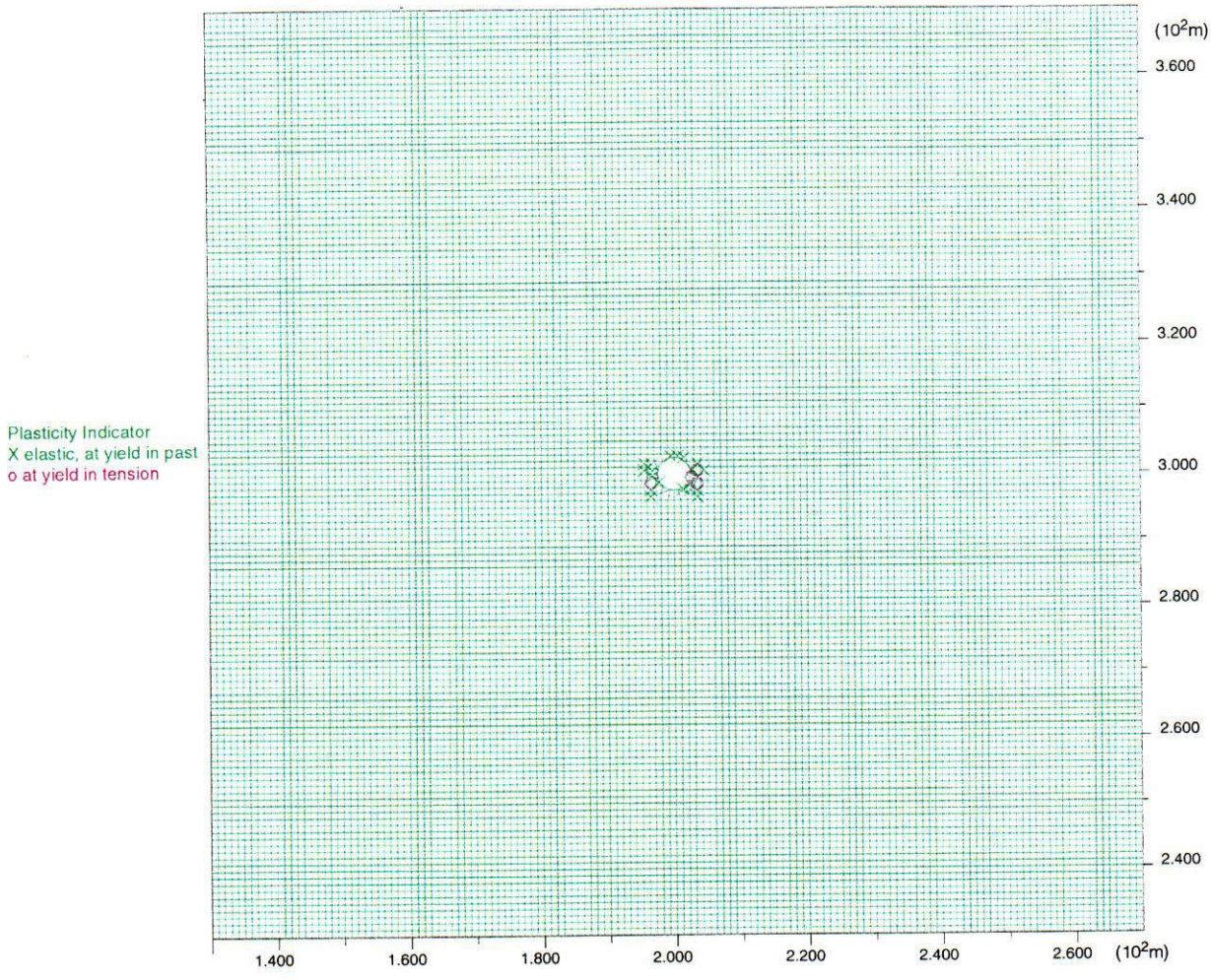

(b) After 1 Year of Heating

Figure 4-8. Extent of yielding in rock as a function of time for Sensitivity Case 1 with Temperature Option 1 (cont'd)

C22

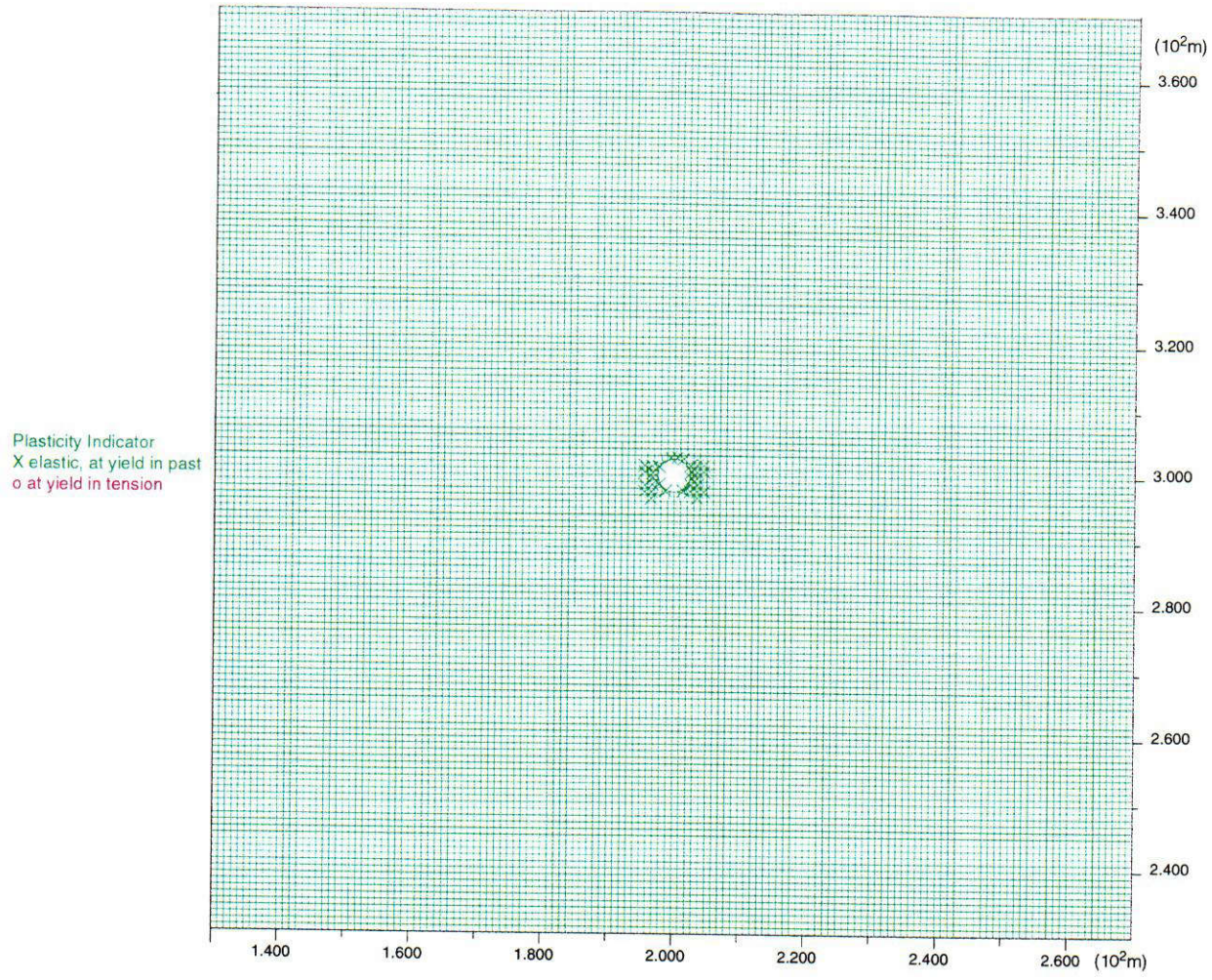

(c) After 4 Years of Heating

Figure 4-8. Extent of yielding in rock as a function of time for Sensitivity Case 1 with Temperature Option 1 (cont'd)

C23

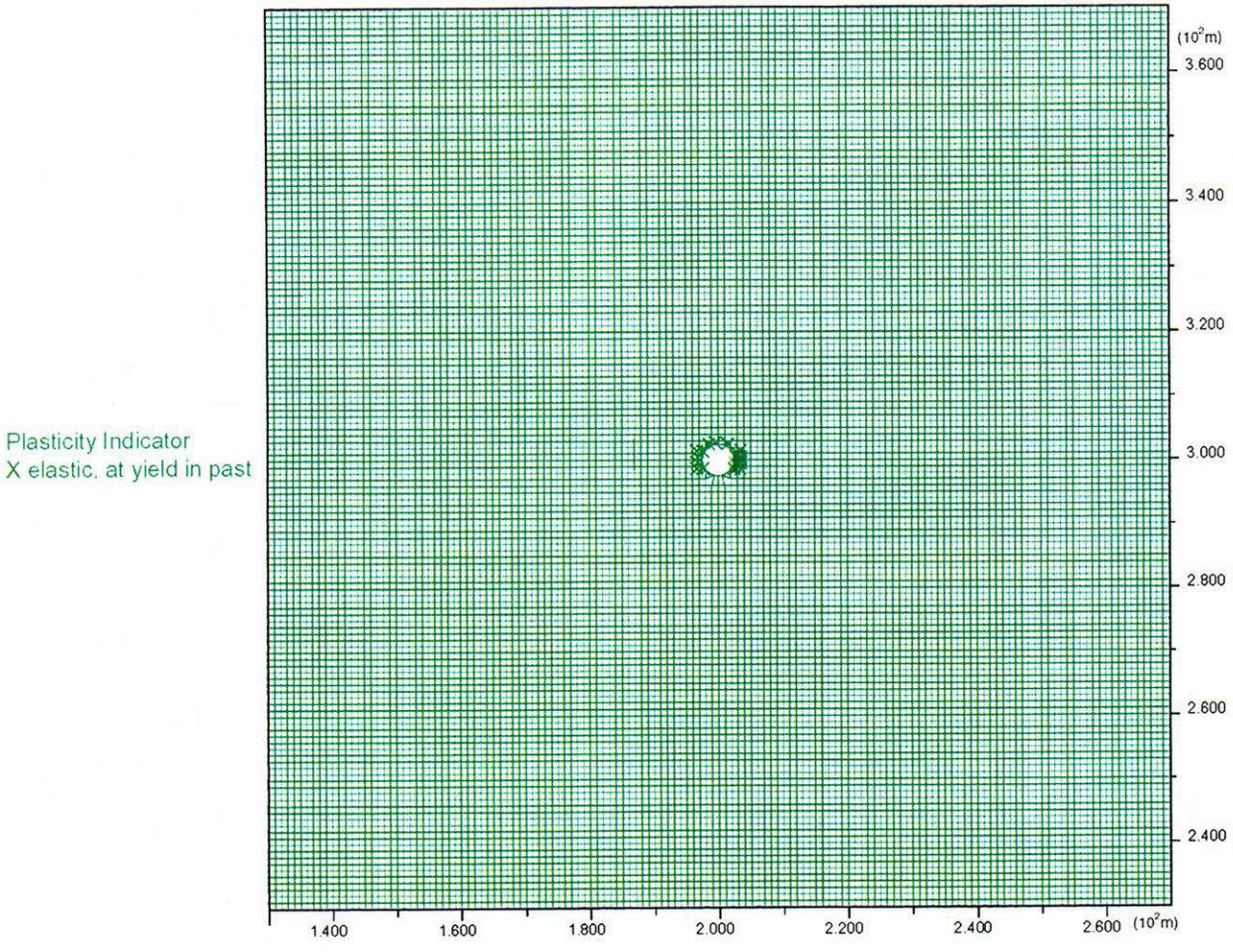

(a) After 3 Months of Heating

Figure 4-9. Extent of yielding in rock as a function of time for Sensitivity Case 1 with Temperature Option 2

C24

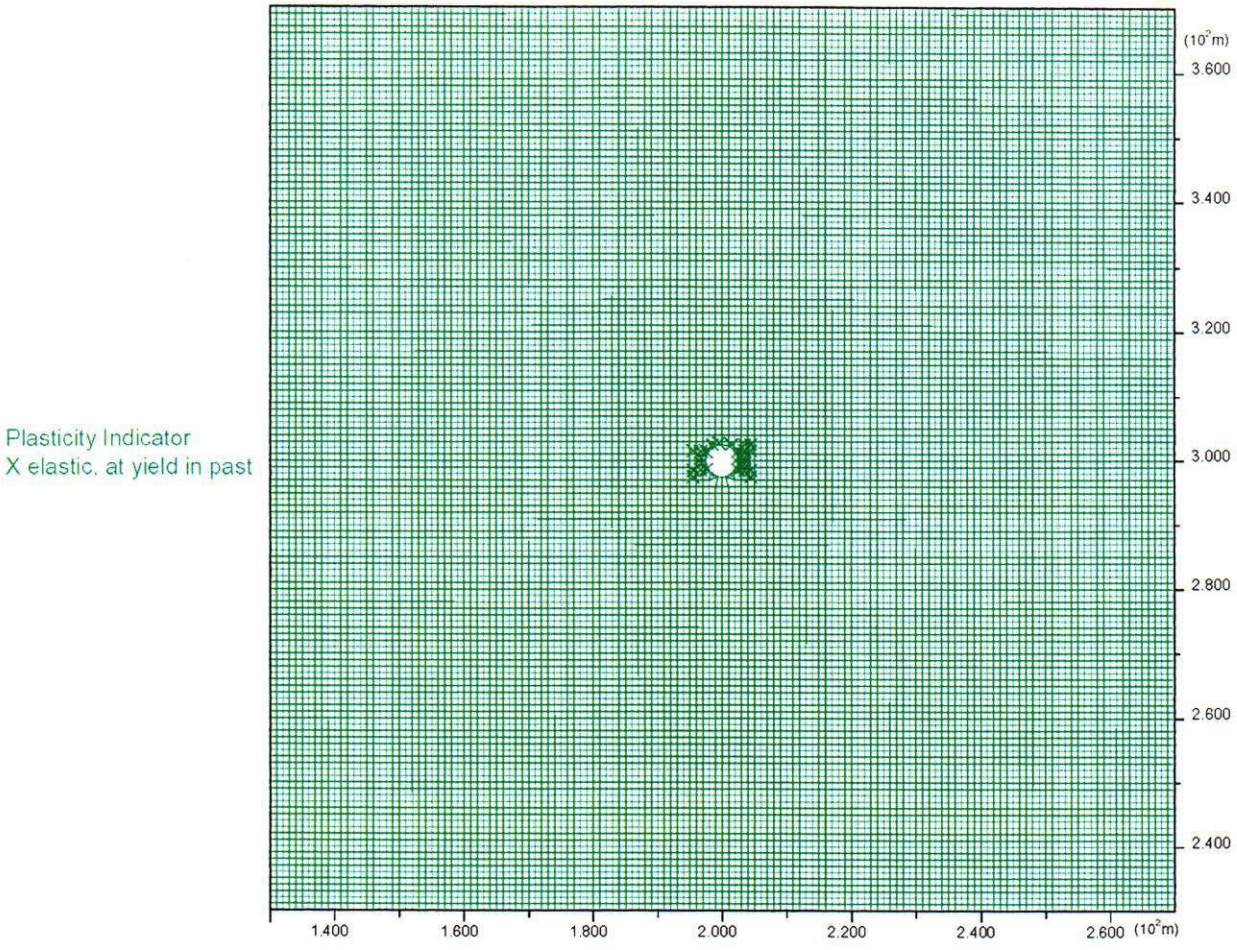

(b) After 4 Years of Heating

Figure 4-9. Extent of yielding in rock as a function of time for Sensitivity Case 1 with Temperature Option 2

C25

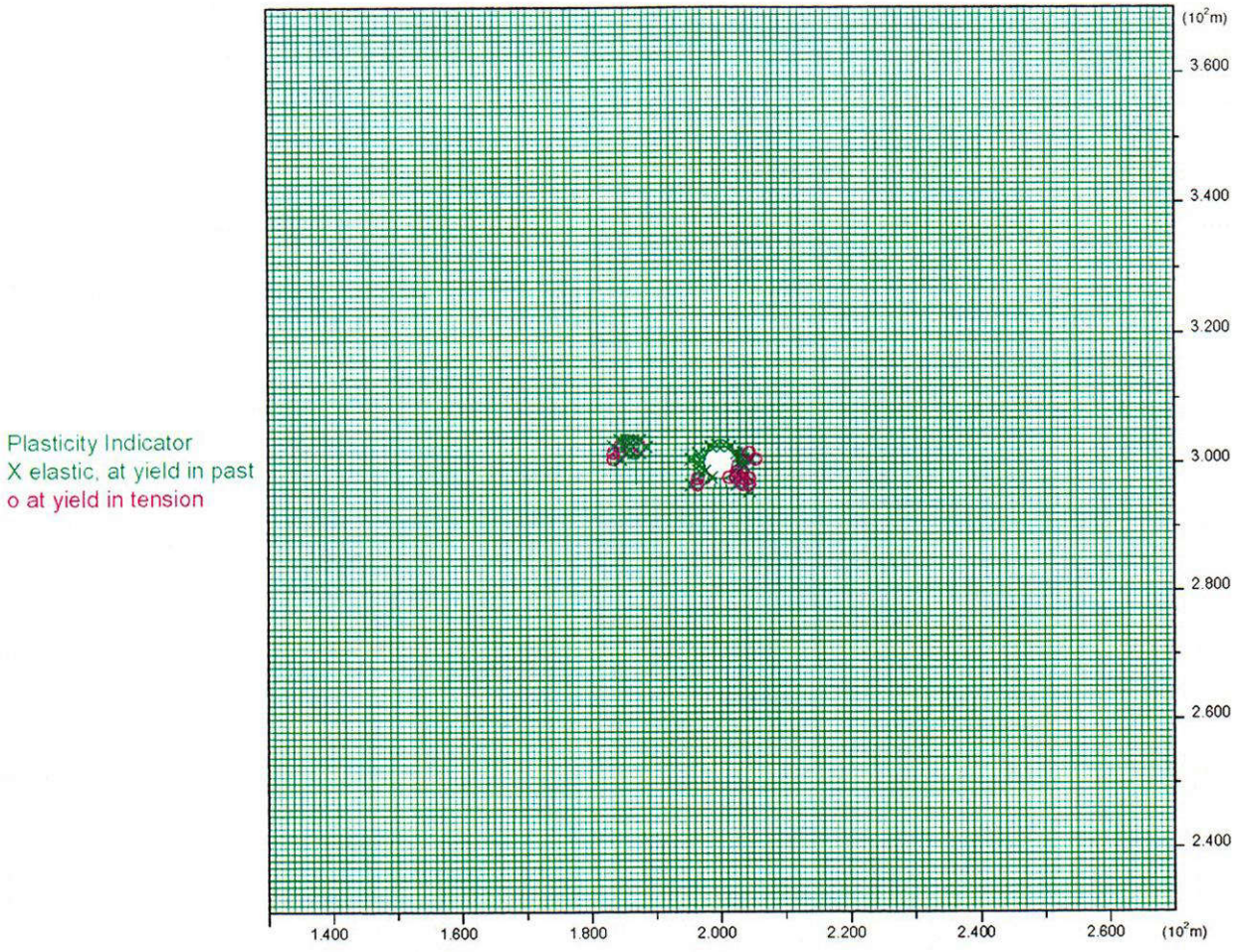

(a) After 3 Months of Heating

Figure 4-10. Extent of yielding in rock as a function of time for Sensitivity Case 2 with Temperature Option 1

C26

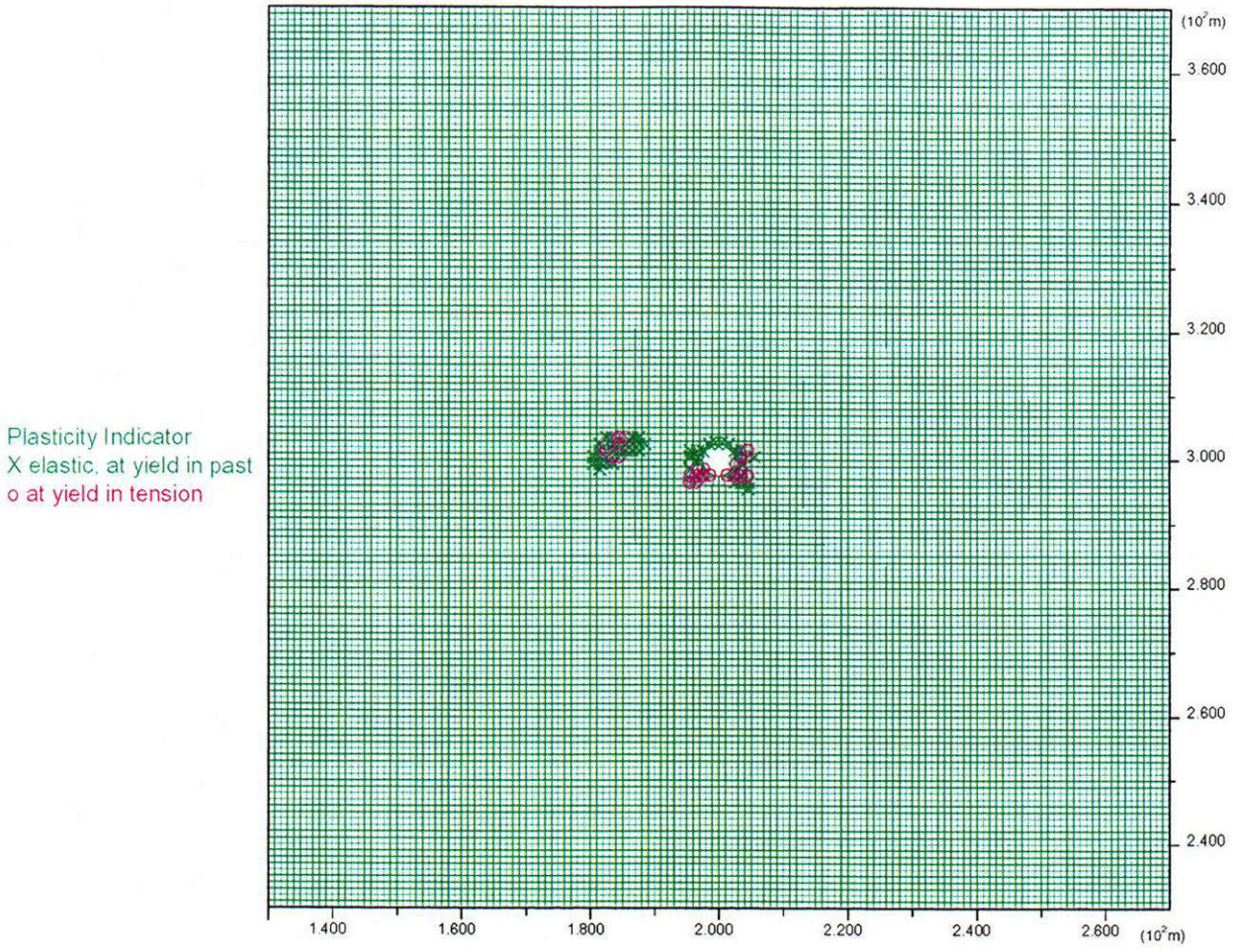

(b) After 1 Year of Heating

Figure 4-10. Extent of yielding in rock as a function of time for Sensitivity Case 2 with Temperature Option 1 (cont'd)

CZ7

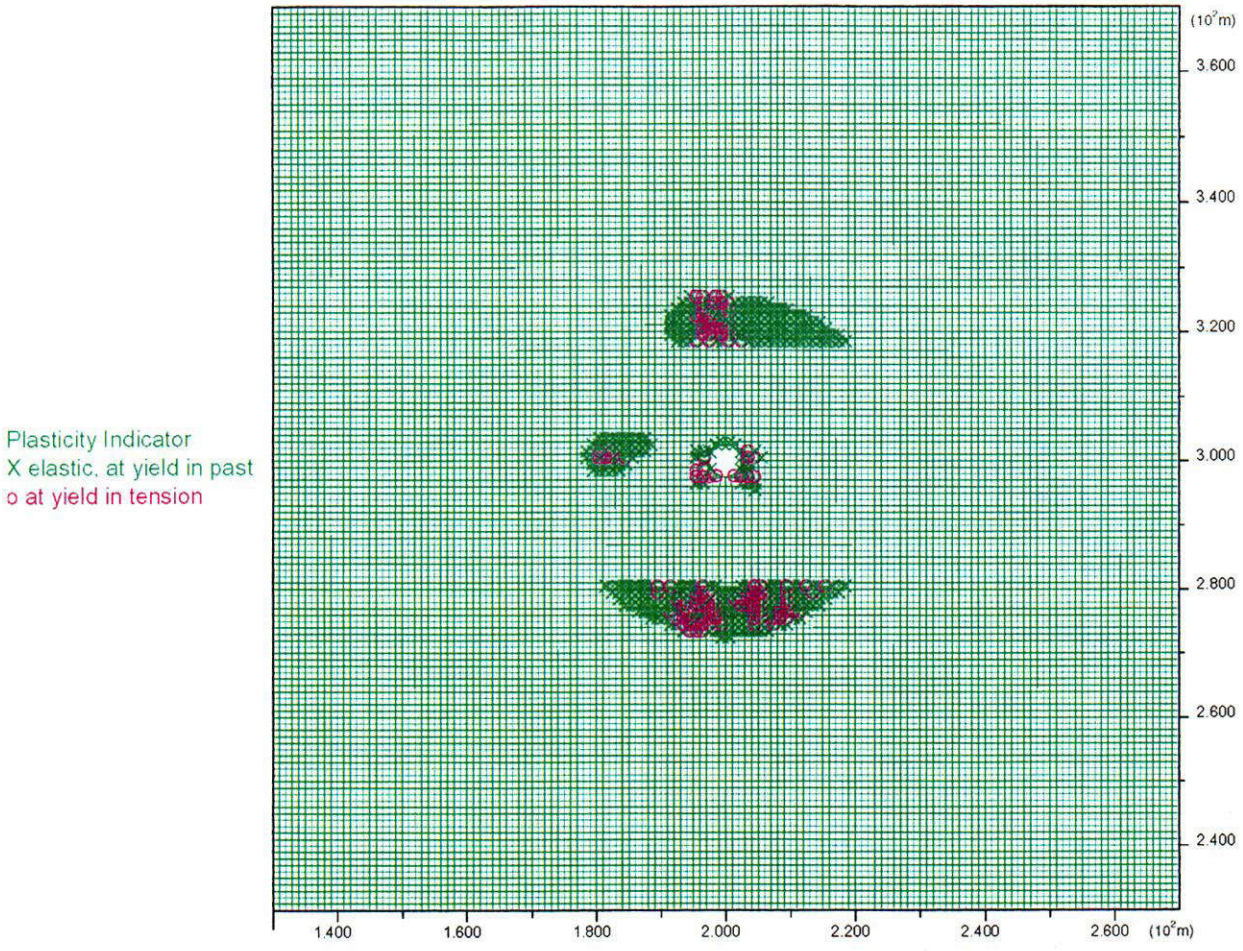

(c) After 2 Years of Heating

Figure 4-10. Extent of yielding in rock as a function of time for Sensitivity Case 2 with Temperature Option 1 (cont'd)

C28

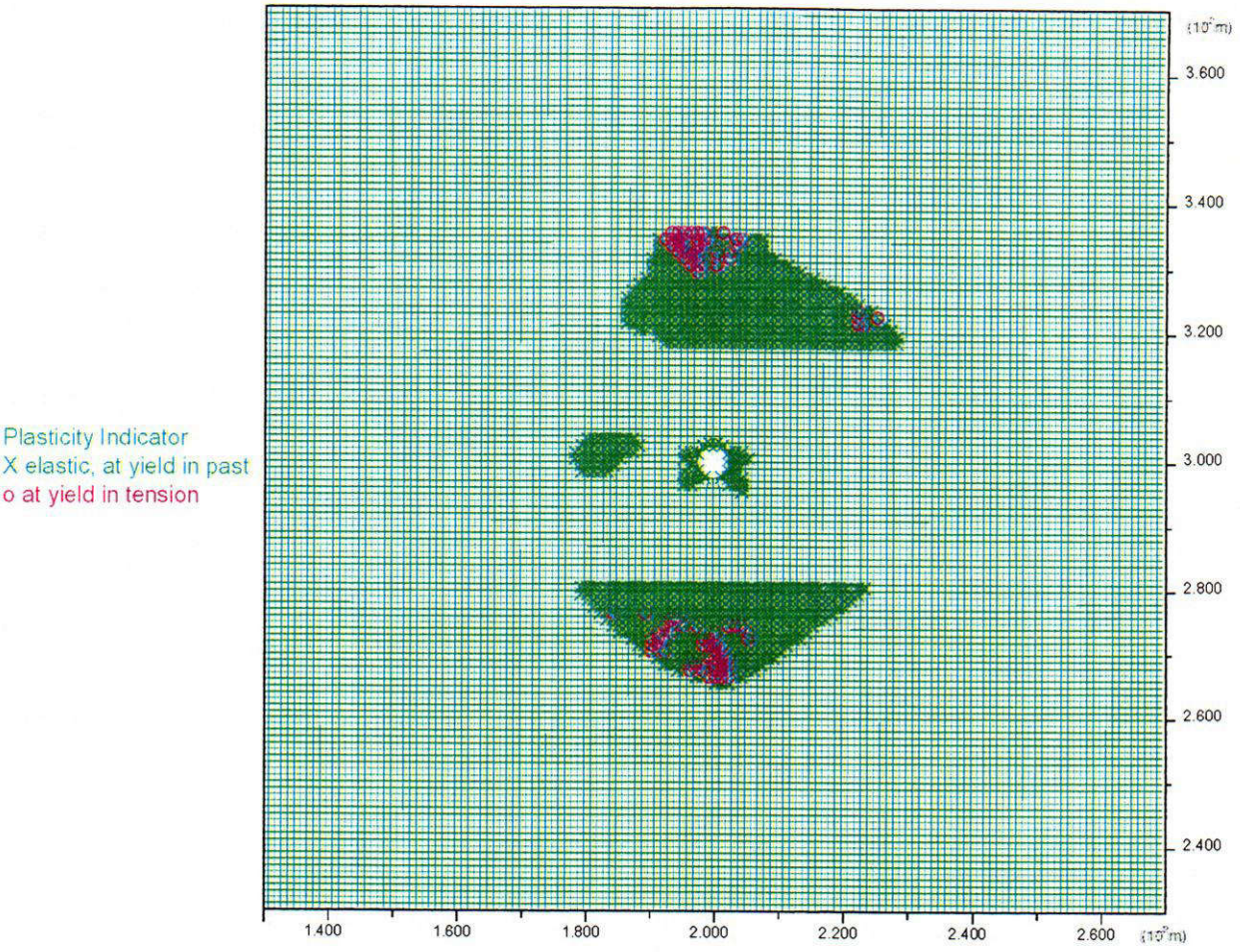

(d) After 4 Years of Heating

Figure 4-10. Extent of yielding in rock as a function of time for Sensitivity Case 2 with Temperature Option 1 (cont'd)

C29

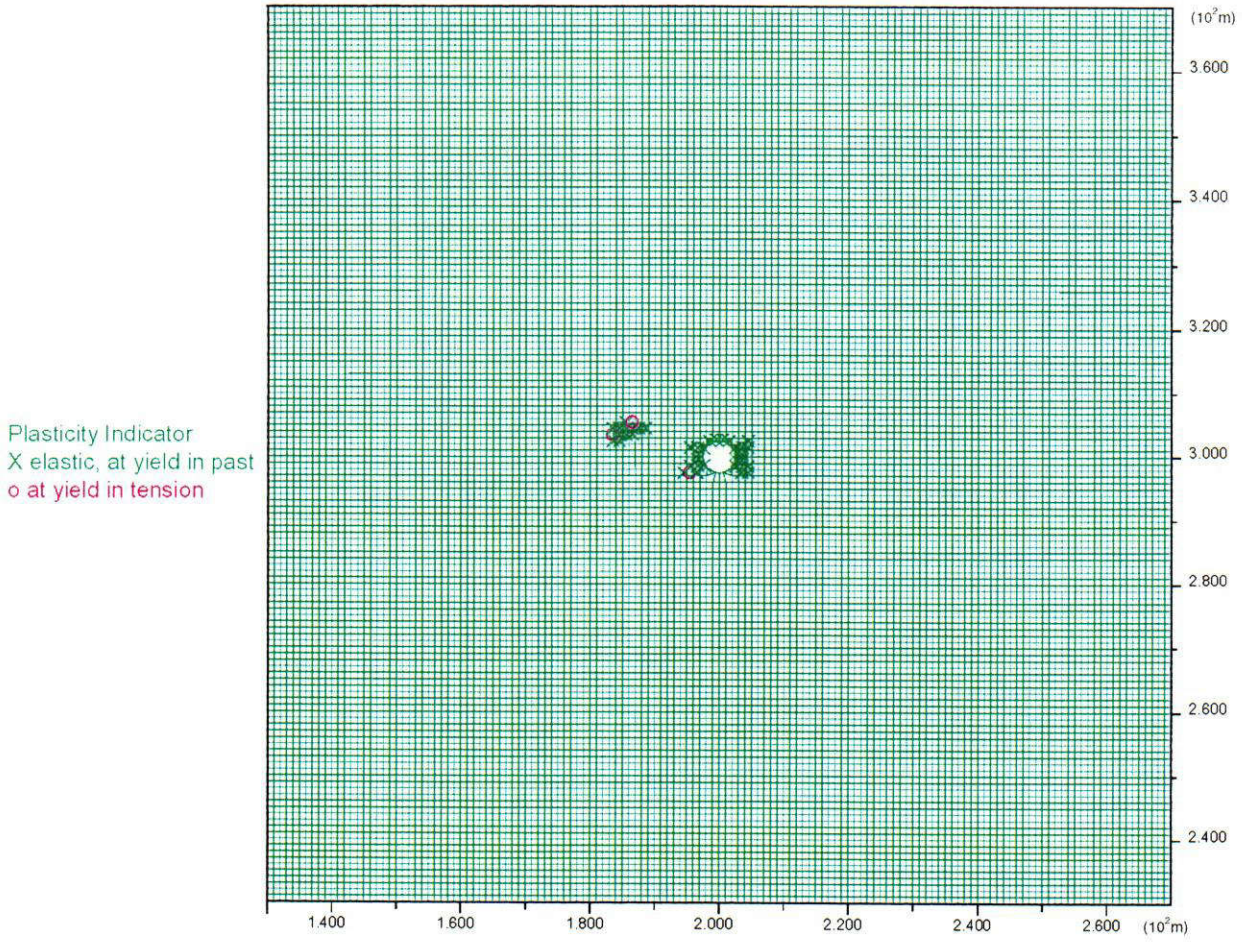

(a) After 3 Months of Heating

Figure 4-11. Extent of yielding in rock as a function of time for Sensitivity Case 2 with Temperature Option 2

C30

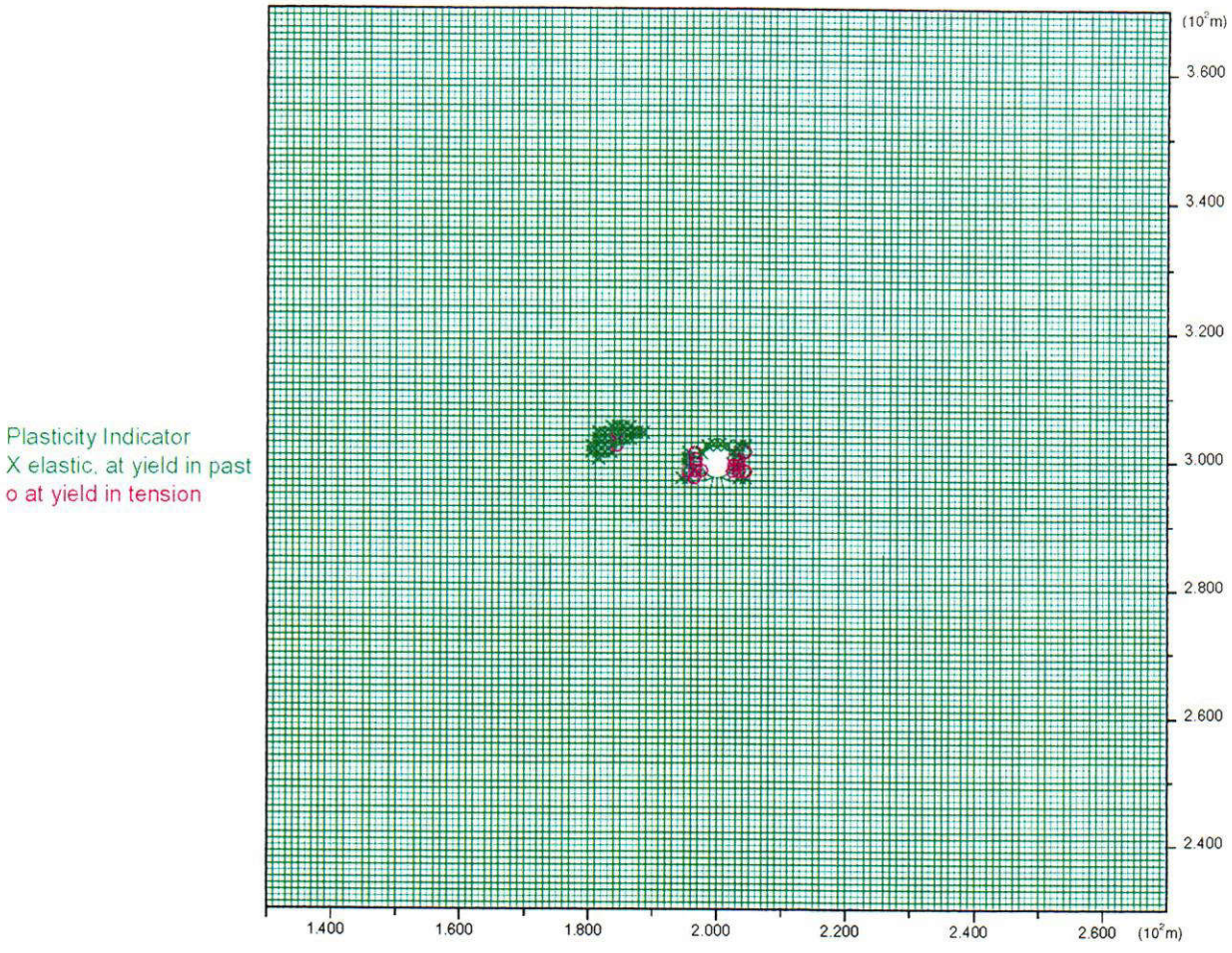

(b) After 1 Year of Heating

Figure 4-11. Extent of yielding in rock as a function of time for Sensitivity Case 2 with Temperature Option 2 (cont'd)

C31

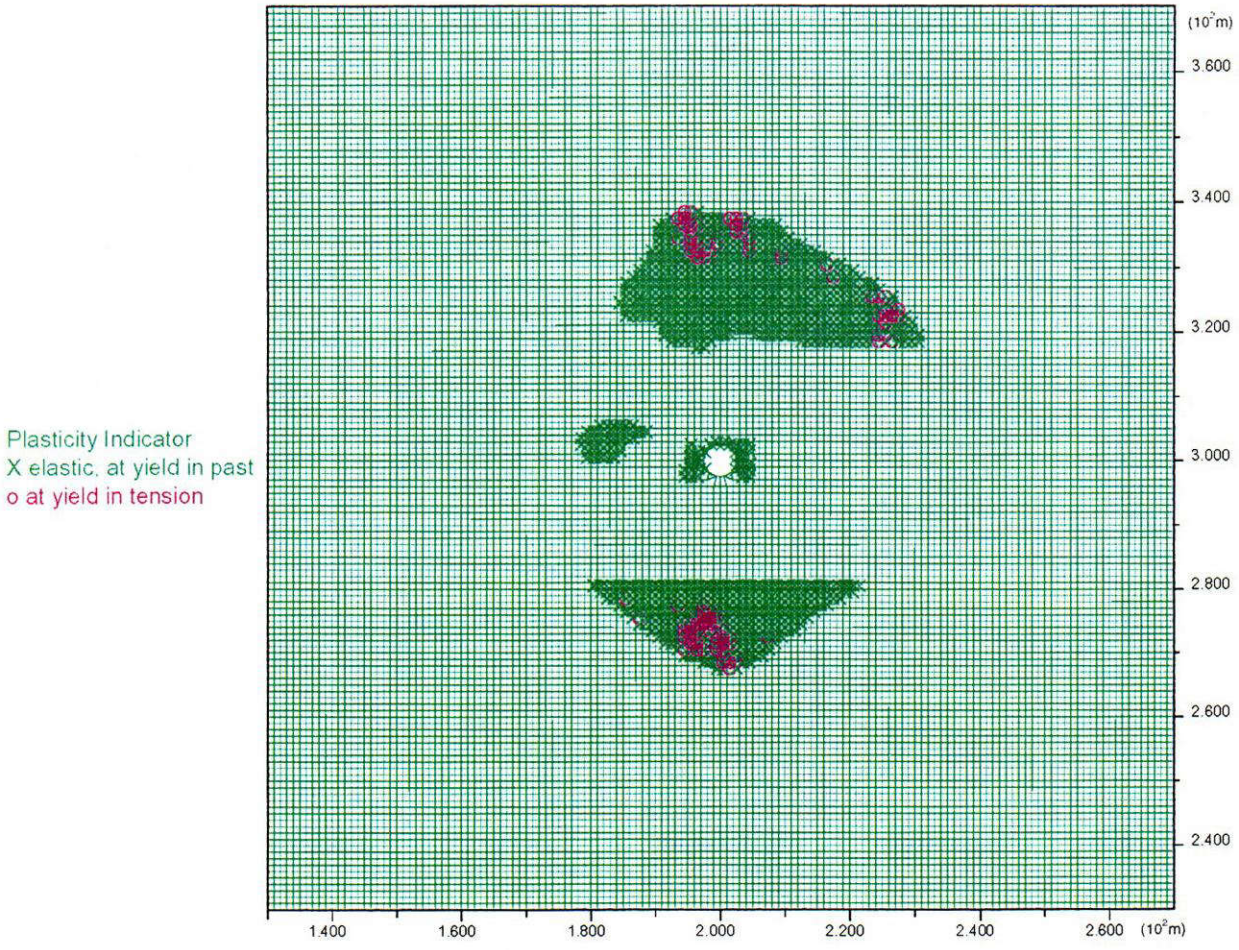

(c) After 4 Years of Heating

Figure 4-11. Extent of yielding in rock as a function of time for Sensitivity Case 2 with Temperature Option 2 (cont'd)

C32

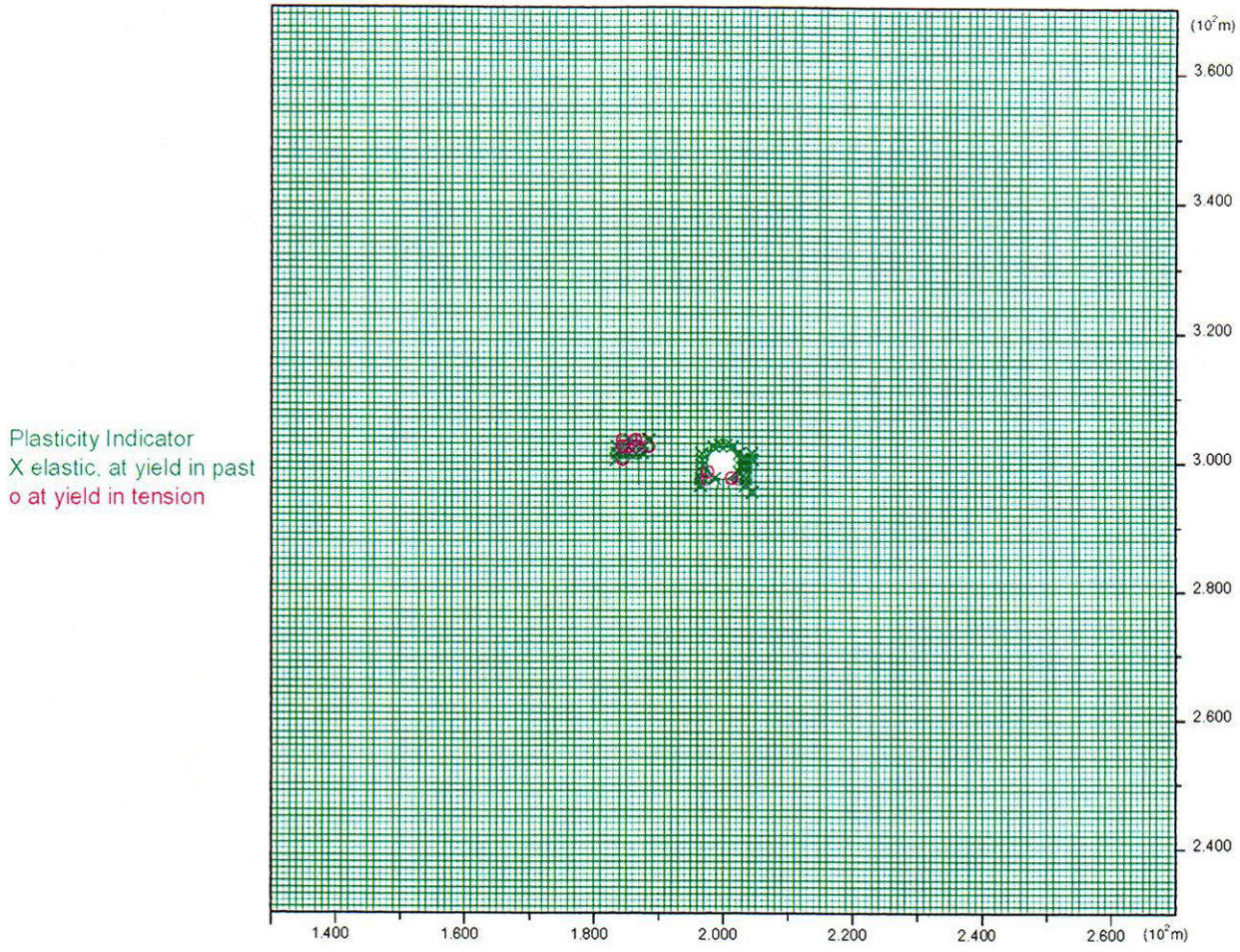

(a) After 3 Months of Heating

Figure 4-12. Extent of yielding in rock as a function of time for Sensitivity Case 3 with Temperature Option 1

C33

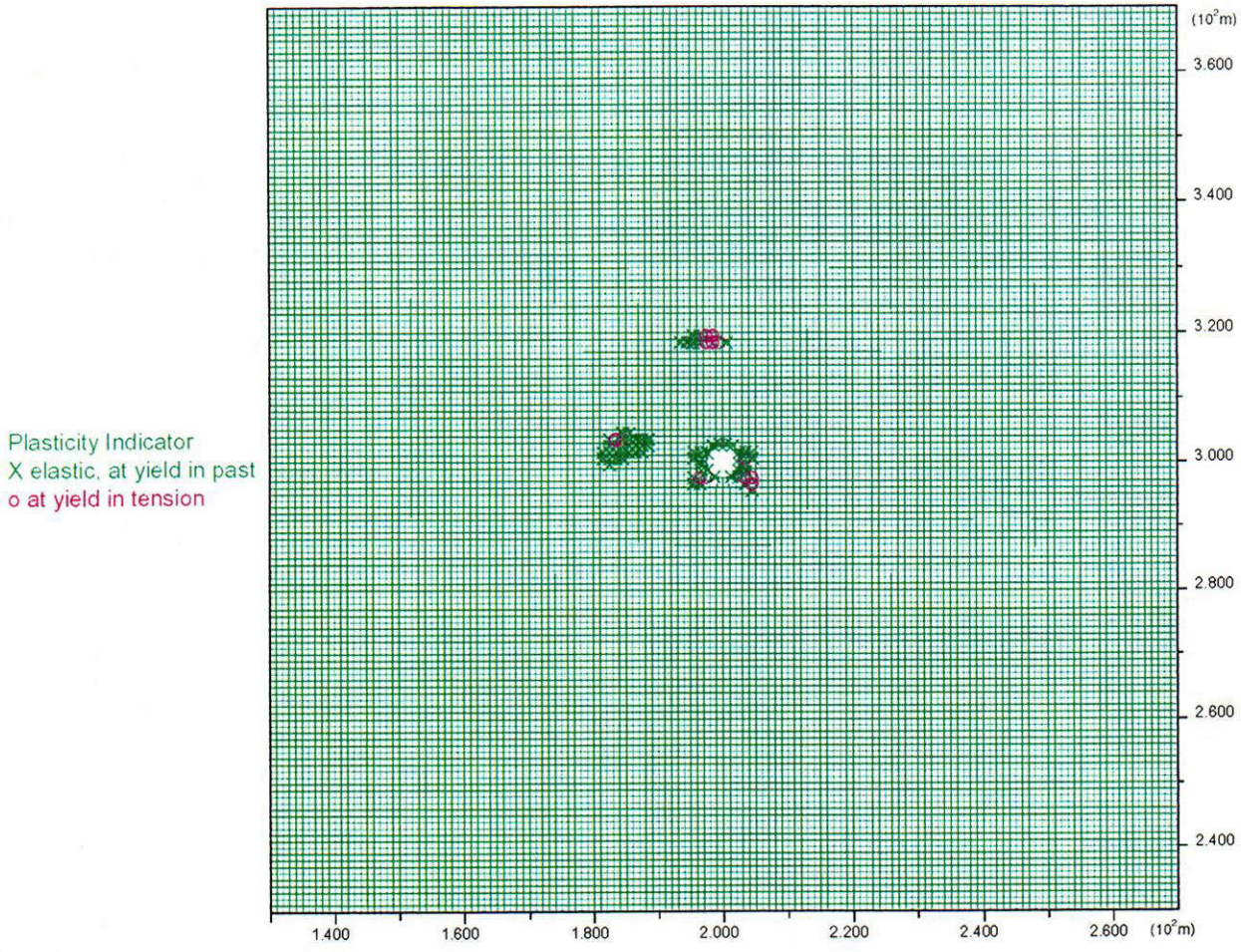

(b) After 1 Year of Heating

Figure 4-12. Extent of yielding in rock as a function of time for Sensitivity Case 3 with Temperature Option 1 (cont'd)

C34

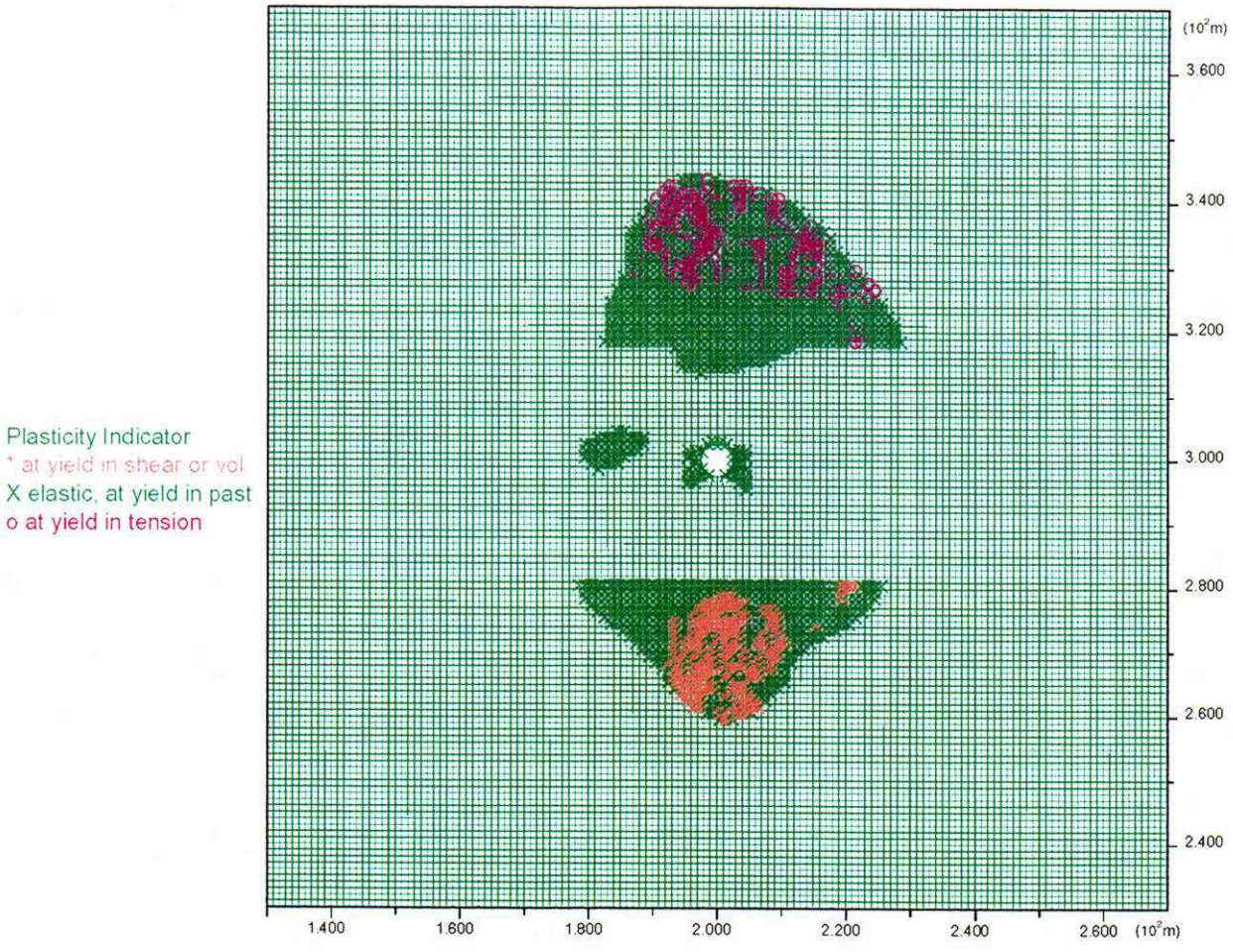

(c) After 4 Years of Heating

Figure 4-12. Extent of yielding in rock as a function of time for Sensitivity Case 3 with Temperature Option 1 (cont'd)

C35

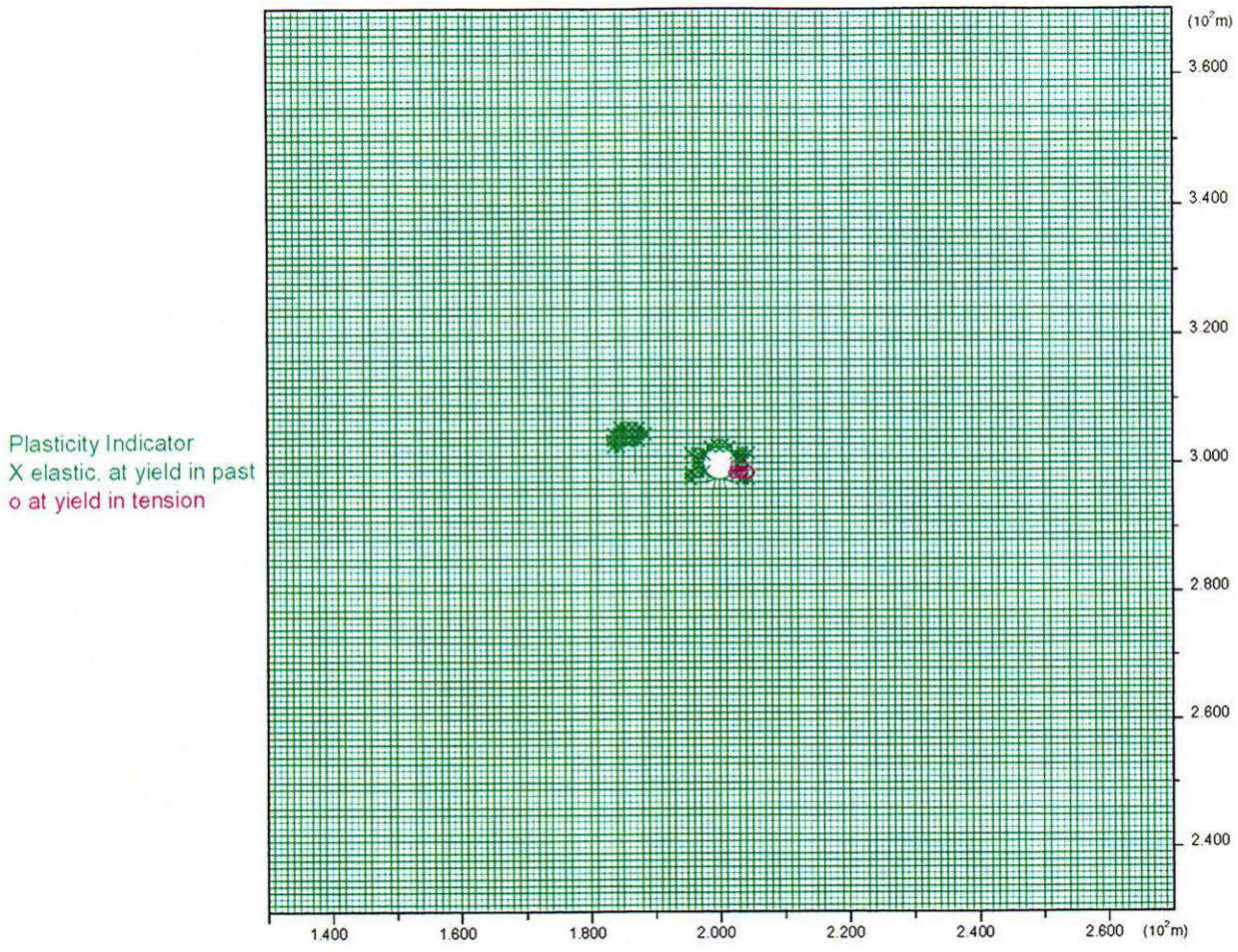

(a) After 3 Months of Heating

Figure 4-13. Extent of yielding in rock as a function of time for Sensitivity Case 3 with Temperature Option 2

C36

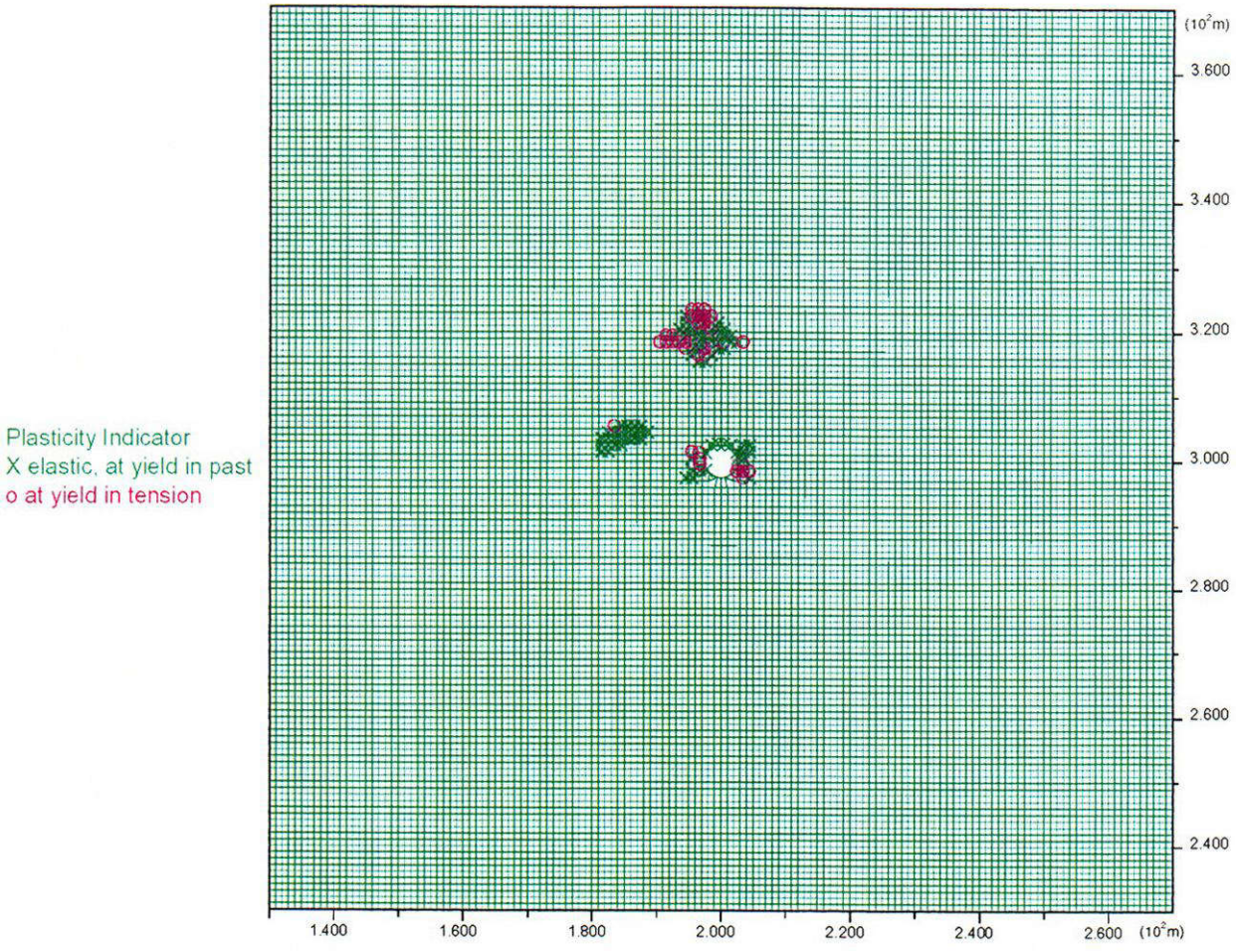

(b) After 1 Year of Heating

Figure 4-13. Extent of yielding in rock as a function of time for Sensitivity Case 3 with Temperature Option 2 (cont'd)

C37

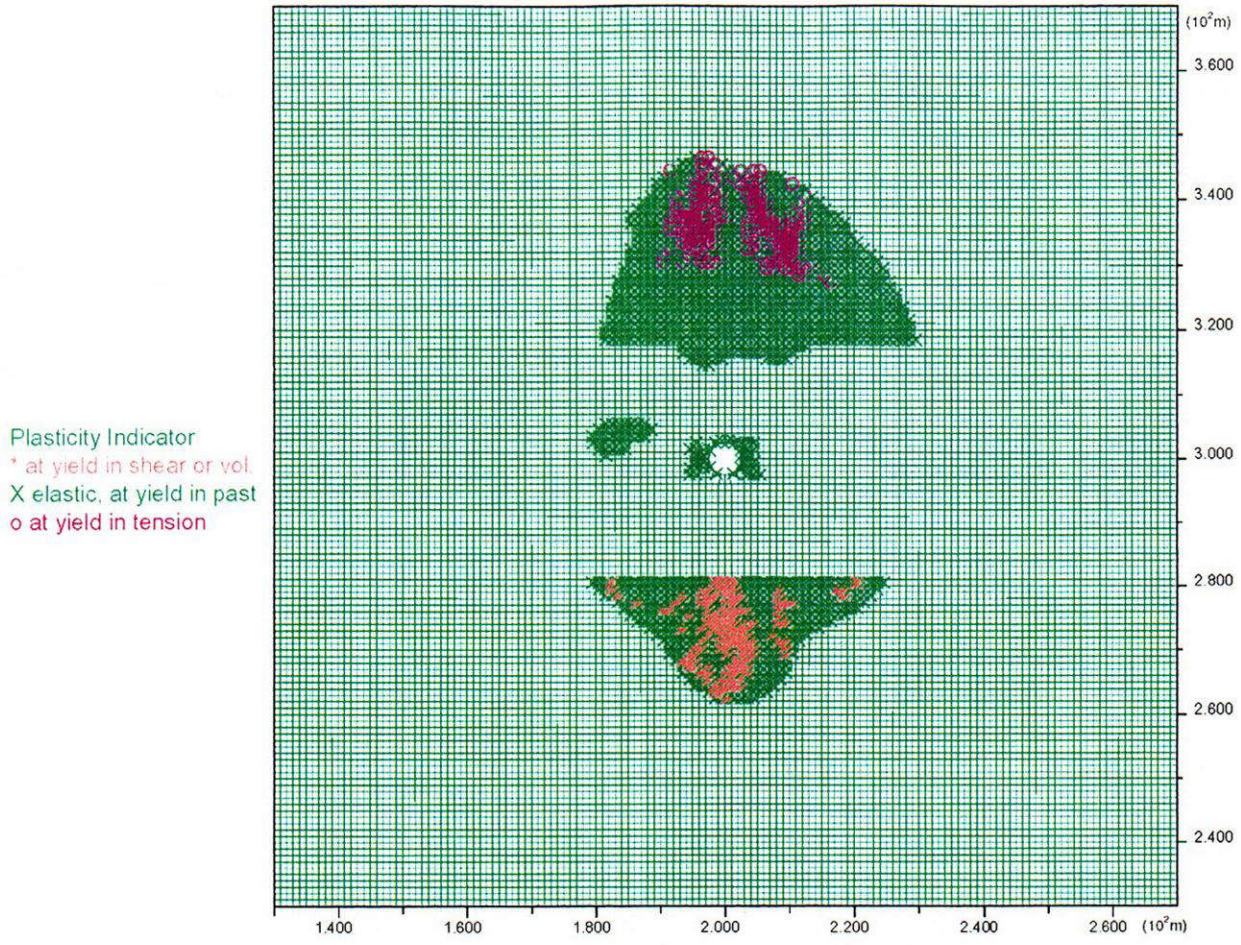

(c) After 4 Years of Heating

Figure 4-13. Extent of yielding in rock as a function of time for Sensitivity Case 3 with Temperature Option 2 (cont'd)

C38

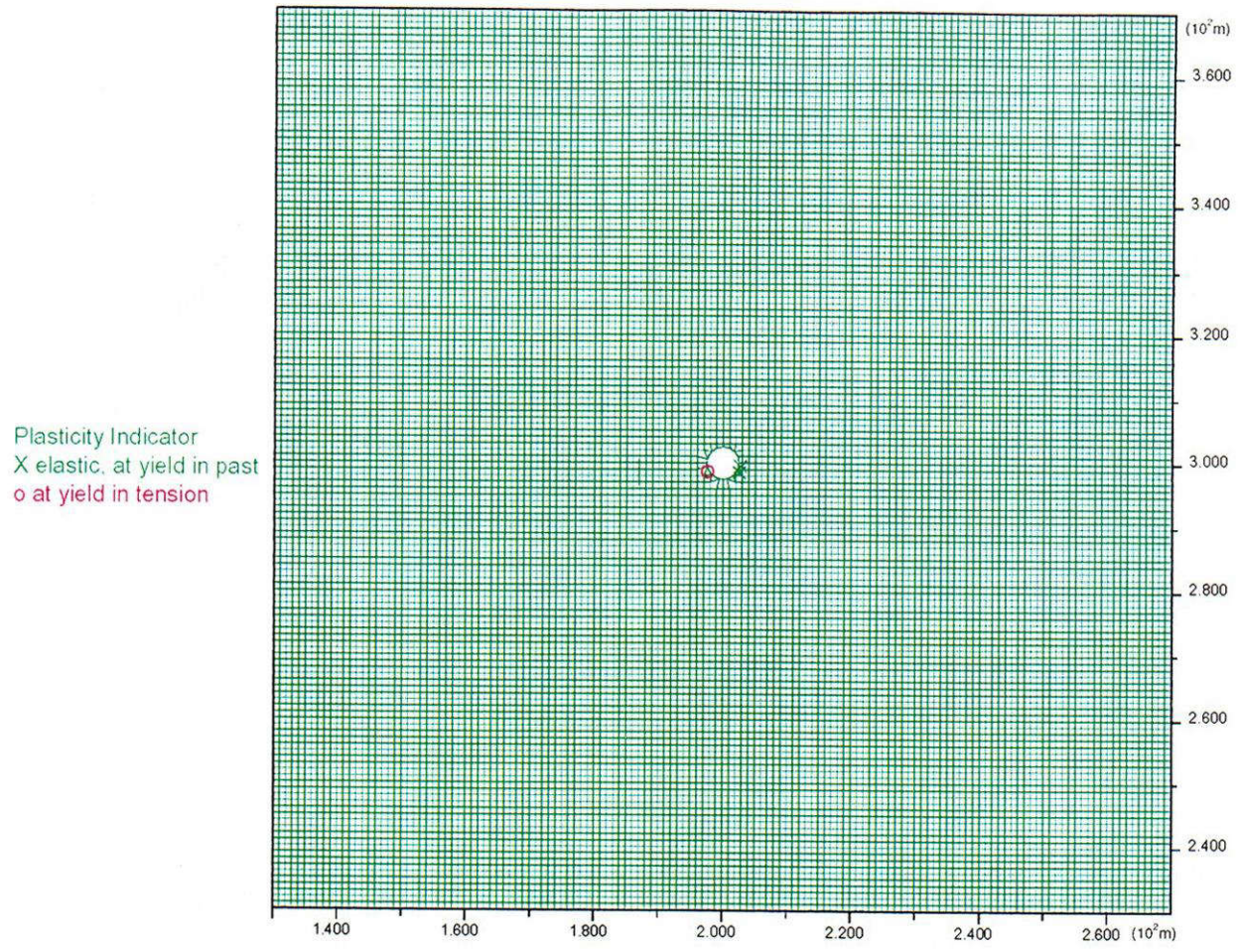

(a) After 3 Months of Heating

Figure 4-14. Extent of yielding in rock as a function of time for Sensitivity Case 4 with Temperature Option 1

C39

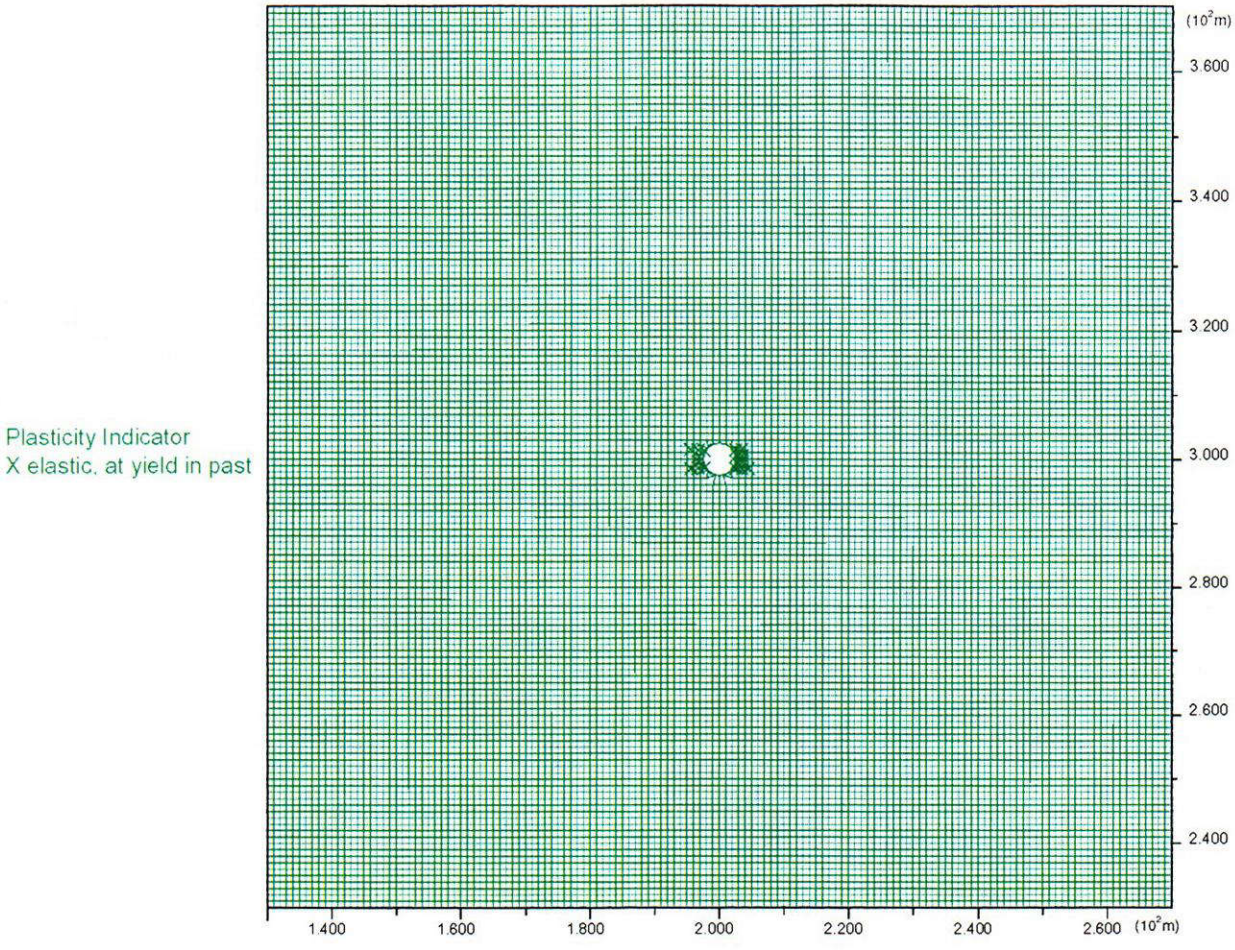

(b) After 1 Year of Heating

Figure 4-14. Extent of yielding in rock as a function of time for Sensitivity Case 4 with Temperature Option 1 (cont'd)

C40